



UNIVERSITÄT
DES
SAARLANDES

Red Blood Cell Shape Stability & Deformability In Single-Cell Capillary Flow: Effects Of Confinement, Age and Membrane Rigidity

Dissertation zur Erlangung des Grades des Doktors der Naturwissenschaften
der Naturwissenschaftlich-Technischen Fakultät der Universität des Saarlandes

Von : **Mohammed Nouaman**

Saarbrücken, 2025

Tag des Kolloquiums: 16.05.2025

Dekan: Prof. Dr.-Ing. Dirk Bähre

Berichterstatter: Prof. Dr. Christian Wagner
Prof. Dr. Chaouqi Misbah

Vorsitz: Prof. Dr. Rolf Pelster

Akad. Mitglied: Dr. Divyendu Goud Thalla

Abstract

The thesis studies red blood cell (RBC) morphology and deformability under microfluidic conditions to reveal their behavior in the microcirculation. Using novel experiments, we analyze how RBC properties, channel geometry, and flow interact. Rectangular channels with height near the RBC diameter and confinement ratios above 0.9 favor distinct croissant and slipper shapes, correlating shear rate with cell elongation. Less confined channels yield varied unstable shapes. We also examine effects of RBC age and membrane rigidity by fractionating cells and altering membranes chemically, finding a reduced formation of stable asymmetric slippers at high flow in aged or stiffened cells. Older cells more often form symmetric croissants, a pattern suppressed by membrane stiffening. Finally, we introduce a deformation index (DI) from compression-expansion tests to quantify deformability and study influences of density and rigidity. Our results enhance understanding of RBC dynamics in confined flows, aiding biomicrofluidic design and hematological diagnostics, and advancing insight into microcirculatory function and disease.

Keywords: Red blood cells, microfluidics, deformability, cell morphology, microcirculation, channel confinement, aging, membrane rigidity, biomechanics

Zusammenfassung

Diese Arbeit untersucht die Morphologie und Verformbarkeit roter Blutkörperchen (Erythrozyten) unter mikrofluidischen Bedingungen, um deren Verhalten im Mikrozirkulationssystem zu verstehen. Mit neuartigen Experimenten analysieren wir das Zusammenspiel von Zell-Eigenschaften, Kanalgeometrie und Strömungsdynamik. Rechteckige Kanäle mit einer Höhe nahe dem Zell-Durchmesser und einer Konfektionsrate über 0,9 begünstigen ausgeprägte croissant- und slipperförmige Formen, wobei eine starke Korrelation zwischen Scherrate und Zellverlängerung besteht. Geringere Konfinierung führt zu vielfältigen instabilen Formen. Außerdem werden Alter und Membransteifigkeit der Zellen durch Fraktionierung und chemische Modifikation untersucht, wobei ältere oder versteifte Zellen weniger stabile asymmetrische slipperformen. Ältere Zellen zeigen verstärkt symmetrische croissants, was durch Membranversteifung unterdrückt wird. Abschließend wird mit einem neu eingeführten Deformationsindex (DI) die Verformbarkeit durch Kompressions- und Expansionsversuche quantifiziert. Die Resultate verbessern das Verständnis der Erythrozyten-Dynamik in engen Strömungen und unterstützen die Entwicklung mikrofluidischer Geräte sowie hämatologischer Diagnostik.

Schlüsselwörter: Rote Blutkörperchen, Mikrofluidik, Verformbarkeit, Zellmorphologie, Mikrozirkulation, Kanalenge, Zellalter, Membransteifigkeit, Biomechanik

Liste of author's publications

- **M. Nouaman, A. Darras, T. John, G. Simionato, M.A.E. Rab, R. van Wijk, M.W. Laschke, L. Kaestner, C.Wagner, S.M. Recktenwald**
Effect of Cell Age and Membrane Rigidity on Red Blood Cell Shape in Capillary Flow.
Cells 2023, 12(11), 1529.
- **M. Nouaman, A. Darras, C.Wagner, S.M. Recktenwald**
Confinement effect on the microcapillary flow and shape of red blood cells.
Biomicrofluidics. 2024 Apr 1;18(2):024104.

Eidesstattliche Erklärung

Hiermit versichere ich an Eides statt, dass ich die vorliegende Arbeit selbstständig und ohne Benutzung anderer als der angegebenen Hilfsmittel, einschließlich der Nutzung von Grammarly und ChatGPT zur Verbesserung meiner schriftlichen Ausdrucksweise, angefertigt habe. Die aus anderen Quellen oder indirekt übernommenen Daten und Konzepte sind unter Angabe der Quelle gekennzeichnet. Die Arbeit wurde bisher weder im In- noch im Ausland in gleicher oder ähnlicher Form in einem Verfahren zur Erlangung eines akademischen Grades vorgelegt.

Ort, Datum

Mohammed Nouaman

Dedication

To my beloved mom (**Khadija**) and dad (**Lahcen**), for your endless love, support, and sacrifices.

To my soulmate (**Rachida**) for your unwavering faith in me, my wife's love is my greatest strength.

To my two little brothers (**Ismail & Rayan**), for inspiring me with your energy and curiosity.

To my dearest aunt (**Rachida**), for always being a source of comfort and guidance.

And to the entire Nouaman(e) family, for your boundless encouragement.

وبعد حمده

إلى أمي الحبيبة خديجة، التي كانت دومًا دعمي وملذي في كل لحظة من حياتي
وإلى أبي العزيز، الذي غرس فيّ القوة والعزيمة لأمضي قدمًا
أقول لكم إن كل نجاح أحققه هو ثمرة تعبكم وجهدكم

إلى زوجتي الغالية رشيدة، شريكة حياتي وصديقتي، التي تقف إلى جانبي دائمًا وتمنحني الحب والقوة في كل الأوقات الصعبة
أنتِ نصفِي الآخر وسندي

إلى إخوتي الصغار الأعمام، أنتم فرحتي وأملي، وبوجودكم تكتمل سعادتي.
إلى خالتي الحبيبة، التي تجمعني بها روابط الدم والقلب، لكِ مني كل الحب والاحترام.

وإلى عاتلتي الكبيرة، عائلة نعمان ونوعمان، أنتم الجذور التي تربطني بكل ما هو أصيل في حياتي.
لكل فرد منكم، أرسل خالص حيي وامتناني.

Contents

Introduction	1
Background	5
1.1 Blood Physiology	6
1.2 Red Blood Cells: Structure and Function	7
1.2.1 Definition and Essential Functions	7
1.2.2 Membrane Composition and Properties	8
1.2.3 Hemoglobin Content and Oxygen Transport	9
1.2.4 Lifespan and Senescence	10
1.3 RBC Flow in Capillaries	12
1.3.1 Deformability and Adaptation of RBCs	12
1.3.2 Bi-Stability of Single RBC Through Capillary Flow	14
1.4 Changes in RBC Flow Characteristics	17
1.4.1 Age-Related Changes	17
1.4.2 Influence of Membrane Rigidity on Capillary Transit	18
1.5 Scope and Purpose of The Study	19
Experimental Materials and Methods	23
2.1 Blood Sample Preparation	24
2.1.1 Blood Extraction	24
2.1.2 Discontinuous Density Separation Sample	25
2.1.3 Diamide Solutions and Rigidification	27
2.2 Microfluidic devices	28
2.2.1 Silicon Wafer and Epoxy Mold	28
2.2.2 PDMS-based Chip	30
2.2.3 Sacles and Geometry	31
2.3 Recording and Exporting Raw Images	32
2.3.1 Microscope, Cameras and Lenses	33
2.3.2 Image Sequences	34
2.3.3 Single Particle Tracking	34
Chapter I: Confinement Effect On The Microcapillary Single-Cell-Flow And Shape Of Red Blood Cells	37
3.1 Introduction	39
3.2 Methodology	42
3.2.1 RBC sample preparation	42
3.2.2 Microfluidic setup	42
3.3 Results	44
3.3.1 Phase diagrams of RBC shape	44
3.3.2 RBC equilibrium position across the channel width	47
3.3.3 Elongation of croissants and slippers in the microchannels	48
3.3.4 Unstable other RBC shapes	50
3.4 Conclusion	52
Chapter II: Effect of Red Blood Cell Age and Membrane Rigidity on Single Cell Capillary Flow Stability	53

4.1	Introduction	55
4.2	Experimental setup	58
4.2.1	Microfluidic Setup	58
4.2.2	RBC Sample Preparation	58
4.2.3	RBC Density Separation	59
4.2.4	Membrane Rigidification	60
4.3	Results	60
4.3.1	Stable RBC Shapes in Straight Microchannels	60
4.3.2	RBC Equilibrium Position in the Channel Cross-Section	63
4.3.3	Fraction of Stable RBC Shapes	64
4.4	Discussion	64
4.5	Conclusion	66
Chapter III: Deformability of Red Blood Cell Through a Compression-Expansion Process		69
5.1	Introduction	70
5.2	Materials and Methods	74
5.2.1	Blood Collection and Samples Preparation	74
5.2.2	Microfluidic Setup	74
5.2.3	Deformation Coefficient	76
5.2.4	Fit Model	76
5.3	Results	77
5.3.1	Deformation Illustration	77
5.3.2	Deformation Distributions	78
5.3.3	Effect of Age and Rigidity on Deformability	79
5.3.4	Deformation Rate and Deformation Time	82
5.3.5	Relaxation Effect	83
5.4	Discussion	85
5.5	Conclusion	87
General Summary and Perspectives		89
6.1	Summary of Key Findings	89
6.1.1	Influence of Geometrical Structure on RBC Morphology	89
6.1.2	Impact of Density and Membrane Rigidity on RBC Behavior	90
6.1.3	Quantitative Assessment of RBC Deformability	92
6.2	Implications and Future Directions	93
6.2.1	Microfluidic Device Design	93
6.2.2	Blood Flow Modeling	93
6.2.3	Hematological Diagnostics	94
6.2.4	Therapeutic Strategies	94
6.2.5	Future Research Directions	94
References		99

Liste of Figures

1.1	Schematic Representation of Blood Component Stratification Following Centrifugation: A Visual Guide to the Separation and Identification of Distinct Blood Fractions	7
1.2	Morphological Analysis of Resting Red Blood Cell Discocyte Shape: Comparative Visualization of Single Cell Topography Using Advanced Decoupling Techniques for Structural Characterization	8
1.3	Multiscale Structural Analysis of Red Blood Cell Morphology: Integrated Visualization of Discocyte Shape, Membrane Composition, and Spectrin Network Architecture in Resting State . . .	9
1.4	Comprehensive Structural Visualization of Hemoglobin in Red Blood Cells: From Macroscopic Vessel Context to Molecular Architecture of Alpha and Beta Chains, Quaternary Structure, and Heme Prosthetic Group	10
1.5	Dynamic Visualization of Red Blood Cell Deformation During Microchannel Transit: Comparative Analysis of Shape Transitions from Initial Biconcave Disc to Elongated Forms Based on Varying Entry Orientations	13
1.6	Visualization of Red Blood Cell Dynamics Under Varying Shear Stress: Transitional Stages from Tumbling to Rolling and Tank-Treading Motions in Moderate Flow Conditions	15
1.7	Multifaceted Analysis of Red Blood Cell Shape Dynamics in Microfluidic Channels: Phase Diagram of Croissant and Slipper Morphologies Correlated with Velocity and Pressure, Complemented by Lateral Distribution Probability Density Functions	16
1.8	Morphological and Biomechanical Alterations in Red Blood Cells Exposed to Oxidative Stress: Dose-Dependent Effects of Diamide on Cell Shape and Membrane Shear Modulus	19
2.1	Systematic Protocol for Red Blood Cell Isolation: Multi-Step Centrifugation and Washing Process for Obtaining Purified Erythrocyte Samples from Whole Blood for Experimental Applications	25
2.2	Detailed Protocol for Red Blood Cell Separation Using Percoll Density Gradient: Step-by-Step Visualization of Discontinuous Layer Preparation and Strategic Assembly for Optimal Fractionation	26
2.3	Visualizing Red Blood Cell Stiffness Changes with Increasing Diamide Exposure: From Preparation to Analysis of Treated Samples	28
2.4	Microfluidic Device Fabrication: A Comprehensive Process Integrating Photolithography and Soft Lithography Techniques	29
2.5	Step-by-Step Fabrication of Epoxy Molds Using PDMS Channels: A Practical Approach to Creating High-Fidelity Microfluidic Structures	30
2.6	Microscopic Analysis of Microfluidic Channel Geometries: Cross-Sectional and Top-View Observations for Compression-Expansion Studies	32
2.7	Comprehensive Microfluidic Experimental Setup: Integration of Pressure Control, Microscopy, and Data Acquisition Systems	33
2.8	Visualization and Image Processing of Red Blood Cell Flow in Microfluidic Channels: From Reservoir Entry to Single-Cell Analysis	35
3.1	Microscale Hydrodynamics of Red Blood Cell Deformation in Confined Microfluidic Channels: Visualization and Analysis of Croissant-like, Slipper-shaped, and Variant Morphologies with Respect to Cell Positioning, Flow Direction, and Pressure-Dependent Velocity Dynamics	40
3.2	Comprehensive Microfluidic Channel Design Schematic: Comparing 10 and 15 Micrometer Width Channels with Variable Heights, Emphasizing Observation Points and Resting Red Blood Cell Scale for In-Depth Flow Dynamics and Cellular Behavior Analysis	43
3.3	Quantitative Analysis of Red Blood Cell Elongation in Microfluidic Channels: From Raw Image Capture to Elongation Index Calculation Using Matlab's BoundaryBox Tool and Custom Image Processing Techniques	44

3.4	Comprehensive Morphological Analysis of Red Blood Cell Deformation in Microfluidic Channels: Velocity-Dependent Shape Phase Diagrams Illustrating Transitions Between Croissant-like, Slipper-like, and Other Configurations Across Varying Capillary Numbers	46
3.5	Comprehensive Analysis of Red Blood Cell Distribution in Microfluidic Channels: Probability Density Functions of Normalized Cell Positions Across 10 and 15 Micrometer Wide Channels Under Varying Pressure Conditions	47
3.6	Morphological Analysis of Red Blood Cell Shape Transitions in Varied Microfluidic Channels: Quantitative Assessment of Croissant and Slipper Conformations Across Shear Rate Gradients with Elongation Index Correlations	49
3.7	Comprehensive Analysis of Red Blood Cell Shape Dynamics in Confined Microfluidic Channels: Temporal Evolution, Lateral Movement, and Stability Assessment of Croissant, Slipper, and Other Morphologies	51
4.1	Comparative Analysis of Red Blood Cell Shape Bistability: Croissant and Slipper Morphologies Observed In Vivo, In Vitro, and In Silico	55
4.2	Machine Learning-Assisted Classification of Red Blood Cell Morphologies in Microfluidic Flow: Comparing Convolutional Neural Network (CNN) Output with Manual Identification for Slipper and Croissant Shapes	57
4.3	Density-Based Fractionation of Red Blood Cells: Visualization of Discontinuous Percoll Gradient Separation Before and After Centrifugation	59
4.4	Comprehensive Phase Diagrams of Red Blood Cell Shapes: Effects of Density Fractionation and Membrane Rigidification on Morphology in Confined Microfluidic Flow	61
4.5	Comprehensive Analysis of Red Blood Cell Morphology and Deformability: Effects of Cell Age and Membrane Rigidification in Microfluidic Flow	62
4.6	Velocity-Dependent Deformability Index Distributions of Density-Fractionated Red Blood Cells: A Comparative Analysis Across Multiple Layers	62
4.7	Lateral Distribution Patterns of Red Blood Cells in Microfluidic Channels: Impact of Cell Density and Membrane Rigidification Across Multiple Flow Velocities	63
4.8	Dynamic Behavior of Red Blood Cells in Capillary Flow: Quantifying Shape Instabilities Across Density Fractions and Membrane Rigidification Levels	64
5.1	Comparative Analysis of Red Blood Cell Deformation in Microchannels: Smooth versus Sudden Contractions and Their Impact on Cell Elongation Dynamics	72
5.2	Microfluidic Design for Red Blood Cell Compression-Expansion Studies: A Dual-Width Channel Approach with Precise Dimensional Control	75
5.3	Dynamic Shape Evolution of a Single Red Blood Cell During Microfluidic Compression-Expansion: A Quantitative Analysis of Deformation Index	77
5.4	Pressure-Dependent Deformation Dynamics of Red Blood Cells in Microfluidic Compression-Expansion: A Statistical Analysis of Deformation Index Distributions	78
5.5	Quantitative Analysis of Red Blood Cell Deformation in Microchannels: Effects of Cell Age and Membrane Rigidity on Compression-Expansion Dynamics	79
5.6	Comprehensive Analysis of Red Blood Cell Deformation Across Pressure Ranges: Comparing Whole Blood, Density-Separated Fractions, and Membrane-Rigidified Samples in Microfluidic Channels	80
5.7	Quantitative Analysis of Red Blood Cell Deformation Kinetics: Comparing Deformation Speed and Relaxation Time Across Cell Age and Membrane Rigidity in Microfluidic Expansion	82
5.8	Quantitative Analysis of Red Blood Cell Shape Recovery Dynamics: Exponential Modeling of Post-Expansion Relaxation in Microfluidic Channels	84
5.9	Comparative Analysis of Red Blood Cell Relaxation Dynamics: Effects of Cell Age and Membrane Rigidity on Post-Deformation Recovery in Low-Pressure Microfluidic Flow	85

Tables

1.1	Comparative Analysis of Oxygen and Carbon Monoxide Binding Kinetics in Isolated Alpha and Beta Hemoglobin Chains: Quantification of Association and Dissociation Constants Under Physiological Conditions	11
2.2	Detailed Composition of Percoll Density Gradient Layers for Red Blood Cell Separation: Elements, Densities, and Volumes for Precise Buffer Solution Preparation	27
3.3	Comparative Analysis of Channel Geometries: An Overview of Diverse Silicon-Based Wafer-Fabricated Microfluidic Channels with Standardized Total Length of 40 mm	42
5.4	Quantitative Analysis of Red Blood Cell Surface Area-to-Volume Relationships: Insights into Cellular Geometry and Measurement Techniques	71

Blood is recognized as an organ consisting of such a complex and dynamic fluid composition; it contains plasma, dissolved substances, and different cellular entities. The amount of blood approximates 7% of human body weight and hence has been considered the second largest organ after the skin. Maintenance for health, better known as blood circulation, goes through the complex vascular network from the early stages of fetal development through the whole course of life. It is this circulation that ensures no tissue is deprived of oxygen and nutritional substances, and it aids in the excretion of metabolic waste products. In addition, because of the dynamic nature of blood, it responds to physiological changes in demand—such as would be encountered during exercise or after injury—by regional flow and distribution changes. Because red blood cells are the most abundant cellular elements present in blood, they have the most pronounced effect on the flow characteristics of blood. These cells assume a biconcave shape, and their anatomy is highly specialized, coupled with hemoglobin, for oxygen transport. Second, imbalances in the circulation of blood lead to a myriad of physiological problems, including vascular blockages manifested by an inability of the heart muscle to contract and ischemic events. This is usually due to clot formation or pathological vessel wall changes, which in turn are coupled to dynamics in blood flow. An in-depth understanding of the function and role that erythrocytes play in flow is relevant to their application in unraveling the underlying mechanisms of circulatory and hematological disorders that may be pertinent to the improvement of diagnostic techniques and treatment strategies, with effects bound to impact positively on patient outcome. Blood is considered an exemplary model fluid for the area of biological fluid dynamics owing to its unique physical properties and relative simplicity compared to the other biological fluids. Extensive research in blood dynamics and hemorheology, in particular, has been carried out with its non-Newtonian behavior in mind, where viscosity decreases with increased shear rate due to the dissociation of RBC aggregates under high shear stresses. These have pointed out that a complex interaction takes place between the dynamics of blood flow and its cellular constituency. For example, the viscosity reduction property allows

blood to flow more smoothly through tiny capillaries and avoids blockages. Second, research into blood rheology provides important information on RBC mechanical properties and their interaction with other blood components, which is highly desirable for a better understanding of various pathological conditions. Recent developments in microscopy and the methodologies of analyses have completely changed blood research from simple macroscopic observation into the investigation of single cells. Novel techniques including high-resolution imaging, flow cytometry, and microfluidics enable researchers now to investigate at unprecedented resolution the behavior of individual RBCs. While in-vitro blood analysis is considered one of the cornerstones of diagnostics in general, it most often deals with static or highly simplified geometries, and preprocessing procedures that might in turn affect the properties of RBCs. Advanced methodologies for analysis have given way to more precise explorations of blood behavior and function at an unprecedented level of accuracy and detail. Moreover, it has allowed for the detection of small changes in RBC shape and mechanics that reflect a wide range of diseases and opened new avenues toward early diagnosis and specific therapy. RBC deformability is considered a basic element for sustaining blood flow, in particular in concentrated suspensions. The deformability of RBCs implies the ability to change shape under the action of external forces and is an important factor in passing through narrow capillaries while maintaining blood flow at an optimum. Indeed, deformability plays another key role in shaping collective phenomena such as the lateral migration and axial distribution of RBCs within channels, setting the broader landscape within which blood rheology and microcirculatory dynamics take place. Changes in RBC deformability are intimately associated with their aging and ultimate removal from circulation, forming parts of the pathophysiology of various diseases such as anemia and hemolytic disorders. Knowledge of modulating factors on RBC deformability will be of importance concerning membrane composition and the integrity of the cytoskeletal network, in developing therapeutic interventions to restore normal blood flow in pathological conditions. These microfluidic channel experiments form a good basis for studies of RBCs under controlled conditions, particularly in straight microchannels with highly diluted suspensions. In this way, these experiments model conditions of microvascular networks and thus enable the detailed investigation of mechanics and interactions between RBCs to be performed under conditions relevant for physiology. Such a microscopic snapshot, together with careful examination of RBC shape and axial position, may be used by the researchers in constructing shape-phase diagrams that could give more detailed insights into the mechanical properties and behavior of RBCs under various conditions. These figures delineate the flow conditions dependence of RBC shape transitions and provide a frame of reference in which to understand how RBCs navigate complex vascular environments. These will form the basis on which the further study of RBC deformability and its implications on dynamic features of blood flow and microvascular functions are founded.

In subsequent chapters, this thesis develops an organized and systematic approach, using these insights progressively to investigate specifically the scientific bases that would be necessary for presenting the components of blood, their mechanical and biological properties, and their flow characteristics in low Reynolds number systems. It will consist of two parts: The first part will describe in detail the basic principles of blood flow regulation, with an emphasis on the role of RBCs in maintaining hemodynamic stability. The second part will explain metrological procedures and fabrication protocols that focus on the main experimental setups and specific modifications made in each case. Then, the results parts are coming after: the first investigation, which will be referred to as Chapter I , will elaborate on the laboratory experiments of RBCs in flow through straight microfluidic channels by focusing on two critical areas: the RBC shape-phase diagram and the influence of confinement on RBC shape stability. The review, in the second result labeled Chapter II , examines how cell age and membrane stiffness influence RBC shape stability. Not last but not least, the third result, which was labeled as Chapter III , will be dedicated to a double-width channel in applying compression and expansion forces to RBCs for investigations into their deformability while manipulating age and membrane rigidity. These chapters will attempt to give an in-depth analysis of the behavior and mechanical properties of RBCs, which can be valuable insight into the complex dynamics of blood flow and cellular interactions within microfluidic systems. Such knowledge will help us understand them in both normal physiology and disease pathology.

Contents:

1.1	Blood Physiology	6
1.2	Red Blood Cells: Structure and Function	7
1.2.1	Definition and Essential Functions	7
1.2.2	Membrane Composition and Properties	8
1.2.3	Hemoglobin Content and Oxygen Transport	9
1.2.4	Lifespan and Senescence	10
1.3	RBC Flow in Capillaries	12
1.3.1	Deformability and Adaptation of RBCs	12
1.3.2	Bi-Stability of Single RBC Through Capillary Flow	14
1.4	Changes in RBC Flow Characteristics	17
1.4.1	Age-Related Changes	17
1.4.2	Influence of Membrane Rigidity on Capillary Transit	18
1.5	Scope and Purpose of The Study	19

1.1 Blood Physiology

Blood is an essential fluid, accounting for approximately 7-8% of human body weight, and it has a vital roles to maintain health and balance within the body. It is made up of four main components: plasma, red blood cells (RBCs), white blood cells (WBCs), and platelets (check Figure 1.1), each playing a vital role in the body's circulatory and immune systems.

The liquid portion of blood, known as plasma, constitutes about 55% of its total volume. Plasma is mostly water (90%), but it also contains important dissolved substances such as proteins, electrolytes, nutrients, hormones, and waste products^[1]. Plasma proteins, including albumin, globulins, and fibrinogen, serve critical functions: maintaining hydrostatic pressure, supporting immune responses, and aiding in blood clotting^[2]. Plasma also acts as a transport medium, carrying essential molecules like glucose, lipids, respiratory gases, and metabolic waste, helping maintain homeostasis and enabling communication between cells throughout the body. The oxygen-carrying function of blood is managed primarily by RBCs, which make up about 45% of blood volume, a measurement known as the hematocrit^[1]. These cells have a unique biconcave shape (see Figure 1.2.A and Figure 1.3.A) that maximizes their surface area for efficient gas exchange. RBCs are responsible for transporting oxygen from the lungs to tissues and returning carbon dioxide to the lungs for exhalation. This is made possible by hemoglobin, a protein found in abundance within RBCs, with each cell containing approximately 270 million hemoglobin molecules. Their lifespan is about 120 days, after which they are broken down and removed by the spleen and liver^[3,4]. The immune defense of the body is primarily supported by WBCs, which, although making up just 1% of blood volume, are indispensable for protecting against infections and foreign invaders^[1]. WBCs come in various types, each with specialized functions. Neutrophils are the most abundant and act as the body's first line of defense against infections. Lymphocytes, which include B cells and T cells, play a crucial role in adaptive immunity by producing antibodies and targeting infected cells. Monocytes, which differentiate into macrophages, are involved in engulfing pathogens and presenting antigens to other immune cells. Eosinophils and basophils, though less common, participate in responses to parasitic infections and allergic reactions. Platelets, the smallest cellular components in blood, play an essential role in the process of clotting, or hemostasis^[1]. Originating from large cells in the bone marrow known as megakaryocytes, platelets respond to injury by adhering to damaged blood vessels. Once activated, they release granules that attract more platelets to the site, forming a temporary plug. This process triggers the coagulation cascade, which leads to the conversion of fibrinogen to fibrin, stabilizing the clot and ensuring proper sealing of the wound^[5]. This mechanism is vital in preventing excessive blood loss and ensuring that clots form only where necessary^[6].

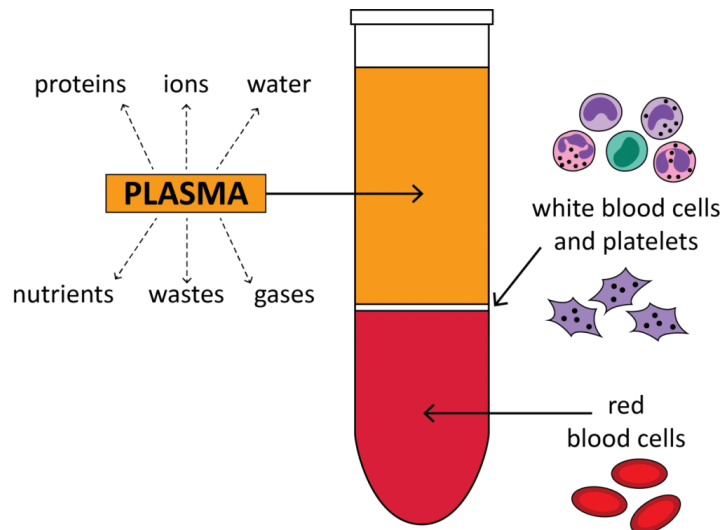


Figure 1.1: Illustration depicting the outcome of blood centrifugation, which facilitates the separation of distinct components within the blood composition. *Reprinted with permission from Glanlab*^[7].

1.2 Red Blood Cells: Structure and Function

1.2.1 Definition and Essential Functions

The specialized blood cells, RBCs (also known as erythrocytes, red cells, or rarely as blood corpuscles), serve the primary function of transporting oxygen from the lungs to tissues and facilitating the return of carbon dioxide from tissues to the lungs. They are characterized by their biconcave disc shape (see Figure 1.2.A and Figure 1.3.A), which increases their surface area-to-volume ratio, making them ideal for gas exchange. Unlike most other cells, mature RBCs lack a nucleus and other organelles, allowing more space for hemoglobin, the protein responsible for binding and transporting oxygen. The unique biconcave shape of RBCs not only increases surface area but also enhances their flexibility. This deformability is essential for RBCs to pass through microvessels and efficiently deliver oxygen to all body tissues^[1]. The production of RBCs, known as erythropoiesis, occurs in the bone marrow and is regulated by the hormone erythropoietin (EPO). EPO production is primarily stimulated by hypoxia, or low blood oxygen levels, ensuring that the body can respond to changing oxygen needs by adjusting RBC production accordingly^[3]. Once released into the bloodstream, RBCs function for approximately 120 days before being engulfed by phagocytes in the spleen, liver, and bone marrow. This life cycle ensures that old and potentially damaged RBCs are continuously removed and replaced with new ones, maintaining efficient oxygen transport. Disorders in RBC function can lead to various health problems. For instance, anemia, characterized by a deficiency in RBC number or function, results in impaired oxygen delivery to tissues, causing symptoms such as fatigue and weakness. Conditions like sickle cell disease, which involve structural abnormalities in RBCs, can lead to complications such as vascular occlusion and hemolysis^[8].

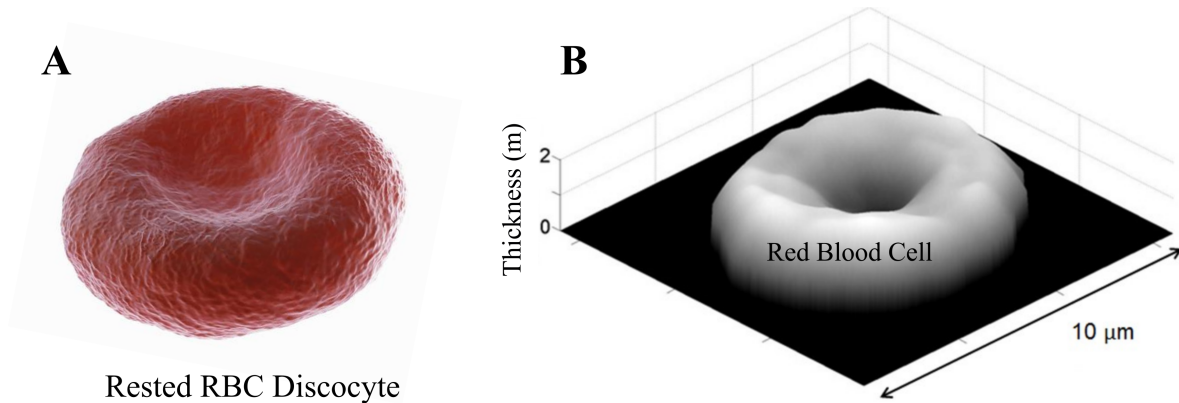


Figure 1.2: (A)- Single RBC at rest taking the discocyte shape. (B)- Visualization depicting the topography of discocyte-shaped single RBC obtained through the application of the decoupling procedure. The decoupling procedure enables the separation and mapping of distinct elements within the RBC composition, providing valuable insights into their morphological characteristics and structural properties. *Source: Memmolo et.al^[9] used with permission.*

1.2.2 Membrane Composition and Properties

The membrane of RBC is a sophisticated structure crucial for the cell's function and durability. It consists of a lipid bilayer scattered with various proteins (presented in Figure 1.3), providing the necessary balance between flexibility and mechanical strength essential for RBCs to navigate the circulatory system and perform their primary role in gas transport.

The discussion surrounding the relative importance of membrane composition versus cytoskeletal integrity in determining RBC deformability has been a focal point in hematological research. Some studies suggest that alterations in membrane lipid composition, such as changes in cholesterol content, can significantly impact the fluidity and mechanical properties of the RBC membrane, thereby affecting its ability to deform under shear stress^[10–12]. Conversely, other research emphasizes the role of the cytoskeleton, particularly the spectrin-actin network, in providing structural support and resilience against deformation^[4,13–15]. For instance, mutations in spectrin or associated proteins can lead to conditions such as hereditary elliptocytosis, where the RBCs exhibit increased rigidity and reduced deformability^[16–18]. Furthermore, it is essential to consider that variations in membrane properties are not uniform across species. For example, studies have shown that the RBC membranes of some mammals exhibit different lipid compositions compared to humans, which can influence their mechanical properties and functionality under varying physiological conditions^[19,20]. This interspecies variability underscores the need for a nuanced understanding of how both membrane composition and cytoskeletal integrity contribute to RBC functionality.

The lipid bilayer forms the basic structure of the RBC membrane (Figure 1.3.B), composed primarily of phospholipids and cholesterol. Phospholipids arrange in a bilayer with hydrophobic tails facing inward and hydrophilic heads facing outward, creating a semipermeable membrane.

Cholesterol molecules dispersed within this bilayer modulate membrane fluidity, making it neither too rigid nor too fluid, which is vital for RBC deformability as it passes through narrow capillaries^[21]. The membrane contains integral and peripheral proteins that give to its structural integrity and function. Integral proteins (see Figure 1.3.C), such as Band 3 and glycophorin, play crucial roles in ion transport and cell recognition. Band 3 facilitates chloride-bicarbonate exchange, aiding in ionic balance maintenance and gas transport efficiency^[22]. Peripheral proteins like spectrin, actin, and ankyrin form a structural network on the inner surface of the membrane, providing the mechanical stability and flexibility necessary to withstand stress during circulation, enabling the cell to return to its original shape after deformation^[23]. Changes in the composition or structure of the RBC membrane can lead to various types of hemolytic anemia, where cells are destroyed prematurely. Conditions such as hereditary spherocytosis and hereditary elliptocytosis arise from mutations in genes encoding membrane or cytoskeletal proteins, resulting in fragile cells prone to rupture under mechanical stress^[24].

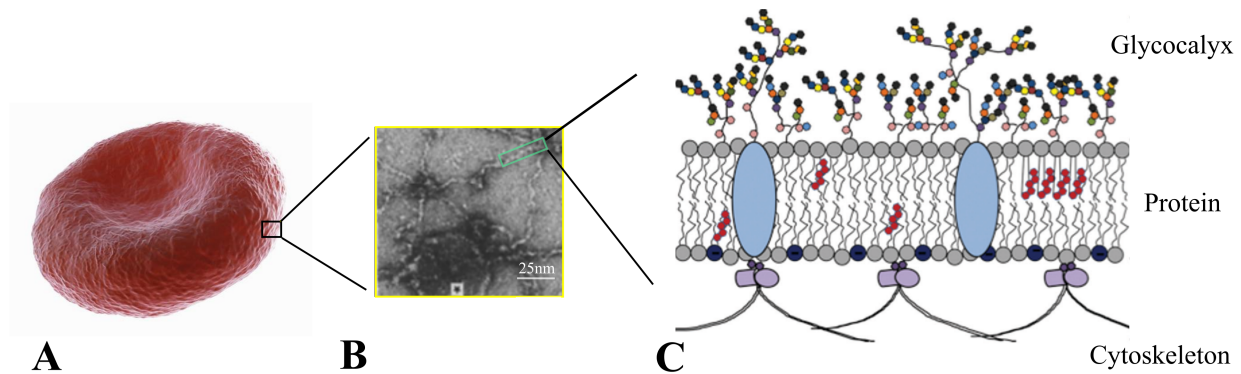


Figure 1.3: Depiction of a resting RBC and its structural elements. (A)- Illustration of a stationary RBC in the discocyte form. (B)- Cross-sectional view of the RBC membrane, revealing the spectrin network, comprising a carbohydrate-rich glycocalyx, a lipid bilayer with bending resistance, and an underlying protein network serving as the membrane skeleton^[25]. (C)- Close-up of the spectrin network, displaying the composition of the spectrin lipid bilayer, glycocalyx, and proteins. *Modified by Inkscape, and reprinted with permissions from both Kim et.al and Atukorale et.al*^[25,26].

1.2.3 Hemoglobin Content and Oxygen Transport

Each RBC contains millions of densely packed hemoglobin molecules, which are crucial for its primary function of oxygen transport. Hemoglobin is a complex protein composed of four subunits, each capable of binding one oxygen molecule, allowing a single hemoglobin molecule to carry up to four oxygen molecules. This high capacity for oxygen binding and release underlies the efficiency of RBCs in transporting oxygen from the lungs to peripheral tissues. The hemoglobin molecule in adults consists of two α chains and two β chains (see Figure 1.4 and Table.1.1), each surrounding a heme group^[27,28]. The heme group contains an iron ion (Fe^{2+}), which is the actual site of oxygen binding. This iron ion can reversibly bind to an

oxygen molecule (O_2), facilitating oxygen absorption and release as blood circulates between the lungs and tissues^[29].

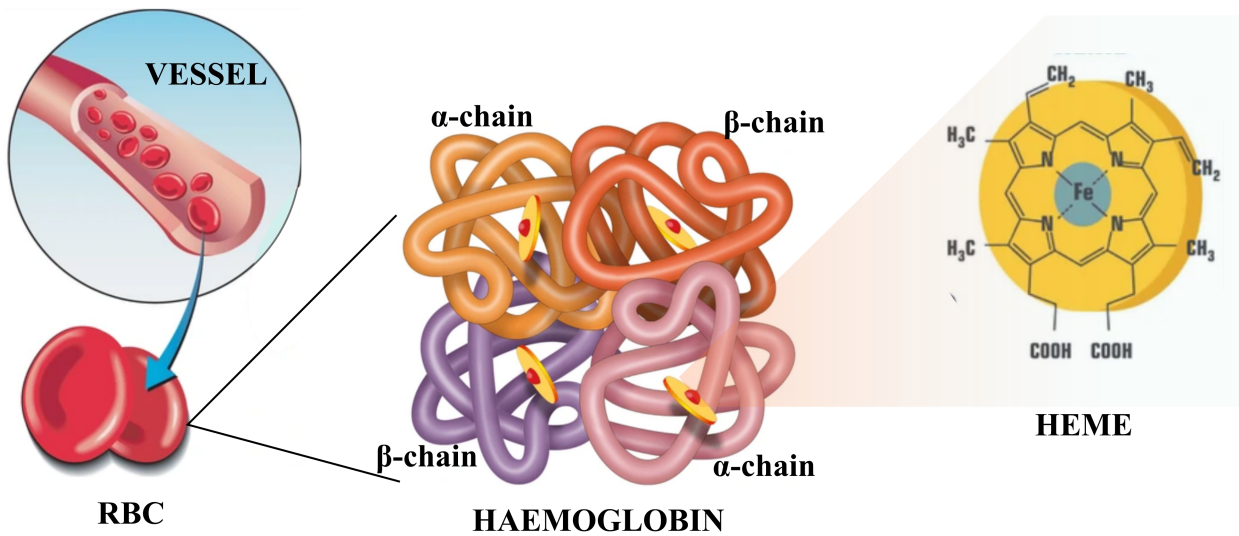


Figure 1.4: The image illustrates the structural components of hemoglobin in RBC. On the left, it depicts a vessel through which an RBC travels. The RBC itself is represented as a biconcave disc. The central portion showcases the intricate structure of the hemoglobin molecule, comprising α -chains and β -chains arranged in a quaternary structure. The α - and β -chains are polypeptide subunits that constitute the hemoglobin tetramer. On the right, the heme prosthetic group is depicted, consisting of a porphyrin ring with a central iron (Fe) atom capable of reversibly binding oxygen molecules. The chemical structure of the porphyrin ring, with alternating methine ($=CH-$) bridges and pyrrole rings, is also illustrated. *Source:* Shutterstock^[30].

The oxygen transport function of RBCs depends not only on the properties of hemoglobin but also on the structural integrity and deformability of the RBCs. Disorders affecting hemoglobin structure or function, such as sickle cell disease or thalassemia, can significantly impair oxygen transport. In sickle cell disease, for example, a mutation in the beta-globin gene results in abnormal hemoglobin (Hemoglobin S), which polymerizes under low oxygen conditions, causing RBCs to become rigid and sickle-shaped. These deformed cells can occlude capillaries, leading to pain, tissue hypoperfusion, and organ damage^[31]. Hemoglobin is a highly efficient oxygen carrier due to its structure, cooperative binding, and regulatory mechanisms that modify its oxygen affinity in response to the body's metabolic needs. Understanding these mechanisms provides insight into how RBCs perform their vital role in oxygen transport and how disorders affecting hemoglobin can lead to significant clinical consequences.

1.2.4 Lifespan and Senescence

The average lifespan of a RBC is approximately 120 days. During their lifetime, RBCs undergo various changes affecting their structure and function^[37–39]. These changes result from continuous mechanical and oxidative stresses that RBCs endure as they circulate through the body. One of the primary changes in aging RBCs is the alteration in cell membrane composition and organization^[37,40]. The lipid bilayer and membrane proteins become more susceptible to oxida-

Table 1.1: Kinetic constants (k' and l' are the energy of association, and k and l of dissociation^[32]) for the reaction with O₂ and CO respectively, of the isolated α and β chains of human Hemoglobin at pH 7.0 and 20°C. Based on data from^[33–36] with permission.

	Oxygen		Carbon monoxide	
	k' ($M^{-1} \text{sec}^{-1}$) $\times 10^{-7}$	k (sec^{-1})	l' ($M^{-1} \text{sec}^{-1}$) $\times 10^{-6}$	l (sec^{-1}) $\times 10^3$
α -SH	4.9	28	4.6	13
α -PMB	5.0	31	3.9	16
β -SH	6.8	16	4.5	8
β -PMB	7.1	156	2.4	27

tive damage, affecting the cell's ability to maintain its biconcave shape^[40–43]. Loss of membrane integrity and oxidation of membrane proteins and lipids lead to reduced cell deformability, making it difficult for aged RBCs to navigate through narrow capillaries and sinusoids. Another crucial factor in RBC aging is hemoglobin degradation. Over time, hemoglobin undergoes oxidative modifications^[44,45], leading to the formation of methemoglobin and hemichromes, these later are forms of hemoglobin that cannot efficiently bind oxygen. These oxidized forms of hemoglobin can precipitate and form Heinz bodies; aggregates that adhere to the inner surface of the RBC membrane; further impeding cell flexibility and promoting recognition and removal by splenic phagocytes^[46]. As RBCs age, they lose membrane components through the release of microvesicles containing phosphatidylserine and other altered proteins^[47]. The exposure of phosphatidylserine on the outer leaflet of the cell membrane acts as an "eat-me" signal for phagocytes, facilitating the phagocytosis of old RBCs by the spleen and liver^[48]. The spleen plays a critical role in removing aged RBCs. As RBCs pass through the spleen, they must navigate through the slits between the endothelial lining of splenic sinusoids^[4,49]. The mechanical challenge of squeezing through these narrow slits acts as a filter, selectively trapping RBCs with reduced deformability^[38,50]. Phagocytes in the red pulp of the spleen then engulf these trapped, aged RBCs. Additionally, Kupffer cells in the liver contribute to the removal of senescent RBCs from circulation^[47,51].

Efficient removal of aged RBCs is vital for maintaining balance in the circulatory system. The bone marrow continuously produces new RBCs to replace those removed, ensuring a stable pool of functional RBCs to maintain oxygen delivery throughout the body^[39,52]. Imbalances in RBC production and removal can lead to various hematological disorders, such as anemia or polycythemia^[53].

1.3 RBC Flow in Capillaries

1.3.1 Deformability and Adaptation of RBCs

We saw previously that the RBC ability to deform is largely assigned to the unique structural properties its membrane and cytoskeleton, which provide both flexibility and mechanical stability^[43]. RBCs can adapt to various shapes during blood flow, influenced by factors such as flow velocity, shear stress, and the physical properties of the surrounding environment^[54].

In vivo and in vitro studies have demonstrated several distinct shapes that RBCs can assume^[55]. For instance, under low stress conditions, RBCs typically maintain their biconcave discoid shape (Figure 1.2.A and Figure 1.3.A), which optimizes the surface area-to-volume ratio for efficient gas exchange^[56]. As shear stress increases, RBCs can elongate into an elliptical shape, enhancing their ability to traverse narrow spaces^[57,58]. One of the most interesting shapes is the "parachute" or "croissant" shape, where the cell flattens and elongates significantly^[59] while maintaining a center-flow profile. At higher shear rates, RBCs can changeover to a "slipper" shape^[60], the cell exhibits an asymmetric and off-center profile (results are described in Figure 1.7). This shape is often observed at moderate shear rates and is believed to result from a balance between hydrodynamic forces acting on the cell and its intrinsic elastic properties^[55]. These morphological adaptations are essential for reducing resistance and facilitating smooth passage through capillaries^[57,61]. The various shapes adopted by RBCs during blood flow have significant implications for their functions and overall blood flow dynamics^[62]. For example, the slipper shape, although less efficient in oxygen transport compared to the biconcave disc, may help prevent occlusion in narrow or partially obstructed capillaries^[63]. Conversely, the parachute shape allows for rapid transit through extremely narrow passages, ensuring continued oxygen delivery to tissues even under high flow conditions^[64,65]. Furthermore, the ability of RBCs to deform and adapt their shape is also vital for their survival and longevity^[66]. Cells that lose their deformability due to aging or pathological conditions are more susceptible to entrapment and destruction in the spleen, leading to reduced lifespan and impaired oxygen-carrying capacity^[16]. With the previous investigations in RBC flow dynamics^[17,23], it becomes evident that the interaction between deformability and mechanical forces is pivotal to both physiological and pathological behaviors of RBCs.

In single-cell flow at the microscopic level, red blood cells (RBCs) exhibit a variety of stable and dynamic shapes that are heavily influenced by several factors, including the biophysical properties of the cell, the degree of channel confinement, flow velocity, and the properties of the surrounding medium. Understanding these behaviors is crucial for deciphering how RBCs function in microcirculatory environments, where these factors combine to determine cell morphology and dynamics.

Under steady flow conditions, RBCs exhibit several distinct dynamic states (illustrated in Figure 1.6). One such state is tank-treading (TT), where the membrane of the RBC rotates

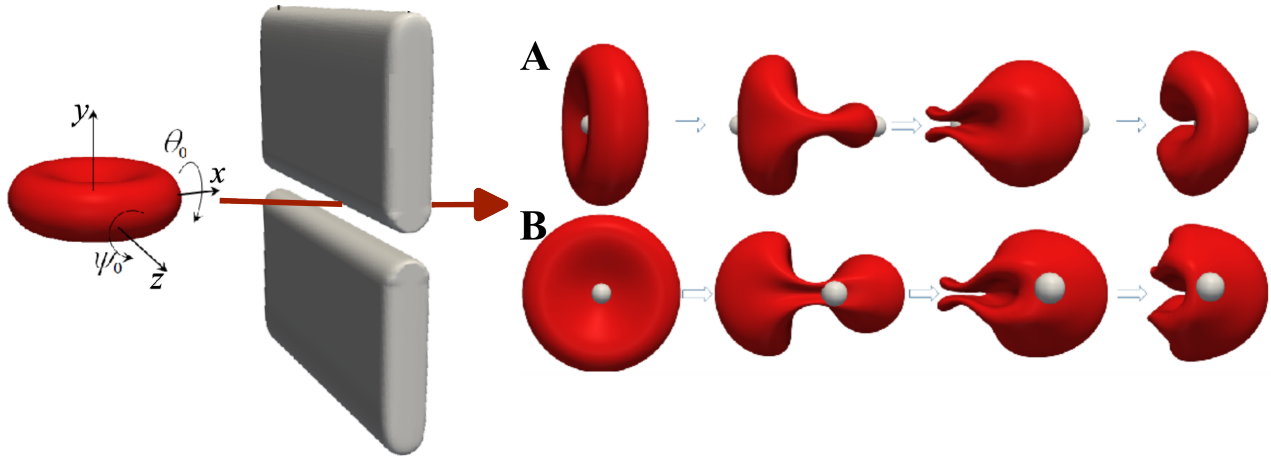


Figure 1.5: Shape deformations of the cell as it passes through the slit with two different initial shape cases: $\theta_0 = 0^\circ$; $\psi_0 = 90^\circ$ (A) and $\theta_0 = 90^\circ$; $\psi_0 = 0^\circ$ (B)^[67]. Flow is from left to right. In both cases (A) and (B), the cell deforms significantly as it transits through the narrow slit. The sequence shows the dynamic changes in cell shape, starting from a biconcave disc and transitioning through various deformed states, including elongated and squeezed forms, before finally passing through the slit. The dimple elements, indicated by white spheres, trace the deformation pattern, illustrating how different initial orientations impact the cell's deformation pathway and overall shape during passage. *Reproduced with permission granted by Salehyar et.al*^[67].

continuously around the cytoplasm (see Figure 1.6.C). This phenomenon occurs when the cell is exposed to shear flow, particularly at higher shear rates. The TT allows the cell to maintain a stable orientation relative to the flow direction, effectively reducing the viscous resistance encountered by the cell. The work of Dupire et al.^[55] provides detailed insights into this behavior, showing how tank-treading stabilizes RBC shape and alignment along the flow direction. The frequency of TT is directly proportional to the applied shear rate and serves as a mechanism for energy dissipation, preventing excessive cell deformation. An important dynamic state is tumbling (Figure 1.6.A), which occurs when the RBC undergoes flipping motion as it moves through the fluid. This pattern typically emerges at lower shear rates or in environments where the viscosity of the surrounding medium is low. Tumbling is characterized by the cell rotating end-over-end, a result of the balance between the external torque exerted by the shear flow and the internal elastic forces of the cell. The research by Apakarian et al.^[60] describes the delicate equilibrium required for this phenomenon, highlighting how both medium viscosity and shear rate influence whether the cell will tumble or undergo TT. Their findings show that as the shear rate increases, a transition from tumbling to TT can occur, indicating a shift in the cell's dynamic response to flow. Rolling is another significant dynamic state that RBCs can display in microflow (see Figure 1.6.B), particularly under specific flow conditions. Unlike tumbling, where the cell flips completely, rolling involves the RBC rotating around one of its axes while maintaining contact with the vessel wall or the boundary of the microchannel. This motion is typically observed under low shear conditions or in environments where the cell experiences asymmetrical forces, such as proximity to the vessel wall or within a capillary. Rolling can be viewed as a transitional behavior between tumbling and TT, where the RBC membrane par-

tially rotates while the cell remains in a relatively stable orientation to the flow direction. This behavior is especially important in the context of blood flow in the microcirculatory system, where RBCs frequently interact with the endothelium of blood vessels. Studies by Fisher et al., along with Dupire^[55,68], have detailed the mechanical properties and conditions influencing rolling, emphasizing its dependence on shear rates and membrane elasticity. Computational models by Fedosov et al.^[69] further explain how rolling dynamics are affected by interactions with microchannel walls and varying flow conditions, illustrating the complexity of RBC behavior in confined environments. Other dynamic behavior, known as snaking, occurs when an RBC takes on an elongated shape and moves in a wavy pattern through capillaries. This behavior often arises in highly confined environments, where the cell's deformability allows it to adapt its shape to navigate narrow passages. Snaking is particularly important in microchannels where the dimensions of the RBC are comparable to the channel width, requiring the cell to elongate and deform to maintain its flow path. Oscillating, also referred to as breathing, is a more complex oscillatory behavior where the RBC fluctuates between different orientations while maintaining TT motion. This state is typically observed at intermediate shear rates, where the forces acting on the cell are sufficient to induce oscillations but not strong enough to completely overcome the membrane's elastic resistance. The oscillations involve periodic changes in the cell's inclination relative to the flow direction, with the membrane's TT motion adjusting to these shifts. Apakarian et al.^[70] further explored this behavior, demonstrating that the frequency and amplitude of oscillations are sensitive to both shear rate and the mechanical properties of the RBC membrane.

Research by Lanotte et al.^[73] further investigates the dynamic shapes of RBCs, particularly under conditions simulating microcirculatory flow. Their findings emphasize the role of RBC deformability in controlling blood's shear-thinning behavior, a property that enables blood to maintain its fluidity even at low shear rates. In their study, Lanotte et al. used high-resolution imaging techniques to capture the various dynamic shapes of RBCs in flow, providing visual evidence of how these shapes evolve in response to changing flow conditions. They identified that RBCs can exhibit a range of transitional shapes between the stable states described above, depending on the interaction between the cell's internal viscosity, membrane elasticity, and external shear forces. These dynamic behaviors of RBCs are not only essential for understanding microcirculatory blood flow but also have implications for various physiological and pathological conditions. Moreover, understanding these dynamics is crucial for designing microdevices aimed at simulating or manipulating blood flow for therapeutic purposes.

1.3.2 Bi-Stability of Single RBC Through Capillary Flow

Mostly, in strongly confined rectangular channels of dimensions comparable to the dimension of RBCs, two main shapes can be distinguished^[74–76]: the croissant and the slipper shape.

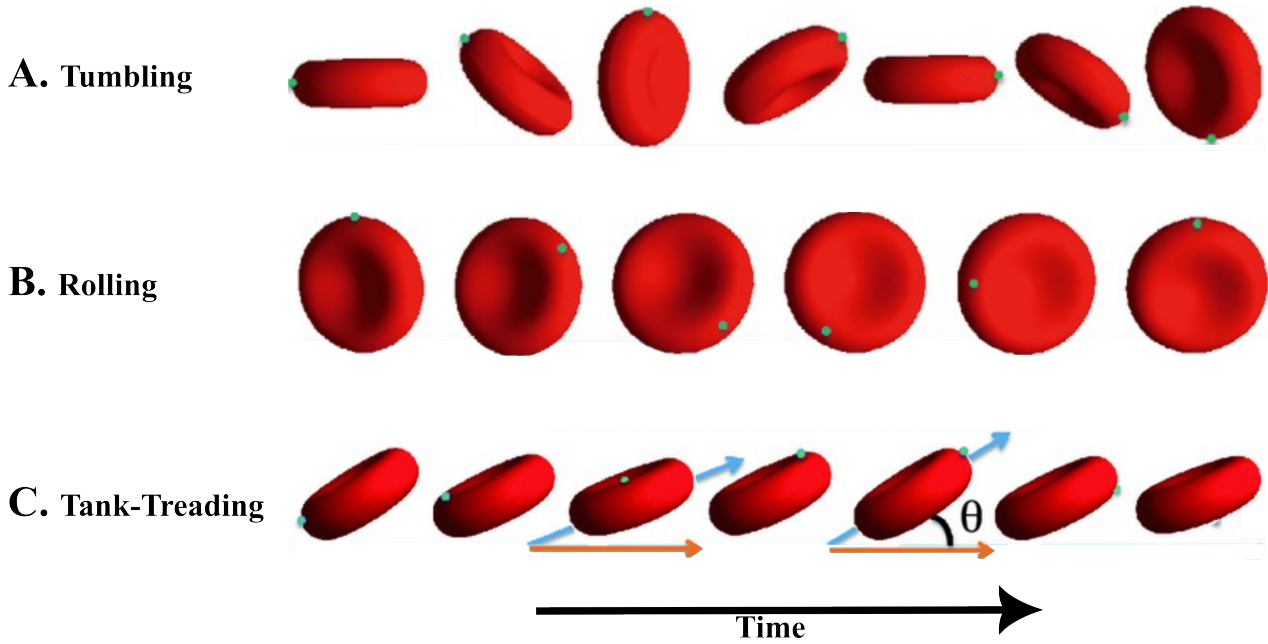


Figure 1.6: Illustration of RBC motion in moderate shear flow^[71]: Flow direction is left to right, with increasing shear stress from (A) to (C). The blue dot marks a moving membrane element. (A) Tumbling/flip-flopping at very low shear stress ($< 0.05\text{--}0.1Pa$). (B) Rolling at intermediate shear stress ($0.1\text{--}0.15Pa$). (C) Tank-treading/swinging at higher shear stress ($> 0.15Pa$), with the axis in the shear plane and slight oscillation. The angle of inclination is presented with θ . *Reproduced with permission from Viallat et.al*^[72].

The croissant-like shape dominates the scene in the case of low flow velocities, whereas the asymmetric slipper shape develops at larger cell velocities. Guckenberger et al.^[75] also studied those two dominant RBC shapes within a rectangular microfluidic channel of ($W = 12\ \mu\text{m}$, $H = 10\ \mu\text{m}$) and proposed the concept of RBC shape phase diagram. See Figure 1.7 showing the proportion of stable croissant and slipper shapes as a function of the cell velocity Figure 1.7.A They concluded that the croissant shape dominated for cell velocities lower than $5\ \text{mm}\cdot\text{s}^{-1}$, and that the slipper shape was more common at higher velocities with cell velocity above $5\ \text{mm}\cdot\text{s}^{-1}$, but still slower compared to the croissant shape due to a centering flow; see Figure 1.7.B. Moreover, they identified that the highly deformable RBC exhibits strong flow-shape coupling, its shape being essentially coupled with its equilibrium position in the cross-section and along the channel width. Other than the shape phase diagram, various other forms of flowing RBCs have been obtained with microcapillaries; more precisely, under the following conditions of pathology: acanthocytes and their complementary pathological croissant and slipper shapes^[77,78]. The cell-shape classifying methods were used to evaluate changes in the microcapillary flow behavior of neuroacanthocytosis syndrome patients, COVID-19 patients, and in dialysis patients^[77–80], and as a biomarker and functional diagnostic technique for a variety of pathologies and quality assessment of stored blood. Numerical simulations have also presented various steady and dynamic RBC shapes in round microcapillaries.

The work of Fedosov et al..^[81] presented a complete shape phase diagram that included sta-

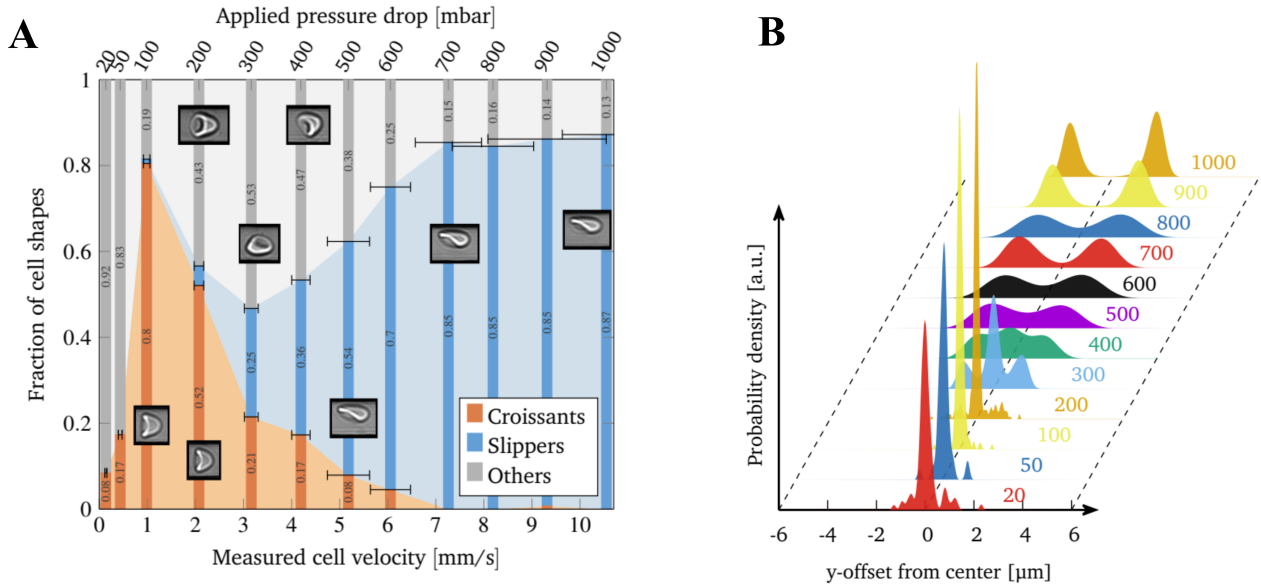


Figure 1.7: (A) Phase diagram of both stable shapes (croissant and slipper) highlights the fractions and the shape transition following the cell’s velocity (bottom axis) and the pressure drop applied to the channel (top axis). The images are screenshots of the cell under each shape category, and the error-bars reveal the velocity variations of each stable shape at fixed pressure value. (B) Probability density function as distributions of the lateral component of the center of mass from the global amount of RBCs under fixed pressure drop. *Originally published in Guckenberger et.al^[75] reproduced here with permission.*

tionary parachutes, swinging slippers, tumbling and snaking discocytes, all as a function of the channel confinement and the shear rate in the system with a circular cross-section. Parachute-shaped RBCs, usually called croissants in microfluidic experiments with square or rectangular microchannels, become more asymmetric in rectangular channels. Similarly, parachute-like RBC in round capillaries flow in the tube center while slippers are displaced further from the channel center (see Figure 1.7.B). The occurrence of these shapes and the transition between the dynamic shapes critically depend on the properties of the RBCs and viscosity contrast between RBC cytosol and blood plasma^[82]. There are very few detailed experimental investigations of how this slight variation in channel confinement affects both the RBC capillary flow and the phase diagram of shapes. Currently, PDMS microchannels fabricated by soft lithography techniques remain an everyday platform for research into micro-scale flow biological systems^[83,84]. However, it remains of paramount importance to understand how channel confinement affects the various shapes of RBCs normally adopted for the in vitro microvascular flow studies. Recently^[85,86], the single-cell flow of RBCs was studied while passing through six microfluidic channels of different dimensions. It has been able to introduce small changes in the order of few micrometers on the RBC phase diagram, the equilibrium position of the cells, their elongation, and the appearance of unstable cell shapes. This work concludes that for the stable slipper-like shapes, one requires a rectangular cross-section, while in square channels croissant-like cells appear. Quantitatively, for channel dimensions larger than 10 μm , both stable croissant and slipper shapes disappear and highly dynamic other RBC shapes appear. For

both croissants and slippers, the obtained deformations are quantified with a non-dimensional deformation index, DI, which scales in microchannel shear rate, highly relevant for biomicrofluidic technologies aiming at the assessment of RBC deformability.

1.4 Changes in RBC Flow Characteristics

1.4.1 Age-Related Changes

As RBCs age, they undergo various biochemical and biomechanical changes that can significantly impact their deformability and rheological properties^[87]. These alterations are crucial because they influence blood flow dynamics and, consequently, the efficiency of oxygen delivery to tissues^[4]. Age-related changes in RBCs have been extensively studied through both *in vivo* and *in vitro* experiments, shedding light on their implications for overall health and well-being^[88].

In vivo studies have demonstrated that senescent RBCs exhibit decreased deformability due to modifications in membrane composition and cytoskeletal structure^[89]. For example, older RBCs tend to lose membrane surface area while gaining intracellular viscosity, resulting in less flexible cells that struggle to navigate through the microvasculature^[90]. This decreased deformability is often attributed to the progressive accumulation of oxidative damage and the loss of key cytoskeletal proteins over time^[91,92]. Furthermore, age-related changes in the phospholipid composition of the RBC membrane can alter membrane fluidity, exacerbating the rigidity of older cells^[93]. *In vitro* studies have corroborated these findings, revealing specific mechanical properties of aged RBCs under controlled conditions^[94]. Techniques such as ektacytometry and micropipette aspiration have been employed to quantify the deformability of RBCs at different stages of their lifespan^[25]. These studies consistently show a marked decline in deformability with increasing cell age, highlighting the challenges faced by older RBCs in maintaining adequate blood flow and oxygen delivery^[54,95,96]. Additionally, the increased tendency of aged RBCs to form echinocytes—spiculated cells—has been observed, which further impairs their flow characteristics^[43,97,98].

Storage age also plays a critical role in altering RBC properties, as evidenced by numerous studies on stored blood units used for transfusion^[99]. During storage, RBCs undergo a series of metabolic and structural changes collectively referred to as the "storage lesion"^[100]. These changes include alterations in cell morphology, decreased ATP levels, and increased membrane rigidity, all of which contribute to reduced cell deformability and impaired microcirculatory flow upon transfusion^[101,102]. Studies using advanced imaging techniques have shown that stored RBCs often develop a spherical shape, making them less capable of traversing capillaries efficiently^[103,104]. Donor age is another factor influencing the properties of RBCs^[105,106]. Research has indicated that RBCs from older donors exhibit different baseline characteristics compared to those from younger donors^[107,108]. For instance, RBCs from older individuals tend to have

shorter lifespans and reduced deformability even before any *in vivo* aging or storage effects are considered^[109]. This is significant for transfusion medicine, as the donor's age can affect the quality and efficacy of transfused blood^[110,111]. Studies have shown that the blood from older donors may lead to less favorable transfusion outcomes, emphasizing the need for age-matched blood donations in certain clinical scenarios^[40,112].

Overall, age-related changes in RBC flow characteristics have profound implications for vascular health and disease. As RBCs age, their ability to deform and travel through the microvasculature diminishes, leading to potential reductions in tissue oxygenation and contributing to conditions such as anemia, cardiovascular disease, and impaired wound healing. Understanding these changes is crucial for developing strategies to mitigate the negative effects of aging on RBC function and for optimizing blood storage and transfusion practices.

1.4.2 Influence of Membrane Rigidity on Capillary Transit

The rigidity of RBC membrane is a crucial factor influencing the cell's ability to navigate through the narrow and tortuous pathways of the microcirculation^[113]. Membrane rigidity determines not only the deformability of RBCs but also their capacity to maintain optimal blood flow and efficient oxygen delivery to tissues^[114]. Changes in membrane rigidity are often linked to various pathophysiological conditions, impacting RBC transit time and overall functionality^[115].

In vivo and *in vitro* studies have extensively explored the effects of membrane rigidity on RBC behavior^[54]. Increased membrane rigidity is typically observed in conditions such as hereditary spherocytosis, diabetes mellitus, and sickle cell disease^[116]. These conditions are characterized by structural alterations in the RBC membrane and cytoskeleton, leading to a decrease in cell deformability^[49]. For instance, in hereditary spherocytosis, mutations in membrane proteins result in spherically shaped RBCs that are less deformable and more prone to hemolysis^[117]. Studies using micropipette aspiration and ektacytometry have shown that these rigid RBCs exhibit significantly impaired deformability, hindering their ability to pass through capillaries efficiently^[24,118]. *In vitro* studies have provided valuable insights into the mechanical properties of RBC membranes and their impact on cell function^[96]. Techniques such as optical tweezers and atomic force microscopy have been used to measure the elasticity and stiffness (see Figure 1.8) of RBC membranes^[120]. These studies have demonstrated that increased membrane rigidity correlates with reduced cell deformability and impaired microcirculatory flow^[121,122]. Furthermore, RBCs with increased membrane rigidity are more likely to become trapped in the spleen, leading to their premature destruction and contributing to anemia^[123–125]. Experimental tools to manipulate and rigidify the RBC membrane have been developed to study the effects of altered rigidity on RBC behavior^[126]. One such method involves the use of chemical agents like diamide, which induces cross-linking of membrane proteins, thereby increasing mem-

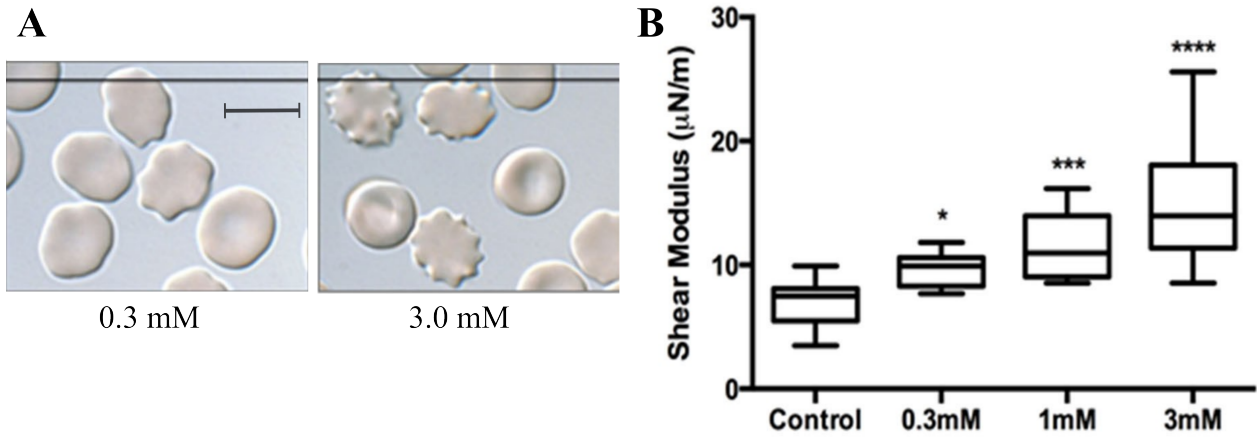


Figure 1.8: Exposure to oxidants induces significant alterations in RBC morphology and biomechanical properties^[119]. (A) Differential interference contrast (DIC) images show RBCs treated with varying concentrations of the oxidizing agent diamide, illustrating dose-dependent morphological changes (Scale bar = 10 μm). The images depict a transition from the typical biconcave shape to more irregular and spiculated forms as diamide concentration increases. (B) Quantitative analysis of diamide-induced changes in membrane shear modulus, reflecting alterations in membrane deformability. The box plots represent the shear modulus for control and diamide-treated RBCs at concentrations of 0.3 mM, 1 mM, and 3 mM. Data are presented as median \pm range. Statistical significance is indicated as follows: * ($p < 0.05$), ** ($p < 0.01$), *** ($p < 0.001$), **** ($p < 0.0001$). Adapted from Sinha *et.al*^[119].

brane stiffness^[127]. In vitro experiments using diamide-treated RBCs have shown a significant reduction in cell deformability and an increase in transit time through microfluidic channels designed to mimic capillary networks^[96,128]. Another approach involves genetic modifications to induce rigidity in RBC membranes, allowing researchers to study the physiological consequences of altered membrane properties in animal models^[4]. The implications of membrane rigidity on capillary transit and RBC function are profound. Increased rigidity not only hampers the mechanical ability of RBCs to deform and pass through narrow capillaries but also affects their interaction with endothelial cells and other blood components. This can lead to increased vascular resistance, impaired tissue oxygenation, and a higher risk of vascular complications. Understanding the factors that influence membrane rigidity and developing strategies to mitigate its effects are crucial for improving the management of diseases associated with altered RBC deformability.

1.5 Scope and Purpose of The Study

The remarkable ability of RBCs to undergo morphological changes in response to various environmental factors forms the core of this thesis, providing a comprehensive analysis of their morphodynamic behavior. This research is structured into three distinct yet interconnected phases, each contributing to a detailed understanding of RBC deformability under confined conditions with different alterations.

Influence of Geometrical Structure on RBC Morphology: The initial phase of this

study examines the impact of the surrounding environment’s geometrical structure on the morphological changes of RBCs. This investigation underscores the crucial role that cellular flexibility plays in enabling efficient function within capillaries, where the geometric configuration of micro-channels is of paramount importance. RBCs possess exceptional morphological adaptability, which directly influences blood flow dynamics. This adaptability serves as a diagnostic tool in certain medical applications and represents the primary measure for assessing cell deformability^[11,76,78]. While significant advancements have been made in understanding how external factors such as vessel size and flow velocity affect RBCs, the effects of confinement arising from microchannels remain relatively understudied^[108,129,130]. This research focuses on the intricate interplay between microchannel geometry and RBC behavior in response to imposed flow, with particular emphasis on how channels of varying shapes influence the cells’ ability to maintain stable forms^[19]. The findings highlight the significance of rectangular microchannels, especially those with a height approximating the diameter of an RBC. It has been observed that a confinement ratio, expressed as $\chi = D_{RBC}/D_h$ (further details provided in section I.2), exceeding 0.9 gives rise to well-known and representative equilibrium shapes, such as croissant and slipper-like forms^[74,75,78,131,132]. These distinct shapes, observed in laboratory experiments, maintain specific equilibrium positions within the channel cross-section and exhibit a tendency to elongate under higher shear rates. Conversely, less confined channels were found to display a broader spectrum of unstable shapes, experiencing diverse morphological dynamics^[73]. This investigation aims to establish a robust experimental framework that will not only advance our understanding of RBC behavior in confined environments but also provide valuable insights for the development of sophisticated microfluidic devices for single-cell analysis^[133]. The results obtained from this phase of the study have far-reaching implications for both fundamental research in cellular biology and practical applications in biomedical engineering.

Impact of Density and Membrane Rigidity Variations on RBC Behavior: The second phase of this research extends the investigation to examine the influence of variations in density and membrane rigidity on RBC behavior. By selectively isolating cells based on these properties, this study explores how the efficiency of microcirculation is affected by RBC deformability, particularly in the narrow segments of the vascular network^[134]. Despite the well-documented alterations in the physical properties of RBCs with aging, the extent to which their shape-adapting ability evolves remained poorly understood^[135]. The results presented herein elucidate how age-related rigidification of the cell membrane influences RBC behavior under both natural conditions and experimental manipulation. In an effort to simulate changes in membrane rigidity, freshly isolated cells were chemically stiffened using diamide and compared with older RBCs^[136]. The findings provide compelling evidence of a progressive loss of stable, asymmetric slipper-like shapes at higher velocities, most notably in older or chemically stiffened cells. These off-center slipper shapes in the microchannel diminish with increasing membrane

stiffness. Intriguingly, older cells demonstrate a higher propensity for forming stable, croissant-like shapes symmetrically aligned along the channel axis. This tendency is suppressed when the cells' membranes are stiffened with diamide, underscoring the intricate interplay between age, membrane properties, and RBC deformability^[137]. This phase of the study contributes significantly to the ongoing discourse on how intrinsic cell properties may impact blood flow dynamics and how RBC deformability affects vascular health.

Quantitative Assessment of RBC Deformability: The final phase of our research provides a comprehensive overview of RBCs, considering both density and elastic properties of the membrane, and quantitatively assesses this crucial property. Deformability has long been recognized as one of the most critical factors influencing the flow behavior of RBCs through capillaries and other narrow blood vessels^[138]. Previous studies have employed various approaches to characterize RBC deformability in terms of stiffness, flexibility, and elongation under different flow conditions. The present study utilizes an innovative experimental strategy to investigate the dynamics of individual RBCs as they navigate through microchannels of varying widths. This process involves subjecting cells to compression through ultra-narrow channels followed by expansion through wider channels, offering a unique perspective on their ability to adapt to fluctuating mechanical stresses^[139]. To quantify this adaptation, the Deformation Index (DI) is employed as a specific measure of how RBCs respond to compression-expansion within a microfluidic setup^[140]. The model results identify two key factors density and cell membrane stiffness as primary contributors to the development of the DI. A higher value for membrane stiffness correlates with a greater loss of deformability, which in turn directly relates to reduced efficiency in blood flow^[141]. This section of the thesis discusses how these findings contribute to our understanding of various physiological phenomena and their potential implications for diagnostic and therapeutic applications in hematology and vascular medicine.

In conclusion, this comprehensive study of RBC morphodynamics provides valuable insights into the complex interplay between cellular properties, environmental factors, and blood flow dynamics. The findings presented herein have significant implications for our understanding of microcirculation and may inform the development of novel diagnostic tools and therapeutic strategies for a range of hematological and vascular disorders^[135].

EXPERIMENTAL MATERIALS AND METHODS

Contents:

2.1	Blood Sample Preparation	24
2.1.1	Blood Extraction	24
2.1.2	Discontinuous Density Separation Sample	25
2.1.3	Diamide Solutions and Rigidification	27
2.2	Microfluidic devices	28
2.2.1	Silicon Wafer and Epoxy Mold	28
2.2.2	PDMS-based Chip	30
2.2.3	Sacles and Geometry	31
2.3	Recording and Exporting Raw Images	32
2.3.1	Microscope, Cameras and Lenses	33
2.3.2	Image Sequences	34
2.3.3	Single Particle Tracking	34

2.1 Blood Sample Preparation

Blood collection and red blood cells (RBCs) extraction are critical steps in many biological and medical applications^[142–144]. It is crucial to obtain high-quality blood samples to ensure accurate results. Different methods can be used for blood collection depending on the quantity required, and the extracted RBCs must be carefully separated from other cells and plasma to prevent contamination and loss of cells.

2.1.1 Blood Extraction

It is essential to obtain high-quality samples to ensure accurate results. When collecting blood from healthy volunteers, informed consent should always be obtained before proceeding^[145,146]. The amount of blood required for a specific experiment can vary, and different methods can be used depending on the quantity needed.

In all conducted *in-vitro* experiments, unless explicitly mentioned otherwise, a uniform blood withdrawal and preparation protocol was adhered to. The acquisition of blood from healthy donors strictly adhered to regulations and protocols sanctioned by the ethics commission of the "Ärztammer des Saarlandes" [Medical Association of the Saarland] (reference 24/12), ensuring compliance with ethical guidelines and standards. This meticulous approach underscores our commitment to maintaining consistency and ethical integrity throughout the experimental procedures. The routine for preparing the blood solutions and the handling follow the guidelines by Baskurt et al.^[147]. Blood withdrawal was executed through two distinct methods: a sterile needle puncture in the fingertip or venipuncture, where the blood was collected within a securely sealed vacutainer containing *ethylenediaminetetraacetic acid* (1.6 mg.mL^{-1} EDTA, SARSTEDT, Nümbrecht, Germany) as an anticoagulant. In the former approach, the total blood volume varied based on skin temperature and precise needle placement, spanning approximately $10 \mu\text{L}$ to $100 \mu\text{L}$. Conversely, the latter method maintained a fixed volume of 9 mL .

After blood is collected, the initial crucial step in isolating RBCs involves separating them from the other components, such as plasma. To achieve this separation, the collected blood is placed in a machine called a centrifuge. This machine spins the blood at a force of around $3000 \times g$ for a duration of 7 minutes. During this process, the formation of a compact pellet of (RBCs) at the container's bottom, along with an upper layer of autologous plasma and an intermediate layer containing white blood cells (WBCs) and platelets, also referred to as the buffy coat. Both the supernatant and buffy coat were carefully removed and discarded, leaving behind the pellet which was subsequently resuspended in isotonic phosphate-buffered saline (PBS) (Gibco PBS, Fisher Scientific, Schwerte, Germany) in the same quantity, following procedures outlined in reference^[148]. This washing procedure is repeated three times, each time ensuring that any remnants of plasma and platelets are removed. Additionally, this multi-step

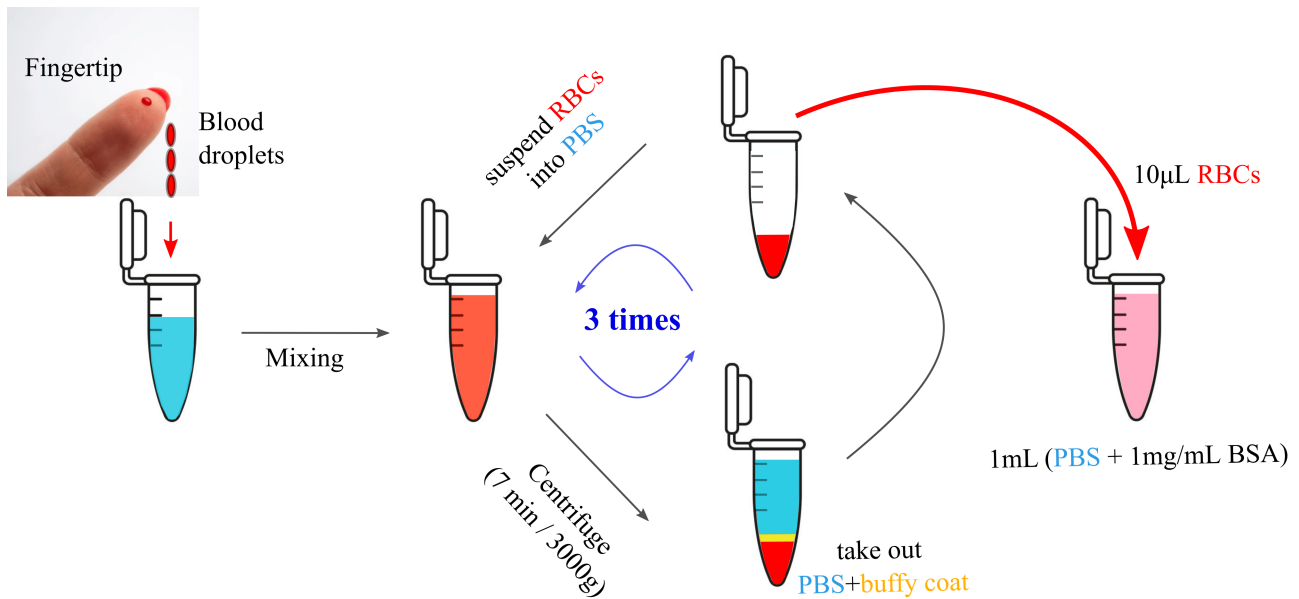


Figure 2.1: The extraction process of RBCs from blood. Left to right: a few droplets from the blood donor is diluted and mixed well into 1 mL of PBS solution. The centrifugation is necessary to apply enough force to separate blood by density of its components, the result then is the appearance of RBCs (bottom solution) due to the high density of the cells, a yellow buffy coat that contains thrombocytes (platelets) and leukocytes (white blood cells). By taking out PBS with the yellow layer we got only RBCs at the bottom. By repeating 3 times the washing process, a pure RBCs layer is obtained and will be diluted later to perform experiments with. *Eppendorf PCR Tubes sketches created using Biorender.*

washing process eliminates any impurities that might disrupt subsequent experiments.

With the washing complete upon the final centrifugation step, a suspension of 10 μ L from the pellet was mixed with a solution composed of 1 ml PBS and 1 mg bovine serum albumin (BSA). The inclusion of BSA aimed to inactivate the RBC surface, preventing the occurrence of the glass slide effect that could otherwise lead to morphological alterations in RBCs^[149]. As a result, the end solution attained a hematocrit level of approximately 1%, signifying the completion of the blood preparation process. A time frame of no more than 3 hours is maintained between the blood withdrawal and the actual experiment execution.

2.1.2 Discontinuous Density Separation Sample

The density of RBCs can be influenced by various factors such as the concentration of hemoglobin, the size of the cells, and the amount of water they contain. For example, in individuals with anemia, there is a lower concentration of hemoglobin in the RBCs, leading to a decrease in RBC density. In contrast, individuals with polycythemia have an increased concentration of RBCs, leading to an increase in RBC density.

Discontinuous density separation is a commonly used method for separating different types of cells or particles based on their density. This technique involves layering different solutions with increasing density in a tube and then centrifuging the tube to separate the cells or particles

based on their buoyancy. In the case of RBCs, a Percoll density solution is commonly used to generate different layers of increasing density from top to bottom.

Percoll is a colloidal solution that contains silica particles coated with polyvinylpyrrolidone (PVP). This solution can be used for density gradient centrifugation to separate cells or particles based on their buoyancy. The buffer Percoll solutions used for discontinuous density separation are typically obtained by mixing Percoll with distilled water, sodium chloride (NaCl), and other substances to achieve the desired density gradient. The buffer Percoll solutions are layered in a 14 mL tube with 5 layers of 2 mL each, arranged in increasing density from top to bottom. The least dense solution is at the top, while the most dense solution is at the bottom. The volume of each layer and the density of each solution depend on the specific experimental conditions and the desired separation parameters.

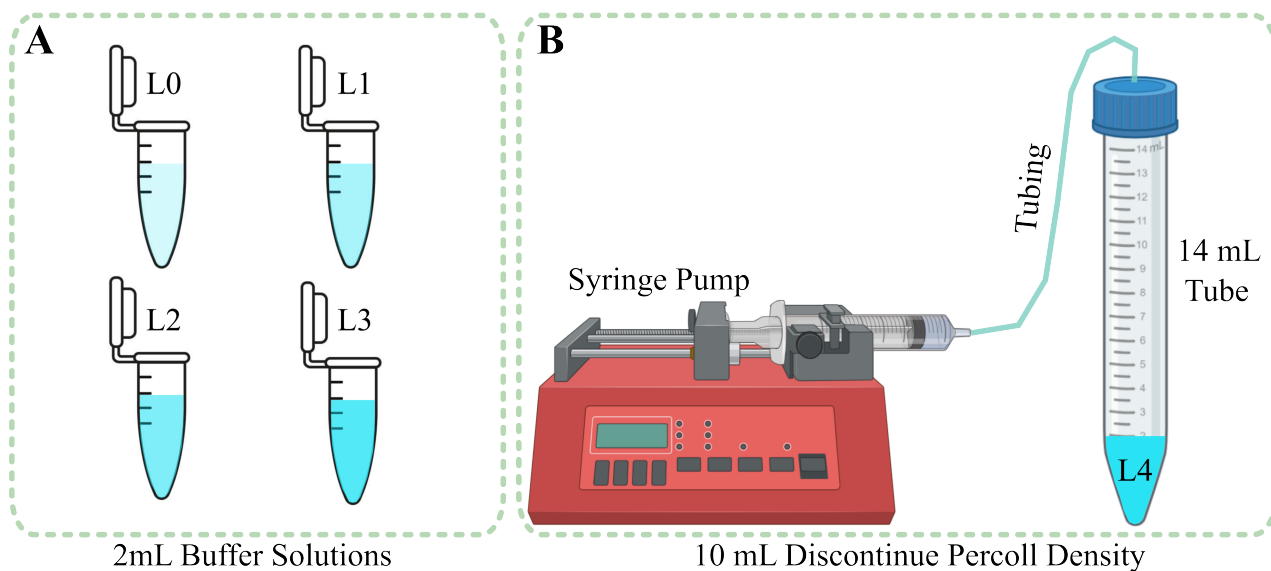


Figure 2.2: The protocol of separation of RBCs performed using Percoll increasing density buffer solutions^[150]: A. Solutions of 2 mL of each layer that construct the discontinuous density separation solution (L0-L4). Details about the production of these solutions are presented at the Table.2.2. B. Protocol to make the main separation solution, by carefully adding the layers one top of the other using a slow syringe pump injection of the buffer solutions (from high to low density). The denser layer L4 can be added using the normal liquide injector. *Elements are created using Biorender.*

To ensure proper layering of the buffer Percoll solutions, a syringe-pump is commonly used to gently dispense each solution into the tube. The syringe-pump (INJEKTOMAT 30, Fresenius Medizintechnik Bad Homburg, Typ Injekt 30 Nr. P84384YU) allows for precise control of the flow rate and volume of each solution, which is important for achieving a stable and reproducible density gradient. After the buffer Percoll solutions have been layered in the tube, 50% of distilled RBCs in phosphate-buffered saline (PBS) solution is gently added to the top of the tube. The tube is then centrifuged at a predetermined speed and duration to allow the RBCs to separate based on their density. After centrifugation, the tube is typically fractionated into different layers, and the RBCs in each layer are collected for further analysis or manipulation.

Table 2.2: Elements, densities and volumes to prepare the buffer solutions for each layer that constructs the main separation solution (see Figure 2.2).

Layers	Density (g/mL)	NaCl (μ L)	Percoll (μ L)	H_2O (μ L)
L0	1.085	182	1227	591
L1	1.092	182	1334	484
L2	1.101	182	1473	345
L3	1.107	182	1565	253
L4	1.122	182	1796	22

Discontinuous density separation of RBCs using Percoll gradient centrifugation is a widely used technique in various research fields such as hematology, immunology, and cell biology. This technique allows for the separation of RBCs based on their density, which can be useful in studying various cellular processes such as cellular metabolism, cell signaling, and cellular differentiation. Additionally, this technique can also be used to isolate specific subpopulations of RBCs, which can be useful in studying the pathophysiology of various diseases such as sickle cell anemia, thalassemia, and malaria.

2.1.3 Diamide Solutions and Rigidification

Red blood cells lack nuclei or organelles and have a plasma membrane made up of a lipid bilayer and integral membrane proteins. The membrane serves several functions, including maintaining cell shape and regulating gas exchange. RBCs can undergo shape changes and are highly deformable, allowing them to pass through narrow capillaries.

RBC membrane rigidification makes the membrane less deformable and more resistant to shape changes. Diamide, a sulfhydryl reagent (Sigma-Aldrich, Taufkirchen, Germany), can induce membrane rigidification by forming disulfide bonds between membrane proteins. To prepare diamide solutions, four different concentrations of diamide: 0 mM (control), 0.5 mM, 1 mM, and 2 mM (Figure 2.3.A.a-d respectively) will be prepared in 2 mL of PBS. After preparing the diamide solutions, 50 ch : 1 μ L of RBCs will be added to each solution (Figure 2.3.A) and incubated for 30 minutes at room temperature to induce membrane rigidification. Washing the RBCs several times with PBS will remove excess diamide and prevent further crosslinking. The washing process involves centrifugation of the RBCs to sediment them at the bottom of the tube, followed by pipetting out the diamide-containing supernatant (similar process as shown in Figure 2.1). Fresh PBS will then be added, and the process will be repeated several times. After washing, the rigidified cells will be resuspended in fresh PBS+(1 mg/mL)BSA and used for microfluidic experiments (Figure 2.3.B). The cells will be loaded into microfluidic channels, and their deformability and flow behavior will be analyzed under different flow conditions. These experiments will provide insights into how membrane rigidification affects RBC function and behavior in circulation.

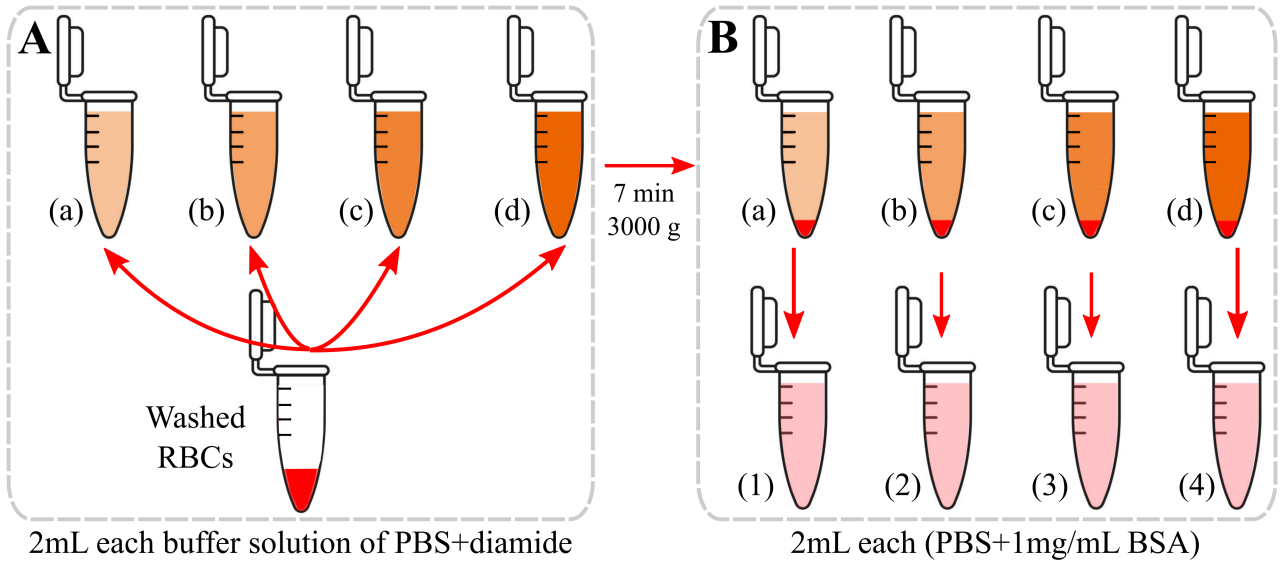


Figure 2.3: Illustration of the impact of increasing diamide concentrations on the degree of RBCs rigidification. The diamide concentrations (a-d) correspond to the solutions containing 0, 0.5, 1 and 2 mM of diamide, respectively. The corresponding numerical labels (1-4) denote diluted samples of $H_t = 1\%$ RBCs treated with each respective diamide concentrations. RBCs are treated with diamide, followed by careful washing, resulting in a precisely controlled suspension of RBCs (A). These suspensions are then diluted to achieve four distinct densities of diamide (A.a-d). This treatment and dilution process spans a duration of 30 minutes. Buffered solutions comprising a mixture of PBS, diamide, and RBCs undergo centrifugation (B). The centrifugation process involves the same method employed in Figure 2.1. Extracted RBCs are subsequently subjected to a similar dilution process, resulting in four solutions (B.1-4), each boasting a consistent $H_t = 1\%$. *Elements are created using Biorender.*

2.2 Microfluidic devices

This section provides an overview of the microfluidic setup employed in the experiments, which is composed of three primary steps. The first step involves preparing silicon wafer channels, while the second step is focused on creating an epoxy mold from the silicon wafer PDMS. The final step involves extracting the PDMS chip from the epoxy mold and bonding it with glass. While each of these steps is described in greater detail in the following section, this overview serves as a concise summary of the key components of the microfluidic setup.

2.2.1 Silicon Wafer and Epoxy Mold

Microfluidic channels are small, precise, and controllable channels typically used for the transport of fluids in microfluidic systems. These channels are often fabricated on silicon wafers using a combination of photolithography, etching, and other microfabrication techniques. The channels themselves are typically a few micrometers to a few hundred micrometers in width, with depths that are typically much smaller than the width. The channels are often coated with a variety of materials, including polymers, metals, and glass, to enhance their performance.

To create these channels on a silicon wafer, a variety of methods can be employed. One common approach is to use photolithography (see Figure 2.4.A) to create a pattern on the surface of the

wafer. This pattern is then used to etch channels into the wafer using a variety of techniques, such as deep reactive ion etching or wet etching. Once the channels are etched into the wafer, they can be coated with a variety of materials using techniques such as spin coating or physical vapor deposition. Once the channels have been created and coated, they can be used for a variety of microfluidic applications. One such application is the analysis of biological samples, such as blood. By controlling the flow of fluid through the channels, it is possible to isolate and analyze individual cells or molecules within a sample. Other applications include chemical synthesis, drug discovery, and materials science. In order to fabricate the microfluidic channels used in this study, a multi-step process was employed. First, the channel sets were designed using Inkscape or a similar program, and then printed on the top of a silicon wafer using photolithography. After the channels were printed, the wafer was coated with a polymer layer to facilitate the flow of fluids through the channels. This process allowed for the creation of highly precise and controllable microfluidic channels, which were used in the subsequent experiments.

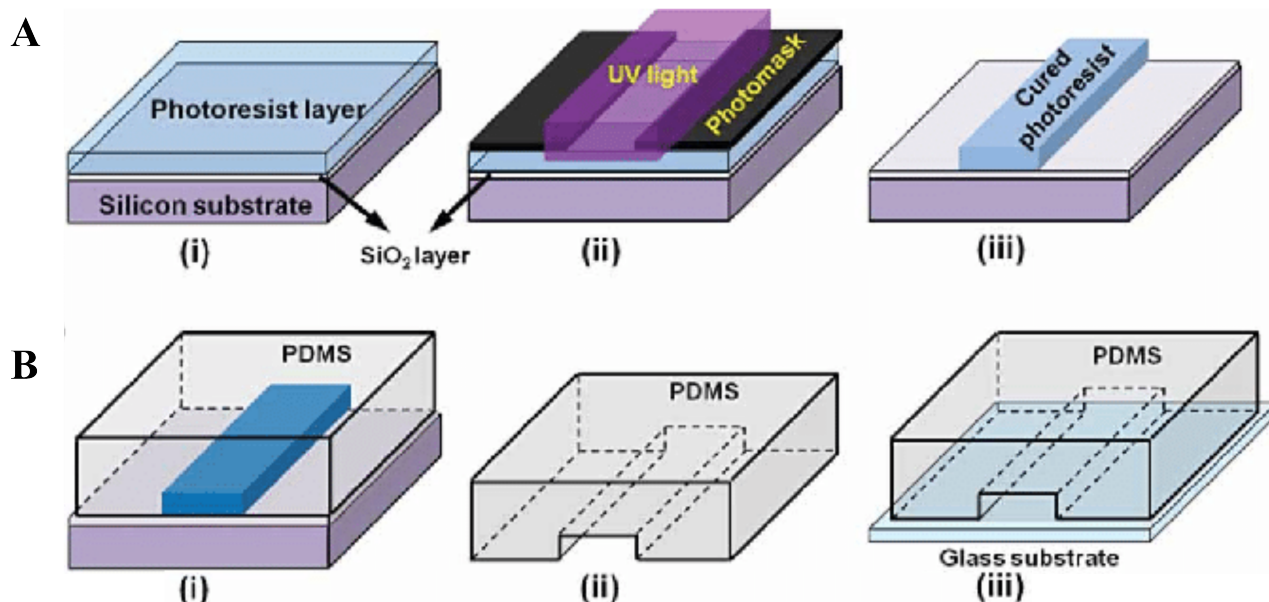


Figure 2.4: The fabrication of microfluidic devices involves a meticulous process combining photolithography and soft lithography, as illustrated in the accompanying figure. A. Photolithography Process: (A.i) Silicon substrate is first prepared with a silicon dioxide (SiO₂) layer, upon which a photoresist layer is applied. (A.ii) The substrate, coated with the photoresist layer, is then aligned with a photomask. Ultraviolet (UV) light is used to expose the photoresist through the photomask, allowing the desired pattern to be transferred. (A.iii) After UV exposure, the photoresist is developed, leaving behind a cured photoresist pattern on the silicon substrate. B. Soft Lithography Process: (B.i) In the initial step, PDMS is poured over the patterned photoresist on the silicon substrate. This setup is then allowed to cure, forming a negative replica of the original pattern. (B.ii) Once the PDMS has cured, it is carefully peeled off from the substrate, revealing a detailed channel structure imprinted within the PDMS. (B.iii) The final step involves bonding the patterned PDMS structure to a glass substrate, creating a completed microfluidic device ready for various applications. *Reprinted with permission from Sengupta et.al*^[151].

Overall, the fabrication of microfluidic channels is a complex process that requires a variety of specialized techniques and equipment. However, the resulting channels provide a highly

precise and controllable environment for the study of a wide range of phenomena, making them an important tool for researchers in a variety of fields. Polydimethylsiloxane (PDMS, RTV 615A/B, Momentive Performance Materials, Waterford, NY) is a widely used material in the field of microfluidics due to its transparency, biocompatibility, and ease of fabrication. PDMS is a type of silicone elastomer that is typically created by mixing a base material with a curing agent in a 10:1 ratio. Once the two materials are mixed together, the resulting mixture can be poured into a mold and allowed to cure for several hours. PDMS can be stored in a cool, dry environment prior to use, and it is typically used within a few weeks of being mixed.

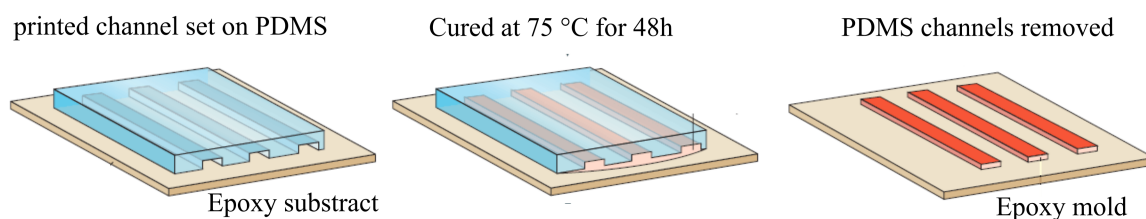


Figure 2.5: The fabrication process of epoxy molds using PDMS channels through a series of well-defined steps: Initially, printed channels are set on a PDMS substrate, which is then placed onto an epoxy substrate. This assembly ensures that the PDMS channels are securely positioned on the epoxy base. The next step involves curing the setup at a temperature of 75 °C for 48 hours. This extended curing period allows the PDMS channels to firmly adhere to the epoxy substrate, ensuring a robust mold formation. After the curing process is complete, the PDMS channels are carefully removed, leaving behind a detailed imprint on the epoxy substrate. This results in the formation of an epoxy mold, accurately capturing the geometry of the original PDMS channels. *Reprinted and modified with permission from Douglas B. Weibel et. al*^[152].

To create PDMS chips, the channels are first fabricated on a silicon wafer. The PDMS is then extracted from the silicon wafer by pouring it over the surface of the wafer and allowing it to cure (see Figure 2.4.B). Once the PDMS has cured, it can be peeled away from the wafer, and an epoxy mold can be created from the PDMS using a mixture of epoxy and hardener. The epoxy mold can then be used to create additional PDMS chips, allowing for the replication of the original channel design. The use of epoxy molds instead of the original silicon wafer is preferred in some cases to avoid damage to the original channel sets (fabrication steps is presented in Figure 2.5). Epoxy molds also offer greater flexibility in terms of the shape and size of the final PDMS chips. However, silicon wafers are typically preferred for the original fabrication of the channels due to their superior resolution and originality.

In summary, the use of PDMS and epoxy molds in microfluidic device fabrication allows for the creation of highly precise and controlled channels that are essential for many microfluidic applications. While the process of fabricating PDMS chips can be complex and time-consuming.

2.2.2 PDMS-based Chip

After extracting the PDMS from the epoxy mold, it may require some treatments to prepare it for bonding with the glass chip. One of the most common treatments is to reshape the PDMS using a scalpel to ensure that it fits properly on the glass chip. The surface of the PDMS may

also need to be cleaned to remove any dust or debris that could interfere with the bonding process. This can be accomplished by gently pressing a piece of tape onto the surface of the PDMS and peeling it away, or by rinsing the surface with distilled water.

The glass chip that will serve as the base for the PDMS channels also requires careful preparation before bonding. This typically involves cleaning the surface of the glass chip with isopropanol and distilled water to remove any debris or fingerprints. The glass chip can be either thick or thin, depending on the specific requirements of the experiment. To bond the PDMS and glass surfaces together, a plasma cleaner can be used to ionize both surfaces. This process creates a chemical bond between the PDMS and glass that is both strong and reliable. Once the bonding process is complete, the PDMS and glass chip can be baked at a low temperature $T = 75^{\circ}\text{C}$ to further strengthen the bond.

2.2.3 Sacles and Geometry

The precise geometry of microfluidic channels is paramount for their functionality, especially in applications involving the manipulation and observation of RBCs. This section delineates the methods and results of our geometric measurements of the microfluidic channels, which are critical for ensuring accurate flow dynamics and experimental reproducibility. To accurately measure the dimensions of the microfluidic channels, we utilized a combination of optical microscopy and image analysis techniques. Initially, the channels were imaged under various conditions to highlight their structural features. The imaging process involved filling the channels with PDMS and subsequently introducing air to enhance the visibility of the channel boundaries. This method provided a clear contrast between the filled and unfilled regions, allowing for precise identification of the channel edges. Subsequent images were taken after the removal of PDMS, revealing the channels' inherent structure without any filling material. This step was crucial for assessing any potential deformation or residue left by the PDMS, ensuring that the channels maintained their intended dimensions and shape. Measurements of the channel width and height were then obtained, providing essential data for understanding the flow characteristics within the channels (see Figure [2.6.A](#)).

Additionally, we performed a top-down analysis of the channels to evaluate the uniformity of their width along different sections. Consistent channel width is vital for ensuring uniform flow conditions, which are necessary for accurate experimental outcomes. Any deviations or irregularities in the channel dimensions could lead to variations in flow dynamics, potentially affecting the behavior of RBCs within the channels (see Figure [2.6.B](#)). The intricate features of the microfluidic channels, such as bends and junctions, were also carefully examined. These features can significantly impact the flow patterns and must be precisely fabricated to ensure predictable and controlled fluid movement. High-resolution imaging techniques enabled us to capture these details, ensuring that even minute aspects of the channel geometry were accurately

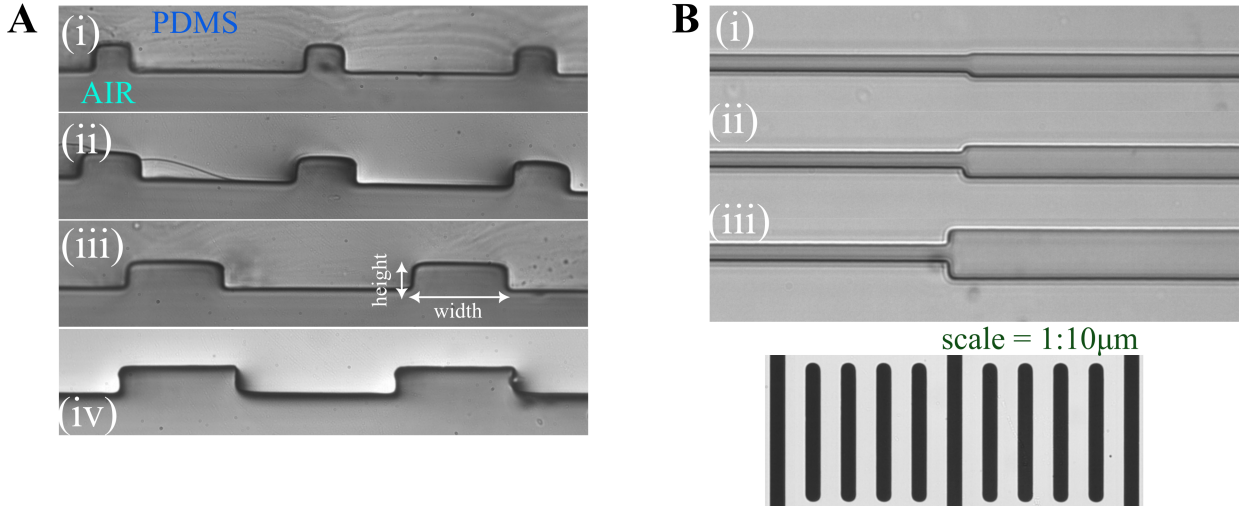


Figure 2.6: Observations on the channel sets used under the microscope using the lense of $\times 60$ magnitude. A. Cross-section (side view) of the channel sets with a height of $8\ \mu\text{m}$, and widths of 10 , 15 , 25 and $35\ \mu\text{m}$ (i-iv consecutively). Both shadowed and lightened sides represents the air and PDMS chip respectively. B. Top view of the channel used for the compression-expansion process, where the channels have the same height $5\ \mu\text{m}$ and same first width $W_c = 8\ \mu\text{m}$ and different second widths $W_e = 10$, 16 and $25\ \mu\text{m}$ (i-iii consecutively). The scale represented at the bottom right is used to measure the dimensions of all the channels.

documented. A scale reference was included in the imaging process to provide a standard for measurement comparison. This reference, with a scale of $1 : 10\ \mu\text{m}$, was essential for translating the observed dimensions into accurate real-world measurements, ensuring that the channels met the required specifications for our experiments.

2.3 Recording and Exporting Raw Images

The experimental setup used for subsequent experiments was designed to capture high-quality images of particles and extract important data from these images. The setup involved the use of specialized software to control various parameters such as frame rate, contrast, and region of interest. Additionally, an inverted microscope with magnifiers was used, which provided the necessary resolution and magnification required for accurate analysis of the particles. A dedicated algorithm program was also developed in Matlab for particle tracking analysis, which allowed for the extraction of important data such as position, center of mass, area, and eccentricity. This algorithm was designed to automatically identify and track the particles of interest, eliminating the need for manual tracking and minimizing human error.

The experimental setup was carefully optimized to ensure consistent and reliable data collection and analysis. Lighting conditions were adjusted, and the software was configured to maintain a consistent frame rate and contrast throughout the experiments. The magnifiers were selected based on the ROI, and were adjusted accordingly to ensure the particles were well-focused and in sharp detail.

2.3.1 Microscope, Cameras and Lenses

The shape of RBCs was assessed using a microfluidic device mounted on an inverted microscope (*Eclipse TE2000-S*, Nikon). The inverted configuration facilitates the observation of live cells that require a stable environment. This microscope (sketched in Figure 2.7.e) is equipped with advanced features such as a digital camera, fluorescence imaging, and an autofocus system, which are essential for high-quality biological imaging. Blue LED illumination (*SOLIS-415C*, Thorlabs Inc. see Figure 2.7.b) emitting a 415 nm wavelength was employed, providing high-intensity, stable, and uniform illumination beneficial for fluorescence microscopy. To image RBC flow at the midpoint of the microfluidic chip (L/2) and analyze RBC shape (see Figure 2.7.c), a high-speed camera (Fastec HiSpec 2G, see Figure 2.7.f) coupled with a $\times 60$ air objective (*Plan Fluor*, Nikon, $NA=1.25$ Figure 2.7.d) was used. This setup enabled accurate real-time capture of RBC shapes, which is crucial for data analysis. Flow stability during experiments was controlled and maintained by a high-precision pressure device (*OB1-MK3*, Elveflow check Figure 2.7.b).

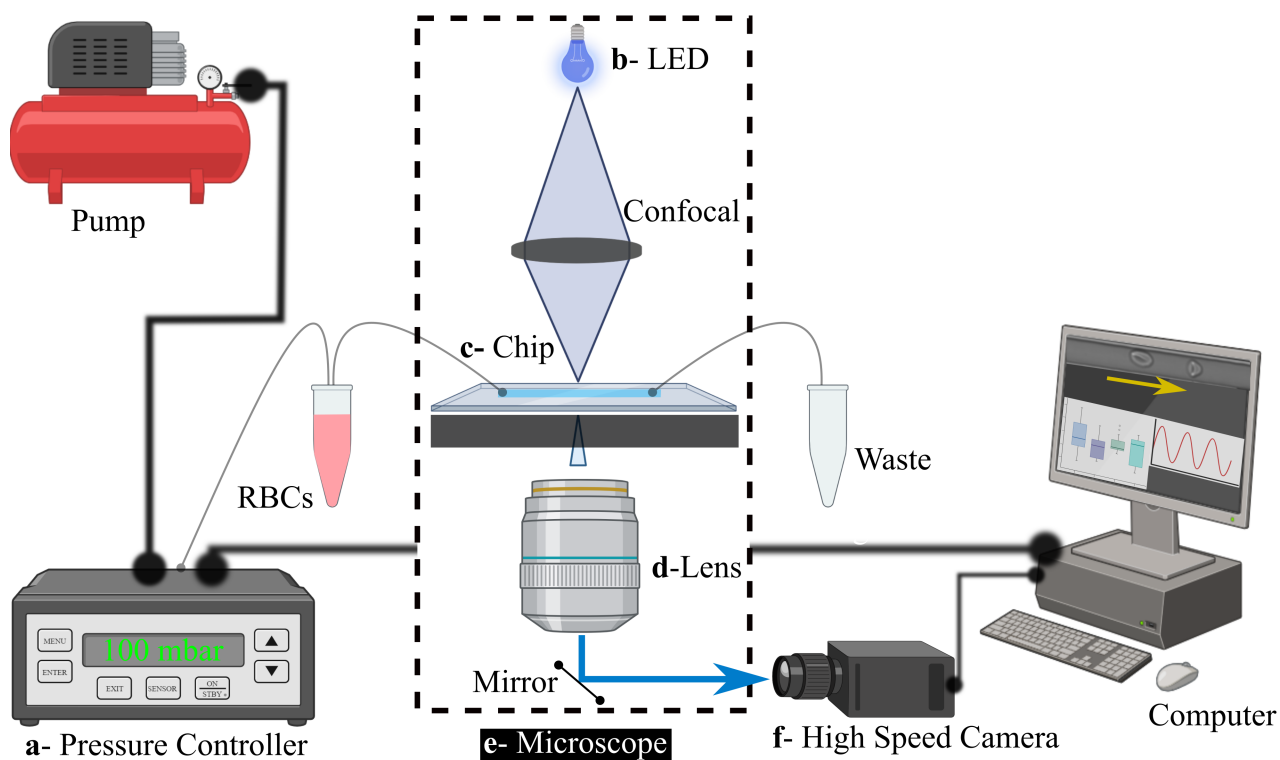


Figure 2.7: Illustration of the main elements of the setup used during all the experiments. Pump feed the microfluidic system with enough air pressure (2000 mbar max), tooled with the controller device of the precise amount of pressure needed. The inverted microscope elements represents inside the dashed area: blue LED at the top as a light source, which manually focused with a confocal. The microfluidic chip layed at the top of a moving stage. The lense capture the light and guiding it with a mirror to the camera for the recording. The computer is the main controller of the system, where the pressure controller, moving stage and frame rate of the camera can be tuned. *Image created using Biorender.*

Additionally, a USB 3.0 camera (*DMK 23U1300*, *The Imaging Source*) with a $\times 20$ air

objective (*Plan Fluor, Nikon, NA=0.45*) was used to provide lower magnification imaging, capturing a wider field of view within the microfluidic device. RAW image sequences were recorded using the Capture program and saved in uncompressed BMP (Bitmap) or AVI (Audio Video Interleave) formats to retain the original image quality for analysis. The combination of advanced microscopy, high-speed imaging, and precision flow control facilitated a reliable assessment of RBC shape within the microfluidic device.

2.3.2 Image Sequences

- **Shape Classification:** To capture the movement of RBCs in microfluidic channels, image series were recorded at frame rates ranging from 50 to 500 frames per second (fps) using a high-speed camera (Fastec HiSpec 1). The specific frame rate within this range was adjusted based on the pressure set by the pressure controller, which in turn determined the mean velocities of the RBCs. This adjustment was crucial to ensure clear images of moving RBCs while minimizing motion blur. The footage was captured in the camera's single mode, which produces a continuous sequence of images. The camera's internal memory, with a capacity of 2 GB, facilitated this high-speed image acquisition independently of the computer's processing power, as it did not require real-time data streaming to the PC. Given the memory constraints, the region of interest (ROI) was cropped to a field of view length of 1280 pixels and a height slightly exceeding the channel width (approximately 100 pixels). While theoretically, it is possible to record multiple channels by expanding the ROI, the considerable space between adjacent channels would reduce the number of cells recorded per sequence. Therefore, the ROI was optimized to maximize the efficiency of cell recording within the available memory limits.
- **Compression-Expansion Process:** To track and record each individual RBC as it appears in the region of interest (ROI), a Matlab program was utilized instead of recording at frame rates ranging from 50 to 500 frames per second. The *IMAGINGSOURCE* monochrome camera USB 3.0 *DMK 23UP1300* was employed for this purpose due to its live recording capacity. The use of *Matlab* tracking cell program, footage was not captured in the camera's single mode. Instead, the USB-camera's full RAM memory was used to store the frames in the form of AVI videos for each cell. The ROI was minimized to a length of 400 pixels and a height of 50 pixels to further optimize the tracking and recording process within the available memory limits.

2.3.3 Single Particle Tracking

Unlike particle imaging velocimetry (PIV), which relies on calculating frame-to-frame correlations to determine the velocity field of tracer particles within a fluid, the approach utilizes single particle tracking (SPT) to analyze recorded image sequences. While this method does

not provide detailed insights into the flow profile within the channel, it allows extraction of the crucial velocity and positional data for each individual cell. This data enables the construction of a phase diagram illustrating cell shapes in relation to cell velocity and axial position within the channel.

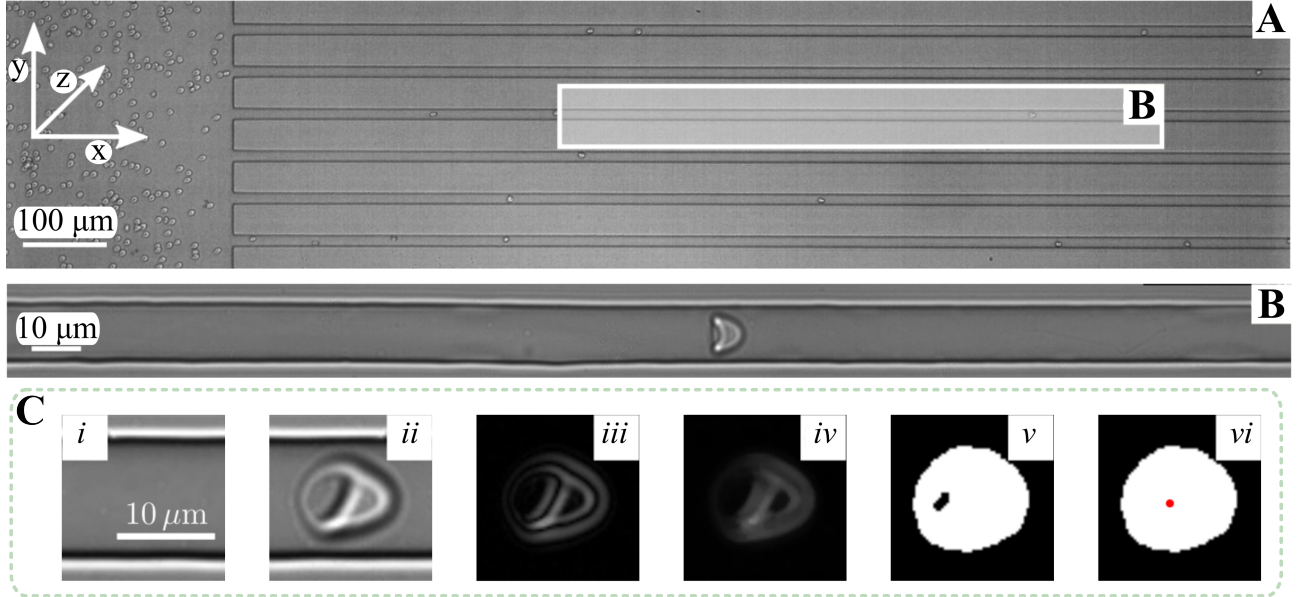


Figure 2.8: Snapshots of the microfluidic channel sets and single RBC flowing through: A. Frame recorded under magnitude of $10\times$ illustrates the reservoir (left) which contains dozens of RBCs entering the channel sets. B. Single RBC flowing through the channel $W = 8\ \mu\text{m}$ and $H = 10\ \mu\text{m}$ under a pressure of $p = 200\ \text{mbar}$. C. Scheme of image post-processing steps for RBCs in microcapillary flow. For better visualization, the widths of the individual images have been cropped to fit one RBC. (i) Background of the cropped channel, obtained by the arithmetic mean of 100 images of one image sequence, cf. Eq. (2.5). (ii) Raw image of a flowing RBC captured at the identical channel position as in (i). (iii) Resulting image after subtracting the background image (i) from (ii), according to Eq. (2.6). (iv) Image after application of a median filter. (v) Binarized image, obtained from gray-value image (iv). (vi) Filling the connected black pixels in (v), we omit any holes in the final cell image. The red dot indicates the position of the center of mass. *Source:* Kihm thesis^[153] used with permission.

The SPT algorithm is a multi-step process, well-documented in scientific literature, but here the focus on the custom modifications made to detect RBCs in the experiments. Initially, the enhance of RBC detection by subtracting the background from the image sequence. This background, B_{ij} , is estimated as the arithmetic mean of a subset of N images, I_{nij} , calculated using the formula:

$$B_{ij} = \frac{1}{N} \sum_{n=1}^N I_{nij}$$

where i and j represent the pixel coordinates. A value of $N = 100$ has proven effective, ensuring that only minimal fluctuations remain in the image after iterative background subtraction. The resulting image, R_{nij} , for the n -th frame is given by:

$$R_{nij} = |I_{nij} - B_{ij}|$$

where the absolute value is taken to highlight deviations from the background. To refine these images, the application of a median filter with a stride of 3×3 pixels is made, which removes artifacts and yields a clearer image. After converting the grayscale image to a binary image (see image process in Figure 2.8.C), the centers of mass of all white pixel clusters, corresponding to the RBCs are identified. Any black pixels within the white cell regions in the binarized images are filled to ensure accuracy. Besides determining the centers of mass, also calculating shape descriptors such as area, orientation, eccentricity and boundary box (where the lateral and horizontal lengths of the cell are identified) of an ellipsoid with identical second moments. Given the optical setup and resolution, the estimation of an uncertainty in detecting the center of mass of $s_p = \pm 0.1 \mu m$ is made. To derive the trajectories from these RBC positions, the minimization of the distances between positions in consecutive images is necessary. This linking protocol is applied across the entire image sequence, yielding trajectories for all recorded cells. Additionally, a filter of the trajectories is made to exclude RBCs that cannot be considered isolated, as close intercellular distances lead to significant hydrodynamic interactions. For RBCs deemed isolated, their images are cropped into sections of 90×90 pixels, ensuring that the entire cell and channel borders are captured. A sophisticated algorithm ensures that the entire cell is within this section, regardless of the exact center of mass position.

CHAPTER I: CONFINEMENT EFFECT ON THE MICROCAPILLARY SINGLE-CELL-FLOW AND SHAPE OF RED BLOOD CELLS

Contents:

3.1	Introduction	39
3.2	Methodology	42
	3.2.1 RBC sample preparation	42
	3.2.2 Microfluidic setup	42
3.3	Results	44
	3.3.1 Phase diagrams of RBC shape	44
	3.3.2 RBC equilibrium position across the channel width	47
	3.3.3 Elongation of croissants and slippers in the microchannels	48
	3.3.4 Unstable other RBC shapes	50
3.4	Conclusion	52

The following chapter is a reformatted reprint of the manuscript published in *Biomicrofluidic*^[132].

Abstract

The ability to change shape is essential for the proper functioning of red blood cells (RBCs) within the microvasculature. The shape of RBCs significantly influences blood flow and has been employed in microfluidic lab-on-a-chip devices, serving as a diagnostic biomarker for specific pathologies and enabling the assessment of RBC deformability. While external flow conditions, such as the vessel size and the flow velocity, are known to impact microscale RBC flow, our comprehensive understanding of how their shape-adapting ability is influenced by channel confinement in biomedical applications remains incomplete. This study explores the impact of various rectangular and square channels, each with different confinement and aspect ratios, on the in vitro RBC flow behavior and characteristic shapes. We demonstrate that rectangular microchannels, with a height similar to the RBC diameter in combination with a confinement ratio exceeding 0.9, are required to generate distinctive well-defined croissant and slipper-like RBC shapes. These shapes are characterized by their equilibrium positions in the channel cross section, and we observe a strong elongation of both stable shapes in response to the shear rate across the different channels. Less confined channel configurations lead to the emergence of unstable other shape types that display rich shape dynamics. Our work establishes an experimental framework to understand the influence of channel size on the single-cell flow behavior of RBCs, providing valuable insights for the design of biomicrofluidic single-cell analysis applications.

Keywords: Red blood cells, microfluidics, channel confinement, cell shape, flow behavior, lab-on-a-chip devices

3.1 Introduction

Red blood cells (RBCs) are the main cellular constituent of blood and are vital in facilitating gas exchange between blood and tissues within the microcirculation. The properties of RBCs, such as their deformability and shape, have a profound impact on blood flow [73]. At rest, human RBCs have a disk-like shape with a diameter of $8\ \mu\text{m}$ and a thickness of $2\ \mu\text{m}$. Due to their high deformability, healthy RBCs can dynamically adapt their shape according to external flow conditions, such as the flow rate, vessel confinement, and the rheological properties of the surrounding fluid [19,154,155]. In the microvascular network where vessel diameters are comparable to RBC size, RBCs flow in a single-file arrangement, and various RBC shapes have been observed [58,156,157]. Consequently, the study of single-cell RBC flow has been conducted experimentally in microfluidic devices [74,76,131,158–162], as well as through numerical simulations [75,81,82,129,163,164], to understand the impact of intrinsic cell properties and external flow conditions on cell shape. Understanding single-cell RBC flow and deformation has contributed to the advancement and development of lab-on-a-chip technologies for RBC deformability analysis of storage lesions in transfusion medicine and for evaluation of biomedical RBC properties in health and disease [11,165,166].

Nevertheless, fundamental knowledge of how external flow conditions such as channel confinement modify the RBC shape in *in vitro* microscale flows is still missing. In microscale single-cell flow, RBCs display a wide variety of stable and dynamic shapes depending on the biophysical cell properties, channel confinement, flow velocity, and the properties of the surrounding medium. Various dynamical states, including snaking, tumbling, swinging, and tank-treading cells, have been reported under steady flow conditions [55,60,73]. Notably, in strongly confined rectangular channels with channel dimensions (height and width) similar to the RBC size, this RBC shape complexity consolidates into two dominant RBC shapes: the croissant and the slipper shape [74,75,78]. The symmetric croissant-like shape predominantly appears at low flow velocities, while the asymmetric slipper shape emerges for higher cell velocities Figure 3.1. Guckenberger et al. [75] investigated these two dominant RBC shapes in a rectangular microfluidic channel with a width of $12\ \mu\text{m}$ and a height of $10\ \mu\text{m}$ through a combination of microfluidic experiments and numerical simulations. They introduced the concept of these so-called RBC shape phase diagram, which shows the fraction of these stable croissant and slipper shapes, as well as a class called “others” (see Figure 3.1) that were not uniquely identifiable, as a function of the cell velocity v . In their rectangular channel, they observed that the croissant shape dominated at cell velocities $v < 5\ \text{mm}\cdot\text{s}^{-1}$, while roughly 70%-80% of the RBCs exhibited a slipper shape above $v > 5\ \text{mm}\cdot\text{s}^{-1}$. They also reported a strong flow shape coupling of the highly deformable RBCs and showed that the cell’s equilibrium position in the cross section and along the channel width is inherently coupled to its shape. Hence, croissant like RBCs preferentially flow at a central position in the channel centerline, whereas slippers flow closer to the channel side walls

(see green marker in Figure 3.1). Furthermore, the authors demonstrated that the emergence of RBC shapes is influenced not only by system parameters, such as flow velocity or channel size, but also by initial conditions, including the initial shape of the RBC and its position within the channel cross section at the onset of the microfluidic channel^[75].

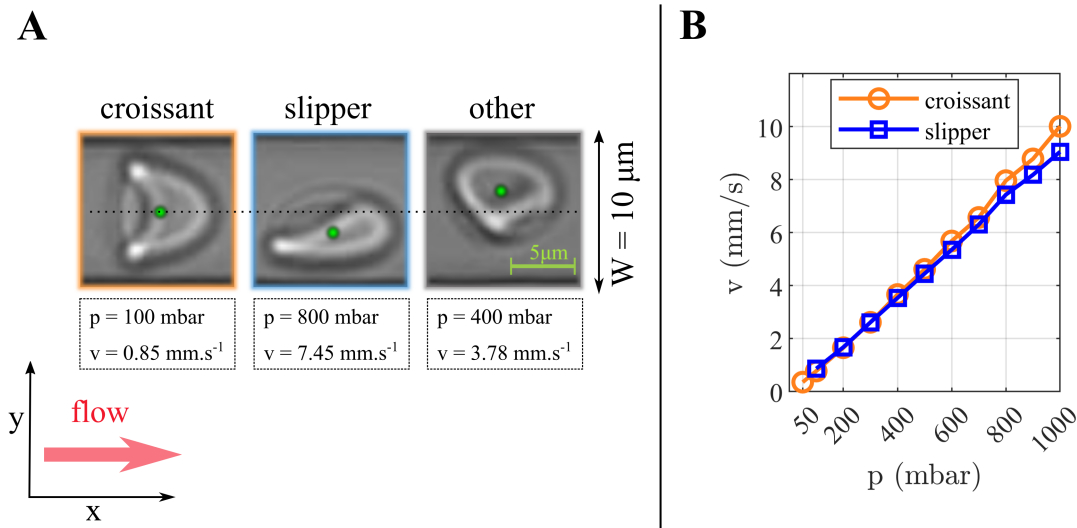


Figure 3.1: Flow behaviour of a RBC in confined fluidic channel ($W = 10 \mu\text{m}$, $H = 8 \mu\text{m}$). (A) Depicts a centrally positioned croissant-like shape, an asymmetric slipper-shaped structure and illustration of a variant shape within the microfluidic channel. The flow direction is indicated from left to right. Dotted black lines represent the channel's midpoint along its width W . Green dots denote the centroid of the cell in y -direction. (Scale bars denote $5 \mu\text{m}$) (B) Velocities of the cell for the two kind of stable shapes as a function of the applied pressure drop follows the Darcy's law^[167].

Recently, as we will see in the chapter, microfluidic investigations have unveiled the sensitivity of the stable croissant and slipper shapes in relation to biophysical cell properties such as RBC age and reduced membrane deformability^[131]. Utilizing RBCs from healthy donors and employing density gradient centrifugation methods, it has been demonstrated that the proportion of stable asymmetric, off-centered slipper-like cells diminishes with increasing age, while aged cells exhibit an augmented prevalence of stable symmetric croissants along the microchannel centerline. Consequently, analysis of the RBC shape phase diagram facilitates the discrimination of distinct RBC sub-populations, notably revealing variations in cell age. Expanding upon the shape phase diagram proposed by Guckenberger et al.^[75], additional RBC shapes in microcapillary flow, such as sphero-echinocytes, acanthocytes, and complementary pathological croissant and slipper shapes, have been introduced under pathological conditions to complement the phase diagram^[77,79]. Integrating the analysis of the cell's equilibrium position, these cell shape classification approaches have been recently applied to assess changes in the microcapillary flow behavior of neuroacanthocytosis syndrome and COVID-19 patients and patients undergoing dialysis^[77-80], demonstrating its potential as a biomarker and functional diagnostic tool for specific pathologies and to evaluate the quality of stored blood. In addition to experiments conducted in rectangular microchannels, numerical simulations revealed a

diverse range of steady and dynamic RBC shapes in round microcapillaries. Fedosov et al.^[81] constructed a comprehensive shape phase diagram encompassing stationery parachutes, swinging slippers, tumbling, and snaking discocytes as a function of the channel confinement and the shear rate in the system with a circular cross section. Note that parachute-shaped RBCs, which tend to become more asymmetric in rectangular channels, are often referred to as croissants in microfluidic experiments with square or rectangular microchannels. Similar to experimental observations^[75], parachute-like RBCs in the round capillaries flow in the tube center, while slippers are displaced further from the channel center^[81]. The conditions of occurrence of these shapes and the transition between the dynamic shapes critically depend on the RBC properties and the viscosity contrast between RBC cytosol and blood plasma^[82]. While experimental and numerical progress has advanced our understanding of how intrinsic cell properties, such as their deformability, cytosol viscosity, viscoelasticity of the membrane, and age, affect the RBC shape and microscale flow behavior^[85,131], detailed experimental investigations of how slight changes in the channel confinement affect the RBC capillary flow and the shape phase diagram remain scarce. Presently, poly(dimethylsiloxane)(PDMS) microchannels fabricated using soft lithography techniques serve as a common platform to investigate the microscale flow of biological systems^[83,84]. These techniques generally offer highly reproducible results down to the nanoscale, with low shrinkage during cure^[168]. However, inconsistencies in PDMS casting, curing, releasing, or bonding can introduce variations in the channel dimensions between different molds or chips during fabrication. Additionally, changes in the channel cross section may occur due to the deformation of flexible PDMS microchannels under pressure-driven flow^[169–173]. Therefore, understanding the effect of channel confinement on the different RBC shapes, employed for in vitro microvascular flow assessment, is paramount. This becomes particularly crucial in the context of assessing microscale flow under physiologically relevant conditions, where subtle variations in channel confinement can significantly influence the observed RBC shapes and, consequently, the accuracy of the RBC shape phase diagram. In this study, we examine the single-cell flow of RBCs through six distinct microfluidic channels. Specifically, we explore the effect of how small differences in the order of a few micrometers affect the RBC phase diagram, the cell's equilibrium positions, their elongation, and the occurrence of unstable cell shapes. Our study aims to conduct a comprehensive experimental investigation to explore the sensitivity of these approaches, particularly how the RBC shape phase diagrams (PDs) are influenced by the precise channel dimensions. This understanding is crucial for elucidating RBC flow dynamics in more intricate systems, such as those found in pathological conditions. For this, we use high-speed imaging of microscale RBC flow and systematically vary the channel width and height, resulting in different aspect ratios and confinement ratios of the channel cross section. Our findings highlight that the presence of stable slipper-like shapes requires a non-square rectangular cross section, while croissant-like cells also disappear

gradually in square channels. Intriguingly, both stable croissant and slipper shapes disappear when the channel dimensions exceed $10\ \mu\text{m}$, leading to the emergence of highly dynamical other RBC shapes. Additionally, we show how the elongation of croissants and slippers, quantified by the elongation index EI, scales with the shear rate in the microchannels, highly relevant for biomicrofluidic technologies aimed at measuring RBC deformability^[166].

3.2 Methodology

3.2.1 RBC sample preparation

Blood was collected with informed consent from three healthy voluntary donors (age 28–51 years) through needle prick and it was subsequently suspended in phosphate-buffered saline solution (Gibco PBS, Fisher Scientific, Schwerte, Germany). Following collection, samples were centrifuged for 5 min at $3000\times g$. The sedimented RBCs were washed three times with PBS and final RBC samples were adjusted at a hematocrit concentration of 1%Ht in a PBS solution that contained 1 g/l bovine serum albumin (BSA, Sigma-Aldrich, Taufkirchen, Germany) (as described in Figure 2.1). The PBS/BSA mixture is a Newtonian fluid with a shear viscosity of roughly $\eta = 1.2\ \text{mPa}\cdot\text{s}$ ^[76,173]. Blood withdrawal, sample preparation, and microfluidic experiments were performed according to the guidelines of the Declaration of Helsinki and approved by the ethics committee of the “Ärztchamber des Saarlandes” (permission number 51/18).

3.2.2 Microfluidic setup

RBC suspensions were pumped through six distinct microfluidic chips using a high-precision pressure device (OB1-MK3, Elveflow, Paris, France) to apply constant pressure drops ranging between $p = 50\text{--}1000\ \text{mbar}$. The microfluidic chips were designed with microchannel having widths of either $W \approx 10\ \mu\text{m}$ or $W \approx 15\ \mu\text{m}$ in combination with three different heights $H \approx 8; 10$ and $15\ \mu\text{m}$ (Table 3.3 and Figure 3.2). The length of all microfluidic channels is $L = 40\ \text{mm}$.

Table 3.3: Comparison of channel geometries: An overview of the diverse channel geometries obtained from the silicon-based wafer on which these channels were fabricated. It is noteworthy that all channels maintain a uniform total length of $L = 40\ \text{mm}$, ensuring standardization across the experimental setup.

Channel	Width (μm)	Height (μm)	Aspect ratio A/R	Confinement ratio χ
1A	10.49 ± 0.36	7.82 ± 0.29	1.4	0.89
2A	10.64 ± 0.30	10.57 ± 0.18	1.01	0.75
3A	10.39 ± 0.62	15.04 ± 0.33	0.73	0.65
1B	15.25 ± 0.32	7.78 ± 0.11	1.96	0.78
2B	15.67 ± 0.32	10.83 ± 0.18	1.45	0.62
3B	15.83 ± 0.71	15.18 ± 0.25	1.04	0.52

Channel dimensions were determined by a customized MATLAB algorithm [9.14.0.2206163 (R2023a), The MathWorks, Natick, MA] that detects the channel borders based on microscopic

images obtained using brightfield microscopy. Channel dimension data were averaged from different microfluidic chips as well as different positions along the channel flow direction within a chip. We define the channel aspect ratio $AR = W/H$ and the confinement ratio $\chi = D_{RBC}/D_h$ with the diameter of a discocyte-shaped RBC at rest $D_{RBC} = 8 \mu\text{m}$ and the hydraulic diameter of the rectangular channel $D_h = 2WH/(W + H)$.

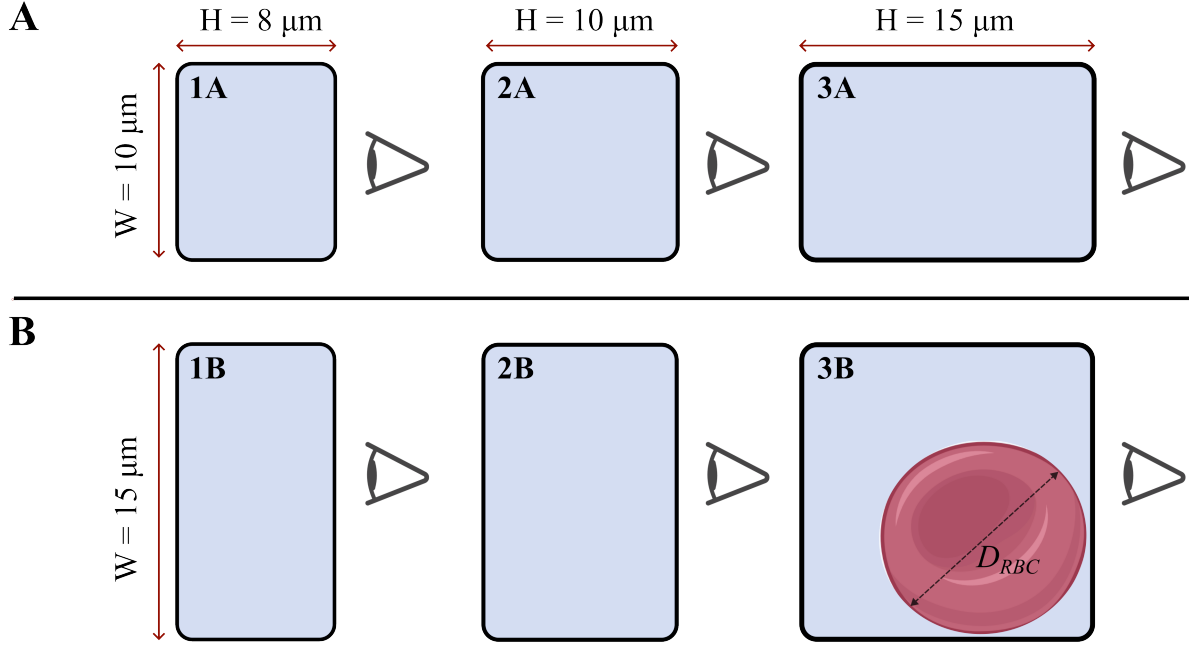


Figure 3.2: Schematic representation elucidating the design of microfluidic channels employed in the experimental setup. The channels exhibit distinct widths, with (A) measuring $10 \mu\text{m}$ and (B) $15 \mu\text{m}$, while also featuring diverse channel heights to investigate their impact on fluid dynamics and cell behavior. The utilization of varied channel dimensions allows for a comprehensive exploration of flow characteristics and cellular responses within confined environments. Notably, the placed eyes to show the points of optical access crucial for observation and analysis within the microfluidic apparatus. Furthermore, a red circle is strategically positioned to illustrate the comparative size of an unaltered discocyte-shaped RBC at rest, showcasing its $8 \mu\text{m}$ diameter relative to the channels under scrutiny. This comprehensive schematic serves as a visual guide, aiding in the understanding of the experimental framework and facilitating interpretation of subsequent results.

The microfluidic chip fabrication followed standard soft lithography techniques using polydimethylsiloxane (PDMS, RTV 615A/B, Momentive Performance Materials, Waterford, NY, USA)^[168]. Subsequently, the chip was bonded to a glass slide using a plasma cleaner (PDC-32G, Harrick Plasma, Ithaca, NY, USA). The inlet and the outlet of the microfluidic chips were connected with rigid medical-grade polyethylene tubing (0.86 mm inner diameter, Scientific Commodities, Lake Havasu City, AZ, USA) to the sample and waste containers, respectively. The microfluidic device was mounted on an inverted microscope (Eclipse TE2000-S, Nikon, Melville, NY, USA), featuring red LED illumination (SOLIS-415C, Thorlabs Inc., Newton, NJ, USA), a $60\times$ air objective (Plan Fluor, Nikon, Melville, NY, USA) with a numerical aperture $NA = 1.25$. RBC flow was recorded at $L_{\text{rec}} = 30 \text{ mm}$ away from the inlet using a high-speed camera (Fastec HiSpec 2G, FASTEC Imaging, San Diego, CA, USA). All microfluidic exper-

iments were performed at 22°C. Image sequences were post-processed using a customized MATLAB algorithm. For each single RBC, we determined the center of mass of each cell in the projection plane (see Figure 3.1), length a in the flow direction, and diameter b along the channel width by identifying a bounding box around the RBC shape. The cell's elongation index is calculated as $DI = (a - b)/(a + b)$. To determine individual cell velocities, we tracked the cell position throughout the image sequence within the field of view. A frame rate of up to 400 frames per second was used to record image sequences of RBC passing the field of view. RBC shapes in flow were classified manually following the criteria established by Guckenberger et al.^[75] Since we did not observe inter-individual variations in the results, data were averaged between the three healthy donors. Data analysis was performed on an average of 6714 cells per donor (between 2653 and 10635 cells).

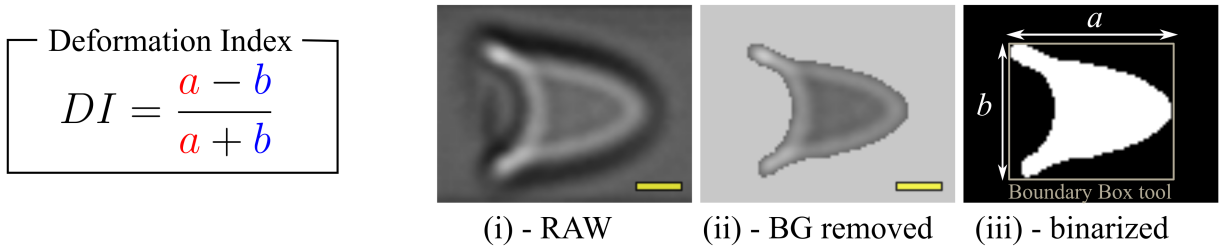


Figure 3.3: Visualization of cell elongation index in a microfluidic channel: Elongation index formula, where a and b are main terms obtained from the *BoundaryBox* tool of the *regionprops* function in Matlab. Measurement Process: From the raw image (i) captured during the experiment, noise and background (BG) are removed to obtain a clean image (ii). Binarization of the image (iii) facilitates the measurement of terms a and b for the cell. (yellow bar scales 2 μm)

3.3 Results

3.3.1 Phase diagrams of RBC shape

Our investigation centers on exploring the impact of channel confinement on the RBC shape in microchannels, focusing on the three dominant RBC shape classes, namely, croissants, slippers, and others, similar to the previously established phase diagram RBC shapes^[74,75,78,79]. Based on the applied pressure drop and the channel cross section, the resulting cell velocities in the microchannels are in the range of $v = 0.2 - 35 \text{ mm.s}^{-1}$ (presented in Figure 3.4), with the lower range being similar to the physiological flow velocities in the microvascular network^[19,155]. Additionally, we calculated the nondimensional capillary number,

$$Ca = \frac{\eta \dot{\gamma} a}{G_s} \quad (3.1)$$

where $\eta = 1.2 \text{ mPa.s}$ is the shear viscosity of the surrounding fluid^[76,173], $\dot{\gamma} = 6v/D_h$ the wall shear rate in the channel^[174], $a = D_{RBC}/2$ the discoid radius of the RBC, and G_s the membrane

shear elastic modulus^[175]. We use $G_s = 4 \mu\text{N}/\text{m}$, in agreement with previous studies^[176,177]. In the investigated cell velocity regime, we find $Ca = 0.28 - 17$ (see top x axes in Figure 3.4). In the RBC shape phase diagrams, we observe a prominent proportion of stable croissant and slipper-shaped RBCs for the smallest channel cross section (Figure 3.4.A) consistent with studies of RBC flow in similarly confined channels^[74,75]. The croissant fraction reaches a peak value of roughly 50% at a velocity of $v = 1 \text{ mm}\cdot\text{s}^{-1}$. As the cell velocity increases, the fraction of croissant-shaped RBC continuously decreases. Simultaneously, the amount of slipper-shaped RBCs increases above $v > 3 \text{ mm}\cdot\text{s}^{-1}$, eventually reaching a plateau value at 70%-75% above $5 \text{ mm}\cdot\text{s}^{-1}$. Keeping the channel width fixed and increasing the channel height to $H = 10 \mu\text{m}$ results in a higher fraction of croissants while slipper-shaped RBCs disappear (Figure 3.4.B). However, with a further increase of the channel height to $H = 15 \mu\text{m}$, the croissant fraction decreases again, and most RBCs display other shape types (Figure 3.4.C). In the channels with a larger width of $W = 15 \mu\text{m}$ and a height of $H = 8 \mu\text{m}$, RBC also exhibit both croissant and slipper-shaped RBCs (Figure 3.4.D) and a qualitatively similar phase diagram than for the smallest channel cross section (compare Figure 3.4.A). However, the fraction of both stable shapes notably reduces in the wider channel. The prominent croissant peak reaches merely 20% at $v = 1 \text{ mm}\cdot\text{s}^{-1}$, while the slipper plateau saturates at 30%-40% above $5 \text{ mm}\cdot\text{s}^{-1}$.

Increasing the channel height results in a successive suppression of slipper-like cells (Figure 3.4.E). At $W = 15 \mu\text{m}$ and $H = 15 \mu\text{m}$, the occurrence of slipper-like RBCs is ultimately suppressed completely, whereas most cells exhibit other shapes at all investigated velocities with a few croissant-like RBC remaining (Figure 3.4.F). Taken together, our observations emphasize that an oblong rectangular cross section coupled with a shallow channel ($H = 10 \mu\text{m}$) is a prerequisite for the emergence of slippers (see Figure 3.4.A and Figure 3.4.D). Modestly increasing the channel height by $2 \mu\text{m}$ to $H = 10 \mu\text{m}$ results in a significant reduction of slipper fraction (see Figure 3.4.E). Consequently, stable slipper-like shapes are primarily found in strongly confined, rectangular channels with a height smaller than $10 \mu\text{m}$ and a confinement ratio exceeding $\chi = 0.9$. It is noteworthy that these slippers are categorically different than the tank-treading slipper-shaped RBCs reported in numerical simulation within round capillaries^[81,82]. In the context of round capillaries, slippers are essentially absent at $\chi > 0.7$ due to the cylindrical channel geometry and mainly appear at low confinement ratios compared to their parachute-like counterpart. In square channels, we do not observe slipper-shaped cells (see Figure 3.4.B and Figure 3.4.F), but an increase in symmetric croissant like RBCs when the channel dimensions do not exceed $10 \mu\text{m}$, corresponding to a confinement ratio of $\chi = 0.75$ (see Figure 3.4.B). At $\chi = 0.52$ (see Figure 3.4.F), the fraction of croissants is drastically reduced, which is similar to observations in numerical simulations, which showed that a transition between stationary parachutes and other dynamical shapes occurs at $\chi \approx 0.5 - 0.55$ in square microchannels^[164]. Note that our microfluidic experiments are restricted to optically accessing

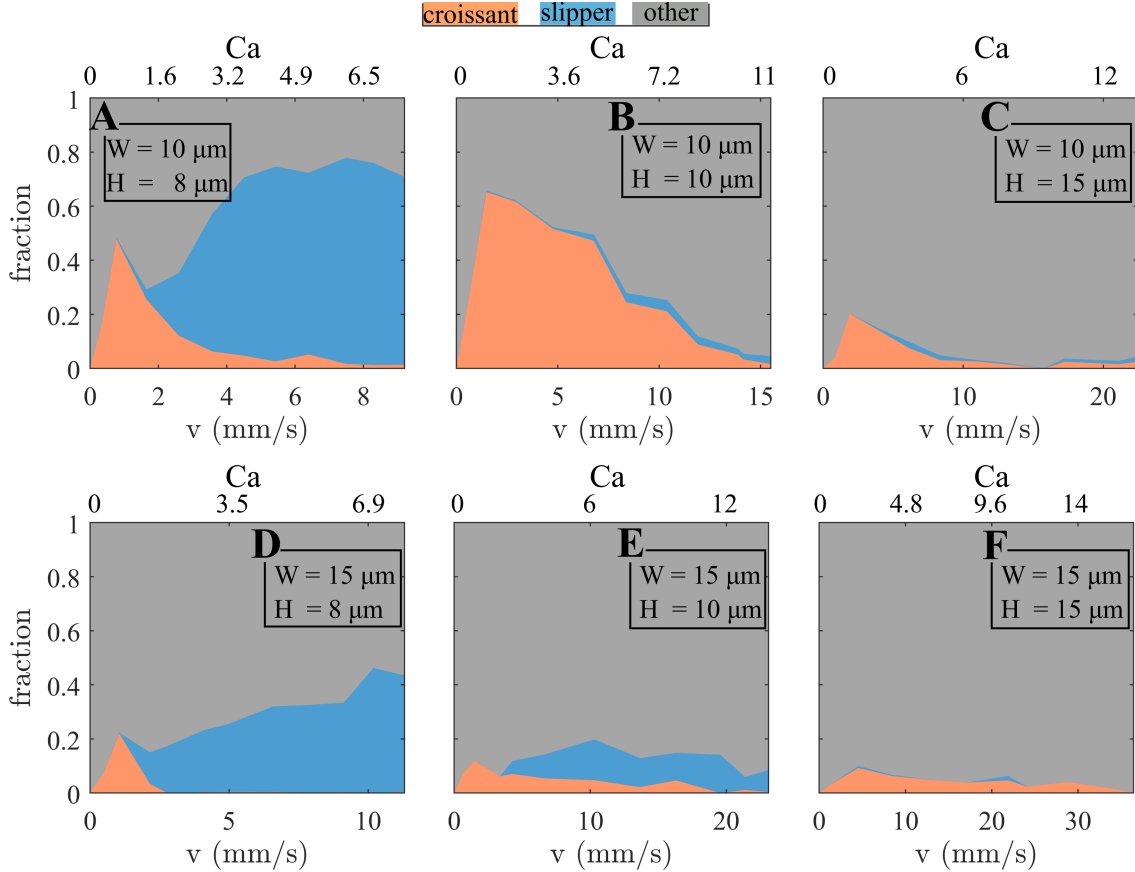


Figure 3.4: Shape phase diagrams (PDs) delineating the morphological transitions of RBC within microfluidic channels, which portray the distribution of croissant-like, slipper-like, and other RBC shapes relative to variations in cell velocity (bottom x axes) and capillary number Ca (top x axes) in the different microfluidic channels. The analysis, conducted meticulously, encompasses an average evaluation of 6714 cells per donor, spanning a range from 2653 to 10635 cells.

RBC flow through one channel side (see blue arrows in Figure 3.2). As a result, cells will be classified based on their projection in the optical x-y-plane in the channel (see Figure 3.2). Therefore, despite having two channels with the same dimensions swapped by 90° (Figure 3.4.C and Figure 3.4.E), we observe different shape phase diagrams. For instance, slippers detected in the channel with $W = 15 \mu\text{m}$ and $H = 10 \mu\text{m}$ flow at off-centered position along channel width W in y-direction in the x-y-plane. In the channel with $W = 10 \mu\text{m}$ and $H = 15 \mu\text{m}$, these cells would flow at offcentered positions along the channel height H in z-direction and their projections on the x-y-observation plane do not exhibit the characteristic slipper shape. Thus, such cells would be classified as others, similar to the so-called sheared croissant class, observed in previous studies^[74]. This effect emphasizes the importance of selecting not only the appropriate channel dimensions in terms of channel height and width but also their relative aspect ratio with respect to the optical access of the channel. We did not use channels with dimensions smaller than $8 \mu\text{m}$ in this study because decreasing the channel size further results in the formation of tightly squeezed, symmetric bullet-like shapes that do not transition into

other asymmetric or off-centered slipper-like shapes, as demonstrated for microcapillaries with diameter $4.7 - 6.6 \mu\text{m}$ corresponding to $\chi = 1.7 - 1.2$ ^[158,159].

3.3.2 RBC equilibrium position across the channel width

The RBC shape is intrinsically linked to its equilibrium position in the microchannel. Based on the 2D projection of the cells in flow and the optical axes of the used setup (see placed eyes in Figure 3.2), we evaluate the RBC equilibrium y -position along the channel width W . It is assessed using the probability density distributions (pdf) of the absolute value of the normalized y -coordinate $|y/W|$ as a function of the velocity (Figure 3.5). For the smallest channel cross section with $W = 10 \mu\text{m}$ and $H = 8 \mu\text{m}$ (see Figure 3.5.A), symmetric croissants flow at a centered position $|y/W| \approx 0$ at low velocities. Increasing the cell velocity results in a reduction of the peak at the central position and an off-centered peak emerges at $|y/W| \approx 0.22$. For the square channel ($W = H = 10 \mu\text{m}$, Figure 3.5.B), most cells also flow along the channel central axis $|y/W| \approx 0$ even at high velocities exceeding $10 \mu\text{m}$.

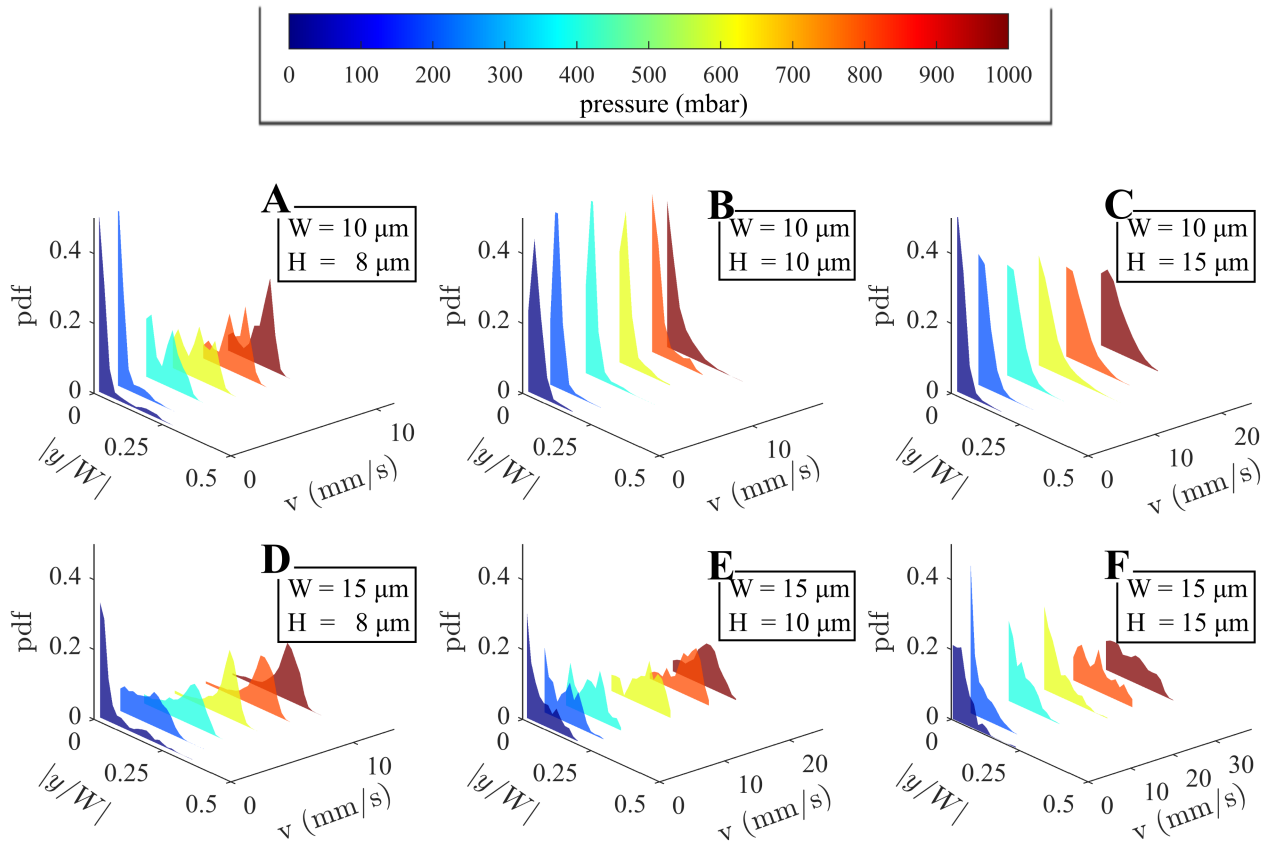


Figure 3.5: Studying cell distribution: The figure illustrates the probability density distributions (PDFs) of RBC y -positions, normalized by the channel width ($|y/W|$) following velocity, to understand the equilibrium positions of these cells across different channel widths (A-C) $W = 10 \mu\text{m}$ and (D-F) $W = 15 \mu\text{m}$. The color bar located at the top provides essential context by indicating the range of applied pressure drop.

This pronounced centered peak in the pdfs persists when keeping the channel width fixed

and increasing the height further to $H = 10 \mu\text{m}$, yet the pdf broadens to more off-centered cell positions at the same time (Figure 3.5.C). In the rectangular channel with $W = 15 \mu\text{m}$ and $H = 8 \mu\text{m}$ (Figure 3.5.D), most cells flow at a central position $|y/W| \approx 0$ at low velocities. At velocities above $5 \text{ mm}\cdot\text{s}^{-1}$, the pdfs exhibit only an offcentered peak at $|y/W| \approx 0.22$. Increasing the height to $H = 10 \mu\text{m}$ (Figure 3.5.E) results in the occurrence of two pronounced peaks in the distributions at $v > 8 \text{ mm}\cdot\text{s}^{-1}$, with one at the centerline and an off-centered one. Upon further increase of the channel height to $15 \mu\text{m}$ (Figure 3.5.F), we still observe a central peak at low velocities up to $v = 20 \text{ mm}\cdot\text{s}^{-1}$. However, RBCs do not flow at a preferred position across the channel width at higher velocities, as indicated by the broad distribution at $v > 25 \text{ mm}\cdot\text{s}^{-1}$. Our analysis of the cell's y-position distribution aligns with the observed phase diagrams. When a significant number of slipper-shaped RBCs is observed (Figure 3.4.A, .D and .E), a pronounced off-centered peak at $|y/W| \approx 0.22$ appears in the pdfs (Figure 3.5.A, .D and .E). This observation is in good agreement with the previous work^[131]. Interestingly, while we find only one offcentered peak at $v > 5 \text{ mm}\cdot\text{s}^{-1}$ in the channel with $W = 15 \mu\text{m}$ and $H = 8 \mu\text{m}$ (Figure 3.5.D), two peaks at $|y/W| \approx 0$ and $|y/W| \approx 0.22$ appear for the slightly deeper channel with $W = 15 \mu\text{m}$ and $H = 10 \mu\text{m}$ (Figure 3.5.E). Such pdfs with two pronounced peaks at elevated velocities have been reported before^[79,131] and are also found in the most confined channel (Figure 3.5.A) due to the emergence of both off-centered slippers and central flowing croissants and other shapes. Note that both channels (Figure 3.5.A and Figure 3.5.E) have similar channel aspect ratios $\text{AR} \approx 1.4$ (see Table I). However, the singularly peaked distribution in the channel with $W = 15 \mu\text{m}$ and $H = 8 \mu\text{m}$ (Figure 3.5.D) at $v > 25 \text{ mm}\cdot\text{s}^{-1}$ suggests that the significant fraction of other-shaped cells (Figure 3.4.D) also flow at an off-centered position, similar to the concurrently appearing slippers. These results highlight that both the RBC shape and the cell's position in the channel cross section provide valuable information for evaluating RBC flow properties relevant to multiple clinical applications^[78].

3.3.3 Elongation of croissants and slippers in the microchannels

In micro-confined conditions, the RBC shape critically depends on the flow rate in the channel^[161,178]. Here, we study how the shape of stable croissant and slipper-like RBCs is affected by the flow conditions in the different microchannels (Figure 3.6.A). To characterize this effect, we assess the cell's elongation index EI as a function of the shear rate in the channel. At low shear rates, croissant-shaped RBCs exhibit a broad shape with a shorter length in flow direction than across the channel width, hence, $\text{EI} < 0$ (Figure 3.6.B). As the shear rate increases up to $\dot{\gamma} = 5 \times 10^3 \text{ s}^{-1}$, there is a substantial rise of the elongation index, independent of the channel cross section. Concurrently, the increase in cell length in the flow direction leads to a transition to positive elongation indices at $\dot{\gamma} = 5 \times 10^3 \text{ s}^{-1}$. Beyond $8 \times 10^3 \text{ s}^{-1}$, cell elongation seems to saturate, eventually reaching a plateau at $\text{EI} = 0.1$. For slipper-like RBCs,

we also observed a gradual increase in the elongation index with the channel shear rate (Figure 3.6.B). However, due to the initially elongated slipper shape, EI is always positive. Between 5×10^3 and $3 \times 10^3 \text{ s}^{-1}$, slipper-like cells exhibit an increase in EI, followed by a saturation at $\text{EI} = 0.3 - 0.4$ beyond $5 \times 10^3 \text{ s}^{-1}$.

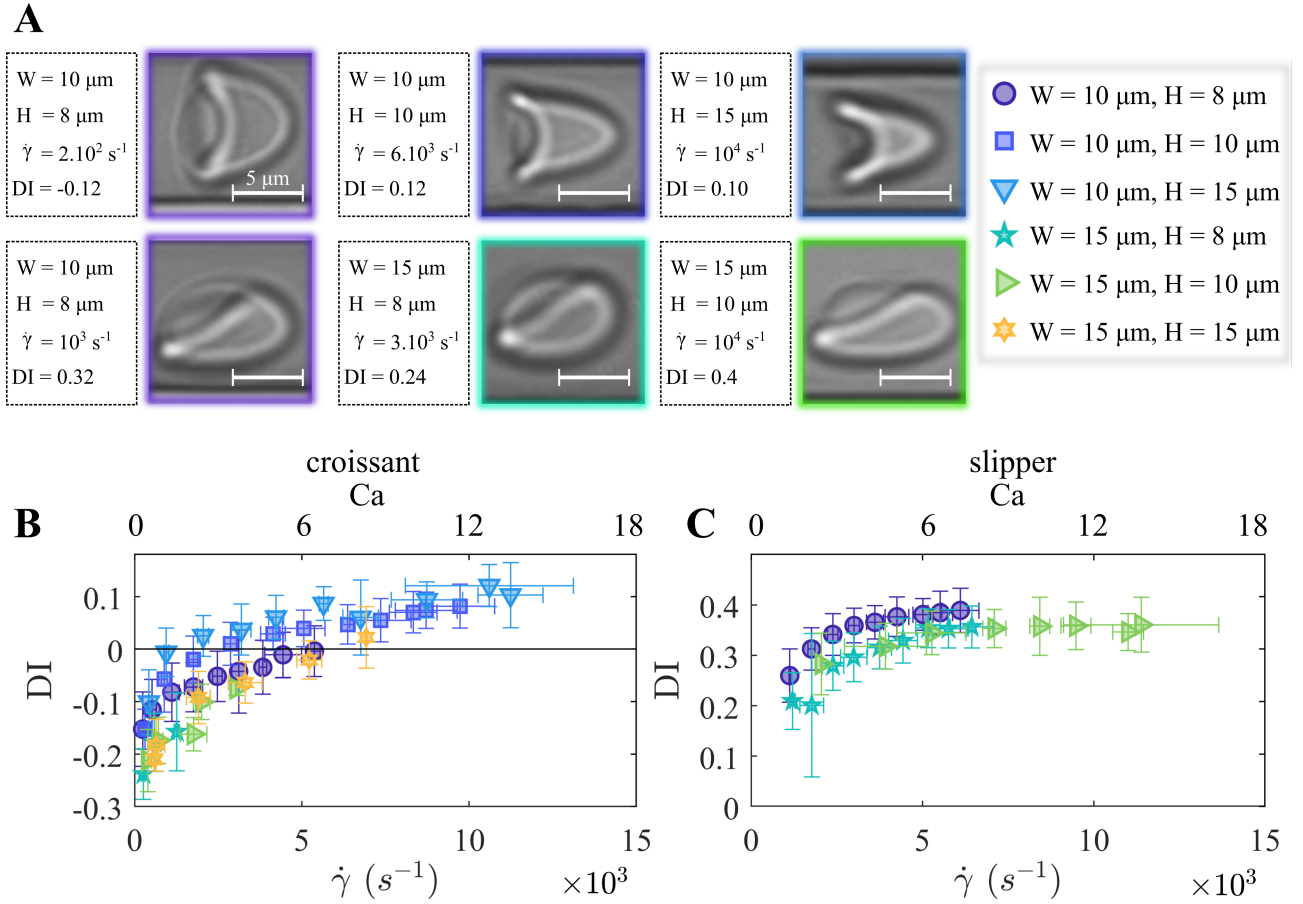


Figure 3.6: Elongation of stable croissant-like and slipper-like RBC shapes in the different channels. (A) Representative images of croissants and slippers in different channels and at various shear rates $\dot{\gamma}$. (Scale bars, $5 \mu\text{m}$). (B) and (C) Elongation index $DI = (a - b)/(a + b)$ in the different microfluidic channels for croissant-like and slipper-like RBCs, respectively. Data are shown as a function of the shear rate (bottom x axes) and capillary number Ca (top x axes). The length a of the RBC in the flow direction and the diameter b along the channel width are identified with a bounding box around the RBC shape, schematically shown in the top right image in (A). Error bars correspond to averaging DI data of cells at the same applied pressure drop.

Assessing the elongation and stretching of RBCs by the fluid shear stress in microcapillaries has emerged as an important technology measuring RBC deformability^[11,166]. Previous work revealed differences in the dynamic deformation behavior between control RBCs and artificially stiffened RBCs, as well as RBCs of diabetes patients in microcapillary flow^[131,138,179]. In our study, the observed increase of cell elongation for stable croissants is in good agreement with previous investigations on single RBCs^[161,180]. This is attributed to the two “tails” of the croissant-shaped RBC that seem to become longer and pointed (see the top row in Figure 3.6.A) as the velocity and shear stress increase. While the cell elongation of croissants does not seem to

saturate completely even at high shear rates (Figure 3.6.B), EI of slipper-shaped RBCs clearly plateaus above $\dot{\gamma} = 5 \times 10^3 \text{ s}^{-1}$, similar to the previously reported high-velocity limit of cell elongation in confined microcapillaries^[159]. Future work will be required to evaluate how the observed dynamic deformation behavior of both stable RBC configurations is connected with the intrinsic cell properties, such as cytosol viscosity and membrane elasticity.

3.3.4 Unstable other RBC shapes

In our experimental investigations, we primarily focus on stable RBC shapes in microcapillary flow. In an effort to explain the suppression of these stable shapes and the occurrence of other shapes (see Figure 3.4), we assess temporal shape changes of the RBC shape within the region of interest with a length of roughly 300 μm in the middle of the microfluidic chip under steady flow conditions. We consider an RBC to have an unstable shape when it rotates, tumbles, or shows any other dynamic shape transitions that lead to fluctuations $\Delta y = y(t) - \bar{y}$ of the cell's temporal y-position $y(t)$ from its mean y-position \bar{y} larger than 5% during passage within the region of interest (Figure 3.7.B).

Croissant and slipper-shaped RBCs exhibit stable shape configurations that do not change significantly while passing the microfluidic channel (two top rows in Figure 3.7.A). For the other cell shape, we find a stable category (third row in Figure 3.7.A), as well as an unstable category that exhibits rich temporal dynamics (bottom row in Figure 3.7.A). While the cell position along the channel width of the three stable shape classes does not change significantly during flow, we observe strong fluctuations of the cell's center of mass position for the category of unstable other cell shapes (representatively shown in Figure 3.7.B). The fraction of unstable other shapes is larger in the microfluidic channels with a large crosssection, i.e., 10×15 , 15×10 , and $15 \times 15 \mu\text{m}^2$ (Figure 3.7.C). Although our experimental field of view only covers approximately 300 μm along the channel flow direction, recent cell-tracking measurements demonstrated that the croissant and slipper shapes are indeed stable^[76]. Once the cell achieves its shape after entering the microfluidic channel, it does not change under steady flow conditions. In our study, we examine the single RBC flow in the middle of the microfluidic chip at $3L/4 = 30 \text{ mm}$. At this position, cells already reached their equilibrium y-position and final shape, and transient effects induced by the fluid inlet can be neglected^[181]. Note that the length over which tank-treading slipper-shaped RBCs in such confined channels oscillate and periodically change their y-position is usually much longer than the region of interest used in this study^[76]. Hence, tank-treading slippers are classified as a stable RBC configuration. In contrast, the dynamic behavior of unsteady other cell shapes does not allow the RBC to reach a steady y-position (see representatively Figure 3.7). These cells predominantly appear in less confined channels with $\chi \leq 0.65$ (see Figure 3.7.C; 10×15 , 15×10 , and $15 \times 15 \mu\text{m}^2$), which is in good agreement with numerical simulations that predict a transition from steady to dynamic shapes upon increasing

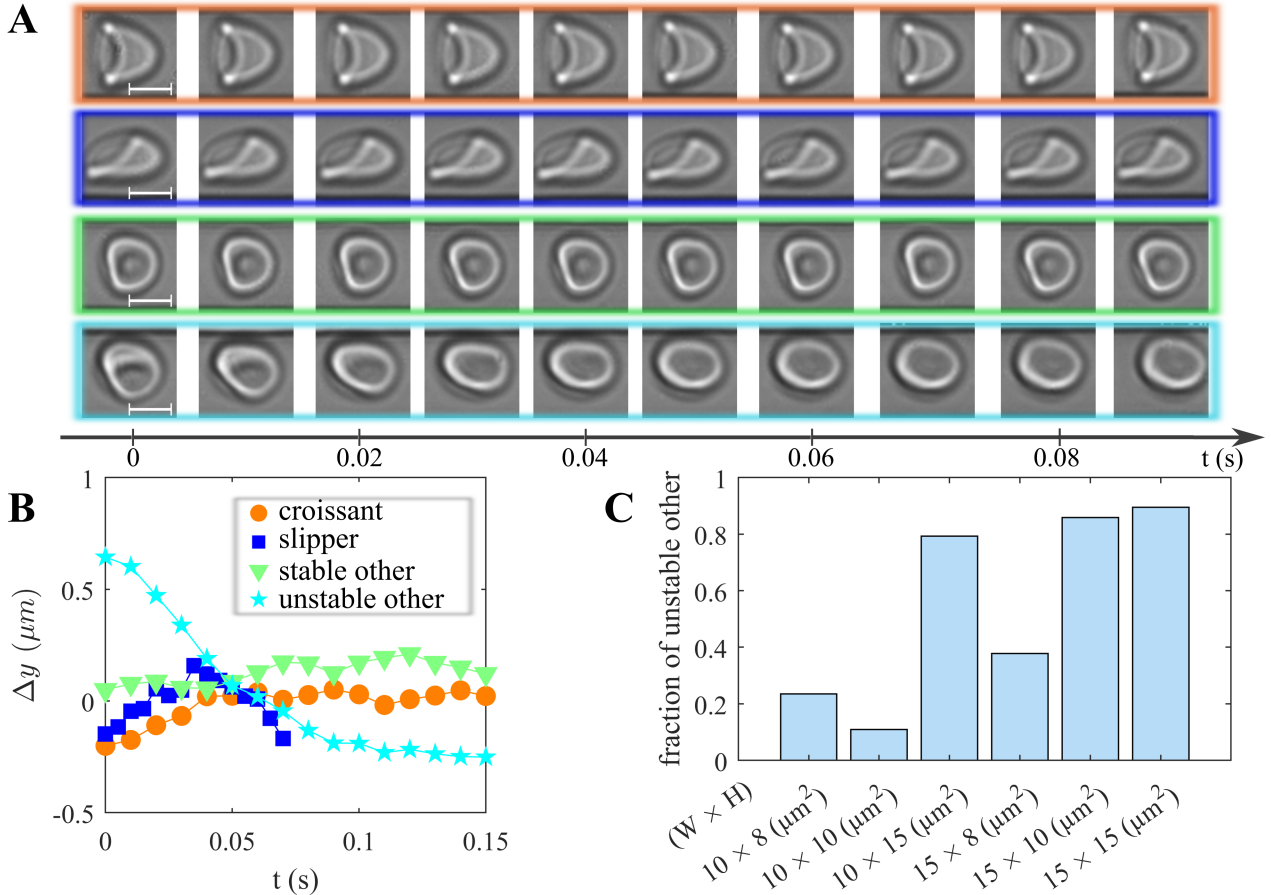


Figure 3.7: Analysis of stable and unstable RBC shapes: A- Representative image sequences exhibit the dynamic behaviour of different RBC shapes within a microfluidic channel measuring $W = 10 \mu\text{m}$ and $H = 8 \mu\text{m}$. The observed shapes include croissant, slipper, stable 'other,' and unstable 'other,' with scale bars denoting $5 \mu\text{m}$. Time evolution between consecutive images is depicted along the bottom axis. The observed shapes include croissant, slipper, stable 'other,' and unstable 'other,' with scale bars denoting $5 \mu\text{m}$. Time evolution between consecutive images is depicted along the bottom axis. B- Examination of lateral movement entails analysing deviations ($\Delta y = y_t - \bar{y}$) in the centre of mass position over time for the four representative cell shapes. C- Evaluation of the fraction of unstable 'other' cells relative to the total number of 'other' shapes provides insight into their prevalence across varied microfluidic channels utilized in this study. These findings contribute to a deeper understanding of RBC stability and behaviour in confined fluid environments.

the channel dimensions^[81,82,164]. In such large channels, RBCs can flow at off-centered streamlines and tumble and rotate more easily driven by the parabolic velocity profile than in the strongly confined channels. While we only classify other shapes as stable and unstable, previous work has revealed a plethora of dynamic RBC states, including tumbling, rolling, swinging, snaking, and tank-treading motions^[55,60,72]. Such dynamic RBC morphologies have received much attention as they can affect blood shear thinning behavior under microcirculatory flow conditions^[73,182]. Since approximately 20% of others exhibit unstable shapes in the channels that generate the highest fraction of stable croissants and slippers, a future research objective will be to investigate the exact nature of these shapes. For example, if tumbling trilobes or multilobes can be reliably detected within the field of measurements, this class could be inte-

grated into the shape phase diagram. Under pathological conditions when RBC deformability or membrane mechanical properties are impaired, and various unstable states emerge, such refined shape phase diagrams represent a central role in evaluating RBC flow behavior and could be used in diagnostic applications.

3.4 Conclusion

The experimental characterization of microscale RBC flow behavior has provided valuable insights into the dynamics of blood flow in confined microchannels. Consistent RBC shape state diagrams have been established, delineating the various configurations assumed by RBCs under different flow conditions. The complexity of RBC shapes across various confined microchannels highlights the intricate interplay between channel geometry and flow parameters. Particular significance has been observed for strongly confined channels with a height below $10\mu\text{m}$ and $\chi \approx 0.9$, where distinct RBC shapes emerge. The generation of characteristic croissant-peaks and slipper-plateaus at low and high velocities underscores the importance of flow dynamics in shaping RBC morphology. Furthermore, there is an observed increase in unsteady other cell shapes with larger channel dimensions, indicating the influence of channel geometry on RBC behavior. These findings have significant implications for future microfluidic designs employing RBC shape classification approaches, offering opportunities for tailored device development. Moreover, the influence of intrinsic cell properties on microscale blood flow has been elucidated, emphasizing the critical role of confinement effects and shear rate as external conditions impacting RBC shape.

CHAPTER II: EFFECT OF RED BLOOD CELL AGE AND MEMBRANE RIGIDITY ON SINGLE CELL CAPILLARY FLOW STABILITY

Contents:

4.1	Introduction	55
4.2	Experimental setup	58
4.2.1	Microfluidic Setup	58
4.2.2	RBC Sample Preparation	58
4.2.3	RBC Density Separation	59
4.2.4	Membrane Rigidification	60
4.3	Results	60
4.3.1	Stable RBC Shapes in Straight Microchannels	60
4.3.2	RBC Equilibrium Position in the Channel Cross-Section	63
4.3.3	Fraction of Stable RBC Shapes	64
4.4	Discussion	64
4.5	Conclusion	66

The following chapter is a reformatted reprint of the manuscript published in Cells^[131].

Abstract

Blood flow in the microcirculatory system is crucially affected by intrinsic red blood cell (RBC) properties, such as their deformability. In the smallest vessels of this network, RBCs adapt their shapes to the flow conditions. Although it is known that the age of RBCs modifies their physical properties, such as increased cytosol viscosity and altered viscoelastic membrane properties, the evolution of their shape-adapting abilities during senescence remains unclear. In this study, we investigated the effect of RBC properties on the microcapillary in vitro flow behavior and their characteristic shapes in microfluidic channels. For this, we fractionated RBCs from healthy donors according to their age. Moreover, the membranes of fresh RBCs were chemically rigidified using diamide to study the effect of isolated graded-membrane rigidity. Our results show that a fraction of stable, asymmetric, off-centered slipper-like cells at high velocities decreases with increasing age or diamide concentration. However, while old cells form an enhanced number of stable symmetric croissants at the channel centerline, this shape class is suppressed for purely rigidified cells with diamide. Our study provides further knowledge about the distinct effects of age-related changes of intrinsic cell properties on the single-cell flow behavior of RBCs in confined flows due to inter-cellular age-related cell heterogeneity.

Keywords: Red blood cell aging, membrane rigidity, microcapillary flow, cell fractionation, diamide treatment, shape adaptation

4.1 Introduction

Microvascular blood flow is vital for gas exchange and nutrient transport between blood and tissues. In the microvascular network, vessel diameters are similar to the red blood cell (RBC) size. At rest, healthy RBCs have biconcave, discocyte shapes with a diameter of roughly $8\ \mu\text{m}$ and a thickness of $2\ \mu\text{m}$. They consist of a lipid bilayer membrane, a spectrin network on the inner surface, and the cytosol, which is rich in hemoglobin^[19,113]. In the small vessels of the microvascular network, highly deformable RBCs flow in a single file and dynamically adapt their shapes to the vessel flow conditions^[58,154,156], even passing through capillaries and apertures smaller than their own sizes^[65,67]. Hence, various RBC shapes are found *in vivo* under physiological flow conditions (Figure 4.1). In general, the RBC shape dynamics depend on external conditions, such as the vessel diameter and the flow rate, as well as intrinsic RBC properties, such as the membrane elasticity or the viscosity of the inner cytosol. Alterations in the RBC properties, such as impaired deformability, which is found in multiple diseases, such as malaria, diabetes, sickle cell disease, or neuroacanthocytosis syndrome^[16,74,183–185], impact the RBC shape and impair blood flow and microvascular RBC transport^[73,155]. However, the fundamental mechanisms through which such changes modify the RBC shape in microscale flows have not been characterized extensively. Microscale RBC flow is commonly studied using microfluidic *in vitro* experiments^[157–160,162,186,187], and numerical simulations^[63,81,129,163,188–190]. In microscale single-cell flow environments, RBCs display a variety of stable and dynamic shapes, which depend on the channel confinement, flow velocity, the properties of the surrounding medium, and biophysical cell properties. Even under steady flow conditions, RBCs can exhibit various dynamical states, including snaking, tumbling, swinging, and tank-treading motions^[55,60,73,191,192].

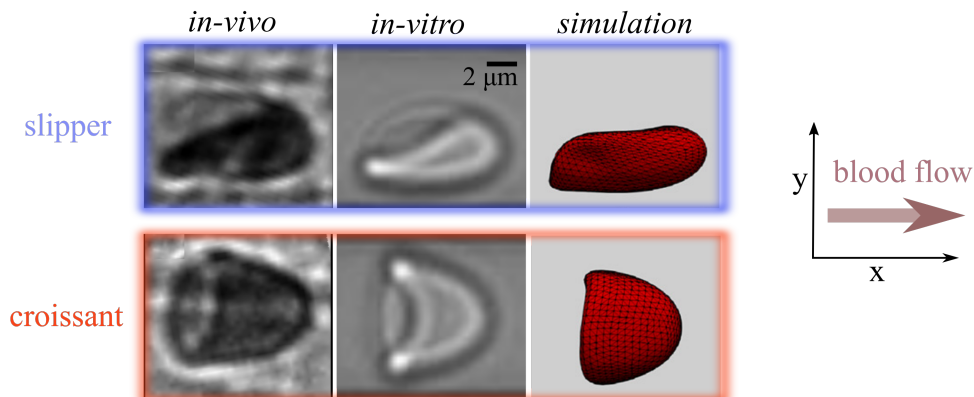


Figure 4.1: Bistability of RBC shape extracted from the total blood observed in the three environments: Representation of the centered flow croissant-like (bottom line) and off-centered slipper-like shape (top line) under the three observation environments^[74,131]. The light source caused the difference in cells colors (blue light *in-vivo* and red light *in-vitro*). Reproduced with permission from both Kihm *et.al* and Nouaman^[74,131].

In rectangular microfluidic channels with dimensions similar to the RBC size, the shape complexity is shown to reduce to two dominant RBC shapes, namely the so-called croissant and slipper shapes (check Figure 4.1)^[75]. Similar RBC shapes have been found in vivo in vessels of the human microcirculation^[58] and in hamsters (see Figure 4.1.A). In microfluidic channels, the symmetrically centered croissant shape predominantly appears at velocities below $v < 5\text{mm}\cdot\text{s}^{-1}$, while the asymmetric off-centered slipper shape is found mainly at velocities above $v > 3\text{mm}\cdot\text{s}^{-1}$. Consequently, a phase diagram of these main RBC shapes, as well as other shapes that do not exhibit stable modifications (presented in (Figure 4.1)), have been established to describe the occurrences of RBC shapes as functions of the flow rate in the microfluidic channel (Figure 4.2.B)^[75]. The resulting RBC shape in microcapillary flow is inherently coupled to its flow behavior, e.g., the cell's equilibrium position in the channel cross-section. For healthy samples, croissant-like RBCs preferentially flow at the channel's centerline at low velocities, whereas slippers flow closer to the channel's side walls at higher velocities, resulting in pronounced peaks in the probability density distributions (pdf) at $|y/W| \approx 0$ and $|y/W| \approx 0.22$, respectively (see Figure 3.5.A). Deviations from the equilibrium RBC distributions have previously been used to assess changes in RBC flow behavior in patients with neuroacanthocytosis syndrome and COVID-19, as well as in patients before and after undergoing hemodiafiltration dialysis^[78,79]. Moreover, RBC shapes in microfluidic capillary flow have been studied for healthy and diseased RBCs using manual and machine learning shape classification approaches^[74,77,80,193–195]. Recent studies have shown the potential of microfluidic characterizations of RBC shapes as biomarkers for specific pathologies, to assess the cell deformability^[78,164,166]. Nevertheless, fundamental knowledge about how the age of RBCs modifies their properties and, thus, affects their microcapillary flow, is still missing. RBCs have an average lifespan of 120 days in the circulatory system, after which, they are cleared by phagocytosis in the spleen based on their decreased deformability and other clearance mechanisms, which are still under debate^[38,89,196,197]. During their lifetime, RBCs pass many times through tiny capillaries and traverse inter-endothelial slits, undergoing complex shape transitions and experiencing physical stress. This induces intrinsic physiochemical and morphological changes, such as a loss of surface area and volume, delayed shape recovery, and increased density and cytosol viscosity^[198–205]. Numerical simulations generally show that changes in inner viscosity or the viscoelasticity of the membrane affect the RBC flow behavior^[76,85,86]. However, experimental validation of how stable RBC shapes, even for healthy donors, are influenced by the cell's age and corresponding RBC alterations remain scarce. Therefore, understanding the effect of age-induced changes in mechanical cell properties on the stable RBC shape signatures in microfluidic devices, which are used as fingerprints for in vitro microvascular flow assessment, is paramount. In this study, we examine the flow of RBCs through rectangular microcapillaries. Specifically, we investigate the effect of RBC age and reduced membrane deformability

on the stable RBC shape and the previously introduced shape phase diagram^[75]. Although such rectangular channels do not capture the geometry of mostly circular in vivo vessels, they allow us to study RBC flow with similar cell shapes (see Figure 4.1A) and cell velocities as in the microvascular network, under controlled flow conditions with good optical access. For this, RBCs from healthy donors are fractioned according to age using density gradient centrifugation methods^[150,206–208]. Furthermore, we treat fresh RBCs with a diamide at different concentrations to artificially increase the shear modulus of the RBC membrane and make the cells less deformable^[154,209]. This enables us to determine to what extent rigidification of the cell membrane can be related to the changes in RBC shapes in flow during aging. In both groups, we observe distinct differences in the stable cell shapes during capillary flow and the fraction of overall stable shapes. Our study aims to advance our understanding of the flow behavior of RBCs in confined vessels. Mainly, how alterations of RBC biophysical properties, such as their deformability, affect microvascular blood flow.

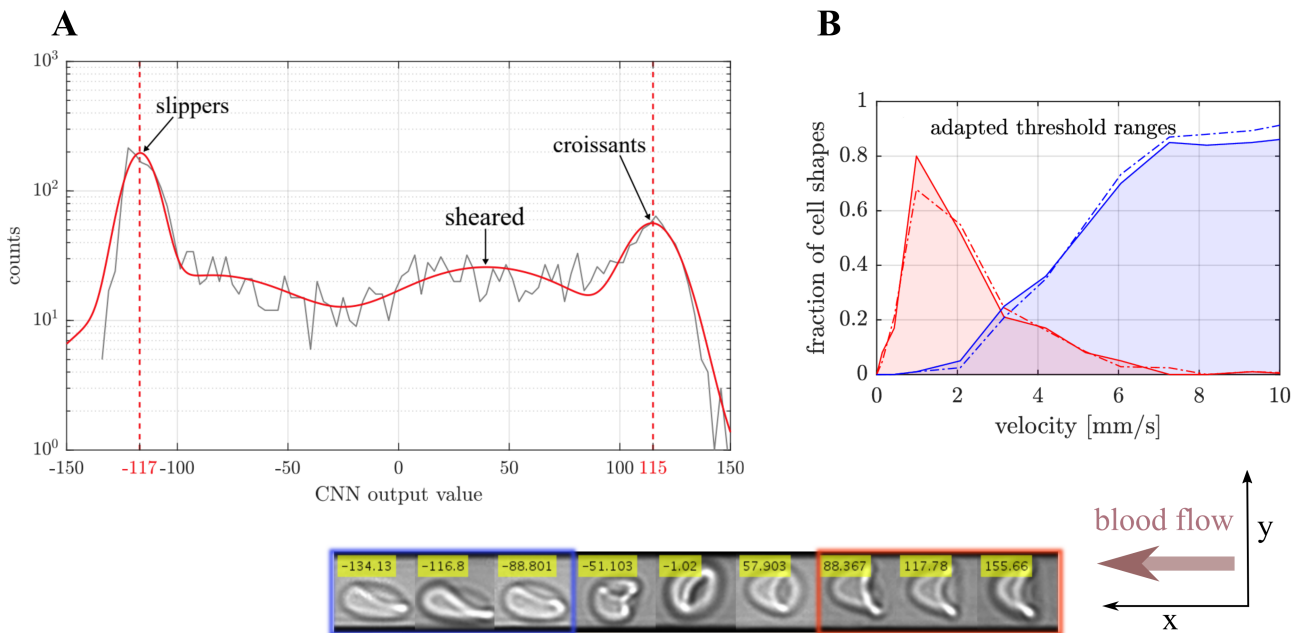


Figure 4.2: Artificial classification of the two main stable shapes of single RBC flow in a microfluidic channel^[74] with $W = 12 \mu\text{m}$ and $H = 10 \mu\text{m}$: A- Representation of the output of the trained a convolutional neural network (CNN) shows two pronounced peaks (-117 for slipper and 115 for croissant). B- Comparison between phase diagram obtained from both manually (hard lines) and CNN (dashed lines) shape classified. Using an adapted threshold range of CNN values till the both phase diagrams came to the same result. The cells presented at the bottom showing the values of the CNN output of each RBC shape category. *Originally published in Kihm et.al^[74] reproduced here with permission.*

4.2 Experimental setup

4.2.1 Microfluidic Setup

To assess the RBC shape in flow, we used rectangular microfluidic channels with a width of $W = 12.6 \pm 0.2 \mu\text{m}$, a height of $H = 7.7 \pm 0.2 \mu\text{m}$, and a total length of $L = 40 \text{ mm}$. The microfluidic device was fabricated using polydimethylsiloxane (PDMS, RTV 615A/B, Momentive Performance Materials, Waterford, NY, USA) through standard soft lithography, which was bonded to a glass slide using a plasma cleaner (PDC-32G, Harrick Plasma, Ithaca, NY, USA). The inlet and outlet of the microfluidic chips were connected with rigid medical-grade polyethylene tubing (with an inner diameter of 0.86 mm, Scientific Commodities, Lake Havasu City, AZ, USA) to the sample and waste containers, respectively. The microfluidic chip was mounted on an inverted microscope (Eclipse TE2000-S, Nikon, Melville, NY, USA), which was equipped with LED illumination (SOLIS-415C, Thorlabs Inc., Newton, NJ, USA). We used a high-speed camera (Fastec HiSpec 2G, FASTEC Imaging, San Diego, CA, USA), and a $60\times$ air objective (Plan Fluor, Nikon, Melville, NY, USA) with a numerical aperture $NA = 1.25$; we imaged the RBC flow in the the microfluidic chip at $\frac{3}{4}L = 30 \text{ mm}$ away from the inlet. We used a high-precision pressure device (OB1-MK3, Elveflow, Paris, France) to apply constant pressure drops between $p = 50$ and 1000 mbar . A frame rate of up to 400 frames per second was used to record the image sequences of RBC passing the field of view. RBC shapes in flow were classified manually according to Guckenberger et al. [75]. All microfluidic experiments were performed at 22°C . The center of mass of each cell in the projection plane was determined with a custom MATLAB (9.14.0.2206163 (R2023a), The MathWorks, Natick, MA, USA) algorithm, and individual cell velocities were determined by tracking the cell position over the image sequence within the field of view. In the applied pressure drop range, the resulting RBC velocity was between $v = 0.5$ and $9 \text{ mm}\cdot\text{s}^{-1}$ (see Figure 1.7.A and Figure 4.2.B). For the used microfluidic chip, we estimated the nominal wall shear rate in the straight channel as $upgamma \approx 6v/H \approx 400 - 7000 \text{ s}^{-1}$. Based on the viscosity of the surrounding medium of $1.2 \text{ mPa}\cdot\text{s}$, we estimated the shear stress to be between $\tau \approx 0.5$ and 8.4 Pa .

4.2.2 RBC Sample Preparation

Blood was collected into EDTA-containing tubes (1.6 mg/mL EDTA, SARSTEDT, Nümbrecht, Germany) with informed consent from three healthy male voluntary donors (age 28–31 years). It was centrifuged for 5 min at $3000\times g$ to separate RBCs and plasma. Sedimented RBCs were washed three times with a phosphate-buffered-saline solution (Gibco PBS, Fisher Scientific, Schwerte, Germany). Finally, a hematocrit concentration of $1\%Ht$ was adjusted in a PBS solution that contained $1g/L$ bovine serum albumin (BSA, Sigma-Aldrich, Taufkirchen, Germany) (full process described in Figure 2.1). The viscosity of the PBS/BSA solutions at 20°C was

approximately 1.2 mPa.s^[76], similar to the viscosity of human blood plasma. Since we do not observe significant inter-individual variations in the results, data were averaged between the three donors. Blood withdrawal, sample preparation, and microfluidic experiments were performed according to the guidelines of the Declaration of Helsinki and approved by the ethics committee of the “Ärzttekammer des Saarlandes” (permission number 51/18).

4.2.3 RBC Density Separation

To fractionate RBCs based on their age, we performed Percoll density gradient centrifugation following the method described by Ermolinskiy et al.^[150]. In brief, the Percoll solution (Cytiva 17-0891-01, Sigma-Aldrich, Taufkirchen, Germany), distilled water, and a 1.5M NaCl solution were mixed at five different ratios to obtain gradient solutions with different densities. Then, 2mL of washed RBCs with 50% Ht in PBS ($\rho = 1.025$ g/mL) were centrifuged on top of five layers of Percoll gradients with densities of 1.085 g/mL, 1.092 g/mL, 1.101 g/mL, 1.107 g/mL, and 1.122 g/mL (see Table 2.2 and Figure 4.3.A).

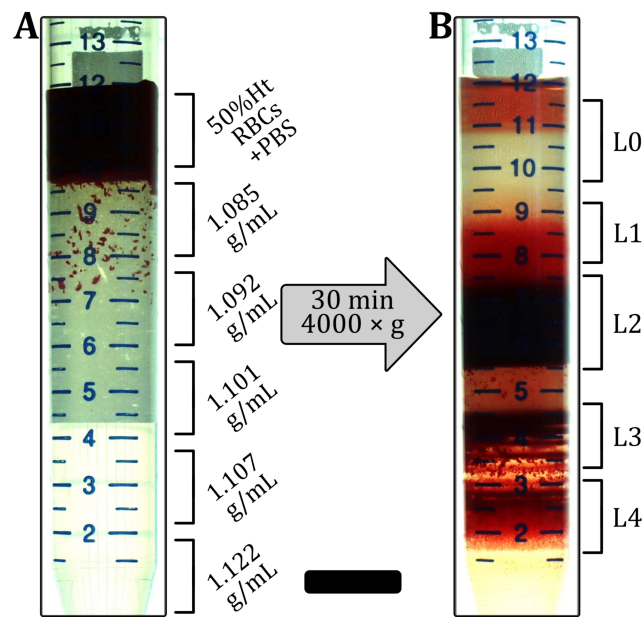


Figure 4.3: The main solution of the density separated RBCs into discontinuous layers (L0-L4): A- The first preparation of the solution composed with four decreasing dense (the process is described in Figure 2.2.B) Percoll solutions (from bottom to top) plus an additional top layer that contains washed RBCs 50% diluted in PBS.). B- Solution obtained after 30 minutes of centrifugation, showing different layers of RBCs (L0 is neglected due to its containing: very few amount of RBCs plus waste and proteins). The black bar is 1cm scaled. *From the work of Nouaman et.al*^[131].

After centrifugation for 30 min at $4000 \times g$ at a temperature of $4^\circ C$, four fractions of RBCs were obtained (Figure 4.3.B) with the youngest cells in the top layers and the oldest cells in the bottom layer. Note that the different number of cells in each layer led to different shifts in the height of each layer. The topmost layer (L0 in Figure 4.3.B) contained the PBS with mostly reticulocytes and leukocytes and was, therefore, not used in the microfluidic experiments.

The other layers (L1–L4) were carefully extracted from the top to avoid any mixing. The fractionated RBCs were subsequently washed with PBS and resuspended at a hematocrit of 1%Ht in the PBS/BSA mixture.

4.2.4 Membrane Rigidification

For the artificial membrane rigidification, fresh-washed RBCs were incubated in diamide (Sigma-Aldrich, Taufkirchen, Germany) for 30 min at diamide concentrations of 0mM, 0.5mM, 1mM, and 2mM. Diamide was proposed to induce a cross-linking between the spectrin proteins^[68].

4.3 Results

4.3.1 Stable RBC Shapes in Straight Microchannels

Similar to the previously established phase diagram of stable RBC shapes (see Figure 1.7.B), we examined the influence of the RBC age and artificially induced membrane rigidity on shape alterations within rectangular microchannels, focusing on the three dominant RBC shape classes, namely croissants, slippers, and others. The resulting cell velocities v in the microchannels are in the range of 0.5–9 mm.s⁻¹, similar to the flow in the microvascular network^[19,155]. For the density-fractionated cells, the number of croissant-shaped RBCs increases with increasing age (Figure 4.4.A). While the peak value of the croissant fraction increases from roughly 25% to 75% from L1 to L4, the corresponding velocity of the croissant peak remains at approximately 1 mm.s⁻¹, in accordance with previous studies^[74,75]. Furthermore, croissant-like shapes also appear at velocities $v > 5$ mm.s⁻¹ for L3 and L4, whereas no significant numbers of such shapes are found at the same velocities for L1 and L2. Concurrently, the amount of slipper-like shapes decreases with the increasing age between the layers. While a plateau value for the slipper fraction of roughly 80% is observed for $v > 6$ mm.s⁻¹ for L1 and L2, this value decreases sharply below 20% for L4. Additionally, the amount of other RBC shapes increases as the RBC age and density increase.

Based on the elongation index (EI) measurements^[131], we used the same RBC treatments for our microchannel approach. Increasing the membrane shear modulus also affects the formation of the stable croissant and slipper-like shapes (Figure 4.4.B). While the control (0mM) exhibits the characteristic croissant peak at $v \approx 1$ mm.s⁻¹, increasing the diamide concentration leads to a reduction in the peak fraction and a shift of the peak position toward higher velocities of approximately 3 mm.s⁻¹ for a concentration of 2mM. Furthermore, the croissant distribution in the shape phase diagrams broadens significantly, leading to the emergence of croissant-like shapes at $v > 5$ mm.s⁻¹ with an increasing diamide concentration. Simultaneously, the slipper plateau regime, which is observed at $v > 5$ mm.s⁻¹ for the control with 0mM, continuously decreases as the diamide concentration. At 2mM, the occurrence of slipper-like

RBCs is ultimately suppressed, nearly completely, whereas most cells exhibit other shapes at high velocities. Based on the 2D projection of the RBCs in the x-y-plane of the microfluidic channel, we calculate the projection area A during the capillary flow. With the increasing age (L1–L4), the median projection area decreases at both low and high velocities (Figure 4.5.A).

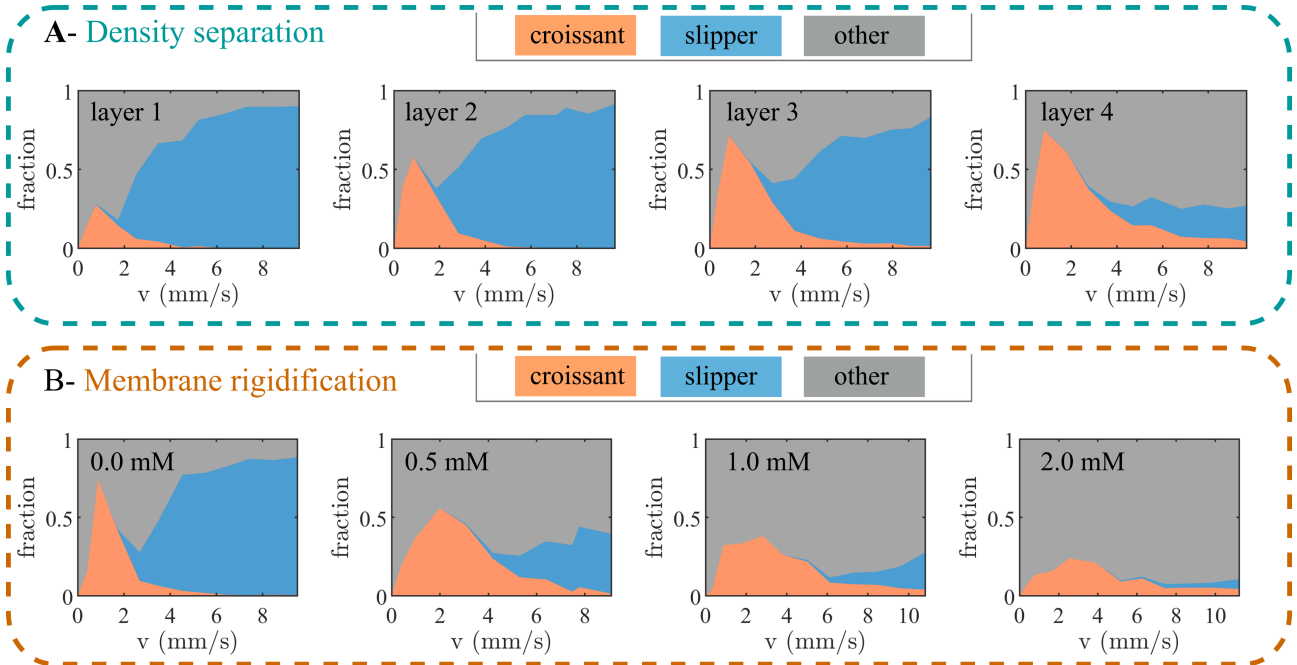


Figure 4.4: Phase diagrams of the RBC shape regarding its density (A) and membrane rigidity (B) s in a width of $W \approx 10 \mu\text{m}$ and $H \approx 8 \mu\text{m}$ microfluidic channel: A- The set of phase diagrams that illustrates the fractions of each of RBC shape (croissant, slipper and other) according to each density layer where RBCs were collected (density increasing with layers), as a function of velocity of the cell. B- Fractions of rigidified RBCs membrane into different molecular concentrations of diamide (between 0.0 and 2.0 mM), as a function of velocity. The analyses were performed on an average of 10,677 cells per donor (between 6361 and 14,268 cells) and 2871 cells per donor (between 1587 and 6168 cells), respectively.

In contrast, A increases with the increasing diamide concentration (Figure 4.5.B). Note that although the volume and surface area of the RBC are coupled, an increase in the projection area does not necessarily correspond to an increase in the cell volume, i.e., when the RBC volume increases and its shape changes from a discocyte to a more spherical shape, its projection area can decrease. Moreover, we calculate the deformability index DI of the RBCs during the capillary flow, which is often used to assess changes in cell deformability^[166]. Here, it is defined as $DI = (a - b)/(a + b)$, where a and b are the major and minor axes of the RBC shape during flow. For both age-fractionated RBCs and cells treated with diamide, the median DI at high velocities is larger than at low velocities (Figure 4.5.C,D) since the emergence of slipper-like shapes at elevated velocities leads to an elongation of the cell. While the deformability index does not significantly change at low velocities for both cases, we observe a drastic decrease in DI with the increasing diamide concentration at high velocities (Figure 4.5.D). This effect is attributed to an increase in other shapes that emerge as the diamide concentration increases

(see Figure 4.4.B). These shapes often have more spherical, less elongated morphology (see Figure 4.1) and, thus, a lower DI. Note that this decrease in the deformability index DI with the increasing diamide concentration assessed in the capillary flow is in accordance with the observed decrease in the elongation index EI from the ektacytometry measurements^[131].

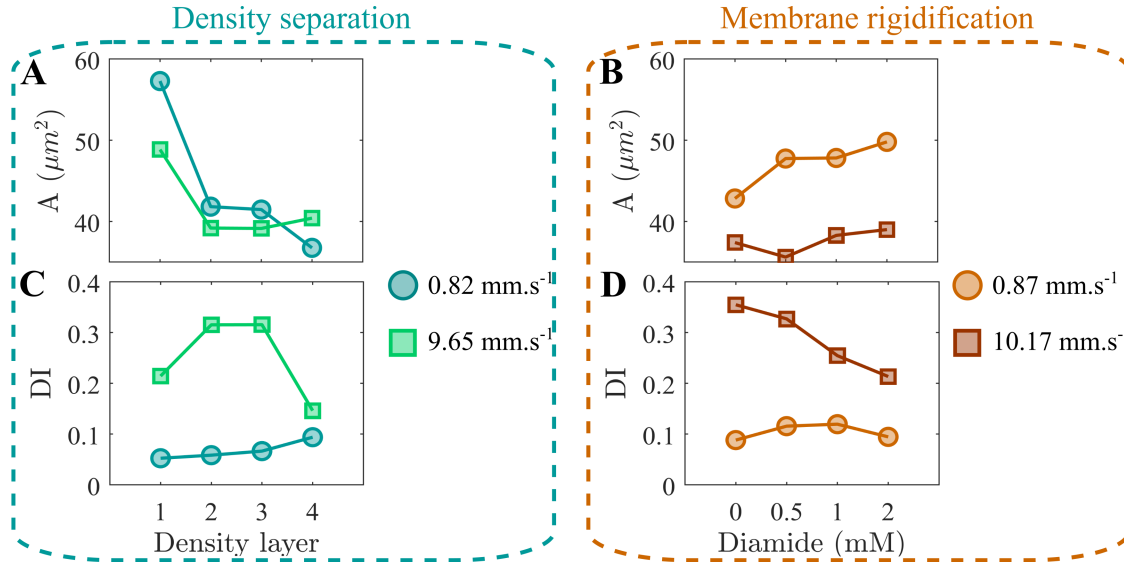


Figure 4.5: Changes of both projected RBC area (top row) and deformability (bottom row) of the membrane along a region of interest ($\text{ROI} \approx 300\mu\text{m}$) at low (circle) and high (square) mean velocity of RBCs under both effects, age and membrane rigidity: Left column- Median values of projected area on x-y plane of RBCs extracted from each density separation layer (A) and the median values of deformation index DI (C). Right column- The area (B) and DI (D) of RBCs as a function of diamide concentrations.

Moreover, for L4, we also observe a reduced median deformability index at high velocities. In this case, the occurrence of both other and slipper-like shapes leads to a pronounced double-peak profile in the DI distribution, which results in a decreased median DI (see Figure 4.6).

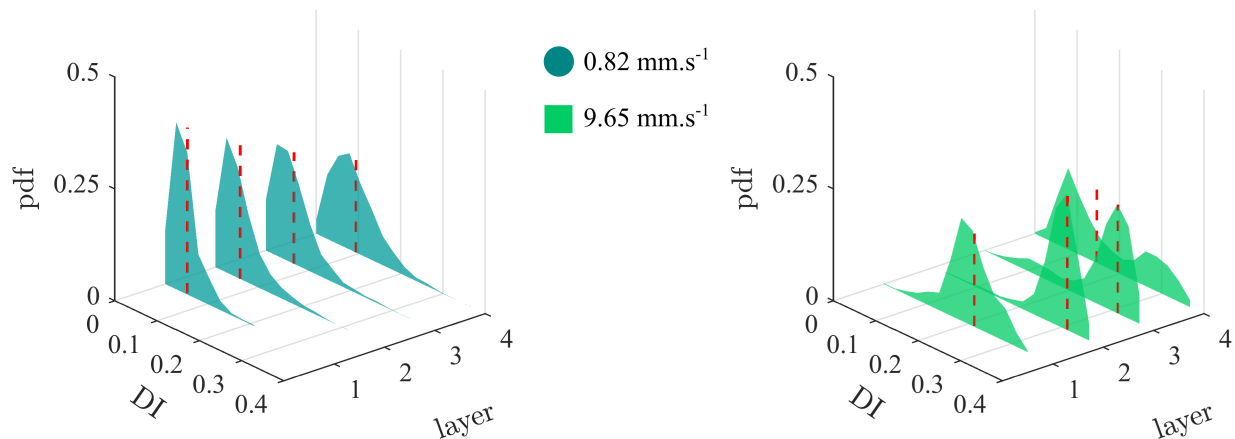


Figure 4.6: Probability density functions of DI distributions of RBCs from (L1-L4) at low (left graph) and high (right graph) velocities. The red dashed lines show the median values of DI presented on Figure 4.5.C.

4.3.2 RBC Equilibrium Position in the Channel Cross-Section

The RBC shape is inherently linked to its equilibrium position in the microchannel. While symmetric croissants generally flow at centered positions, asymmetric slippers emerge at off-centered positions with respect to the channel width W , as reported previously for fresh blood [75]. In the present study, the equilibrium position across the channel width is assessed based on the probability density distribution (pdf) of the absolute value of the normalized RBC y -position $|y/W|$ as a function of the velocity (Figure 4.7). For all density-separated layers L1–L4, we observe a pronounced peak in the pdfs at the channel centers $|y/W| \approx 0$ at low velocities $v < 5 \text{ mm}\cdot\text{s}^{-1}$ (Figure 4.7.A). As the velocity increases, the central position is less favorable and an off-centered peak emerges at $|y/W| \approx 0.22$. For L1 to L3, this off-centered distribution corresponds to the shape transition toward slipper-like cells (see Figure 4.4.A). In contrast, the pdfs at high velocities for L4 show broader distributions, comprising a second pronounced central peak, indicative of the croissant-like shape and other RBC shapes that emerge at $v > 5 \text{ mm}\cdot\text{s}^{-1}$ and $|y/W| \approx 0$ for L4. Without the addition of diamide, the y -position distributions for fresh RBCs show the characteristic central or off-centered peaks at low or high velocities, respectively (0mM in Figure 4.7.B). However, increasing the diamide concentration dramatically affects the equilibrium RBC position across the channel width. At a concentration of 0.5mM, we find a large number of cells that flow closer to the channel center, as evidenced by the emerging peak around $|y/W| \approx 0$ at high velocities.

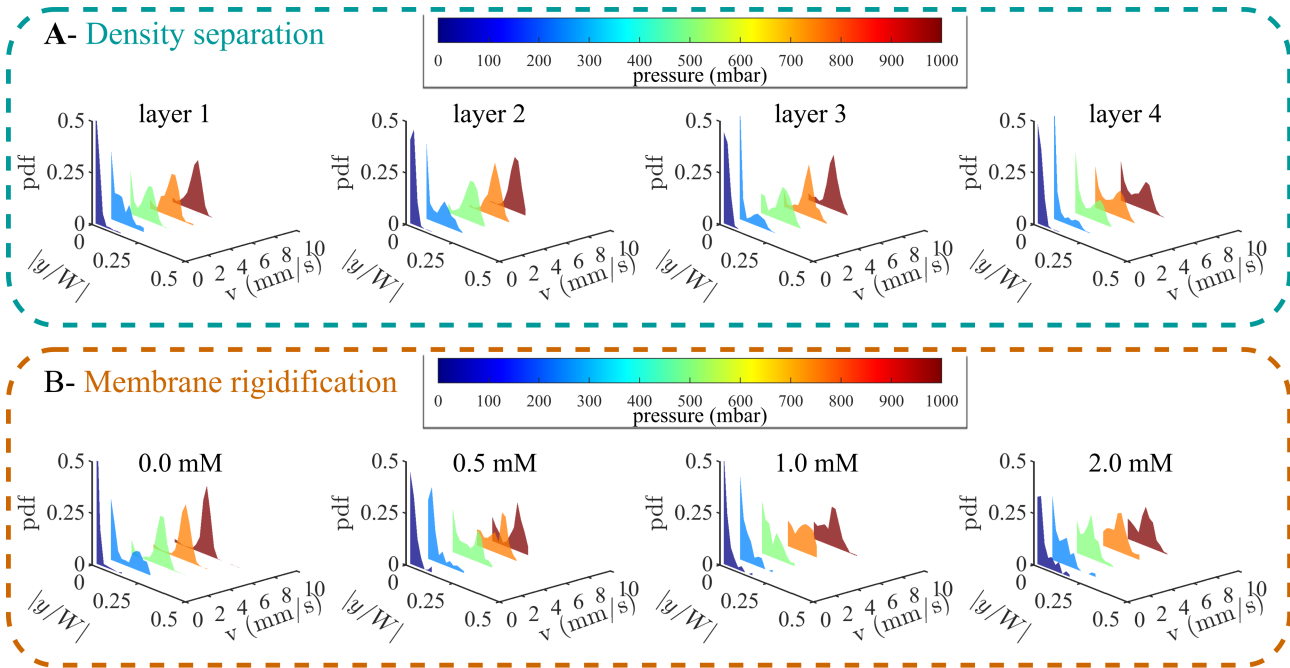


Figure 4.7: Probability density distributions of the absolute values of the RBC y -position normalized by the channel width $|y/W|$. Data are shown for five velocities for (A) the different density layers (L1–L4) and (B) diamide concentrations based on the data treated in Figure 4.4.

Simultaneously, the off-centered slipper peak is still visible, similar to the observations for L4. This effect qualitatively persists as the diamide concentration is further increased. At diamide concentrations above 0.5mM, more cells flow between the channel's centerline and the off-centered position of the slipper peak, in accordance with the occurrence of other shapes beyond the stable croissants and slippers.

4.3.3 Fraction of Stable RBC Shapes

The changes in the RBC density and membrane rigidity affect the emergence of stable RBC shapes. Here, we define a stable shape when it does not rotate, tumble, or exhibit any other dynamic that significantly changes the cell's y-position or shape within the field of view of approximately 300 μm along the flow direction. Note that the field of view is 20 mm downstream of the channel entry, which is long enough for any transient effects of the inlet to decay and achieve a stable shape configuration for all applied pressure drops^[75,181]. In our study, the fraction of stable shapes decreases with the increasing RBC age for the density-fractionated cells (Figure 4.8.A). While nearly all cells have the same shape in the field of view of L1, only 63% of the RBCs in L4 exhibit a stable shape. This decrease is in line with the increasing number of other shapes in the phase diagrams as the cells age (see Figure 4.4.A). In the absence of diamide, roughly 90% of fresh RBCs exhibit stable shapes (Figure 4.8.B), similar to the average value between L2 and L3. This fraction continuously decreases with the increasing diamide concentration, reaching 30% for cells treated with 2mM diamide.

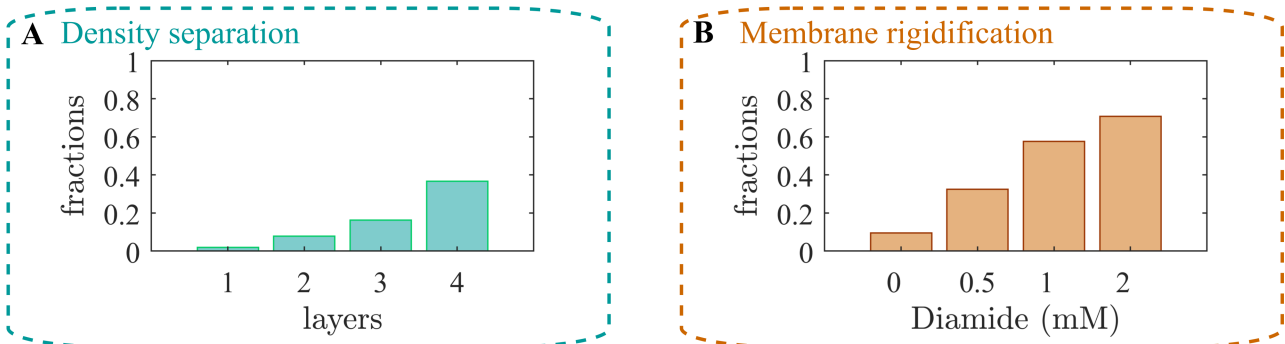


Figure 4.8: Fractions of RBCs that show time-evolution of their shapes (i.e. rotation or tumbling...) within the field of view during capillary flow: A- Fraction of unstable RBC extracted from the different density layers (L1–L4) and B- as a function of the diamide concentration. The classifications were performed on an average of the same amount of data declared on the caption Figure 4.4.

4.4 Discussion

In this work, we study the effect of the RBC age and artificially induced membrane rigidity on the RBC shape in the flow setting, based on microfluidic experiments carried out on blood triplicates. We observe significant alterations in the RBC capillary flow behavior, specifically the

stable RBC shapes, their equilibrium positions, and the fraction of stable shapes, as functions of both the RBC age and the different diamide concentrations. Foremost, the formation of slipper-like cells is continuously suppressed with the increasing age or diamide amount. Moreover, croissant-like RBC shapes start to emerge at higher velocities in this case. However, while the pronounced croissant peak corresponding to low velocities increases for old cells, it flattens down with the increasing diamide concentration. While we also observe changes in the deformability index and the projection area of the RBCs during the capillary flow, the shape phase diagram was recently shown to allow for a more precise evaluation of changes in RBC properties compared to such geometric parameters^[195]. Note that L2 comprises the largest fraction of whole blood (see Figure 4.2.B), with L3 being the second largest. Hence, the results of the control measurements without diamide (0mM) resemble the results of L2 and L3 regarding the phase diagram, the y-position distributions, the deformability index, the RBC projection area, and the fraction of stable shapes. This finding highlights the inter-cellular heterogeneity of fresh RBCs regarding their deformability. Characterizing sub-populations and individual cells has received increasing attention since such methods complement traditional hematological tests that rely on the average and mean values of RBC properties^[210]. In general, the RBC shape in the microcapillary flow is primarily influenced by the intrinsic cell properties under otherwise fixed external conditions, i.e., velocity, channel geometry, confinement, and rheological properties of the surrounding fluid. The two main intrinsic parameters that were shown to influence the RBC dynamics in previous experimental and numerical studies are the cytosol and the properties of the plasma membrane. As the RBC ages, the viscosity of the cytosol increases, which was already suggested to suppress cell deformation, in general^[65,200,211,212]. Consequently, the viscosity contrast λ between the viscosity of the cytosol and the surrounding fluid has been extensively studied, primarily using numerical simulation, which allows for a straightforward adjustment of λ . Although many studies use $\lambda = 1$, it was shown that the viscosity contrast critically affects the flow of single vesicles and RBCs in the linear shear and Poiseuille flow^[82,119,182,189,213–219]. In microfluidic experiments, the viscosity of the cytosol cannot be determined and changed straightforwardly. Nevertheless, the viscosity contrast can be tuned by changing the outer viscosity by using dextran solutions. Recent experiments in rectangular microchannels with a diameter similar to the RBC size demonstrated that decreasing the viscosity contrast λ results in the emergence of slipper-like RBCs at lower cell velocities^[76]. This is in qualitative agreement with our observations that with a decreasing RBC density, hence, decreasing λ , slippers are the predominant shape (see Figure 4.4.A). As λ increases with increasing age, the fraction of highly deformed, asymmetric, slipper-like RBCs decreases. Simultaneously, the occurrence of centered symmetric croissants appears to be enhanced by a higher inner viscosity, as indicated by the strong peak for L4. Nevertheless, not only do the properties of the cytosol change as the RBC ages, but also the properties of the cell mem-

brane, including the elastic shear modulus and membrane viscosity^[198]. For healthy RBCs, the cell membrane exhibits viscoelastic properties and deforms at a constant surface area during the flow. In numerical simulations, the RBC membrane and the mechanical properties of the spectrin cytoskeleton are, therefore, often modeled as a two-dimensional elastic membrane with resistance to shear and area dilation, as well as resistance to bending^[220–222], which allows capturing dynamic and steady RBC shapes^[81,164,182,189,215,223–225]. The effect of an artificial increase in the shear modulus of the RBC membrane is clearly visible in our microfluidic experiments (see Figure 4.4.B). Early micropipette aspiration experiments already highlighted that the deformation of RBCs depends on the viscous and elastic properties of the cell membrane^[226]. These concepts were integrated into numerical simulations, which recently showed that the microcapillary RBC dynamics are crucially affected by the characteristics of the cell membrane, whether it is modeled as purely elastic or viscoelastic^[85,86,227]. Gürbüz et al.^[86] found that the RBC shapes with membrane viscoelasticity resemble the experimentally observed shapes during the start-up in a 10 μ m capillary^[138]. Although both approaches with and without the incorporation of a membrane viscosity result in the formation of centered symmetric cell shapes, the shape transition time and the exact RBC deformation patterns are significantly influenced by increasing the membrane viscoelasticity. Based on the data of Gürbüz et al.^[86], the resulting stable cell shapes with increased membrane viscoelasticity would be classified as others in our work. Thus, we hypothesize that increasing the viscoelastic properties of the RBC membrane results in the suppression of highly deformed slipper cells at high velocities in combination with the emergence of other non-stable cells, in accordance with the observations of L4 and an increasing diamide concentration (see Figure 4.4). Based on the assumption that with the increasing RBC age, the membrane rigidity increases, we note that the phase diagram of L4 resembles the one of a diamide concentration of 0.5mM. However, while increasing the amount of diamide further suppresses slipper-like cells, it also decreases the number of croissants at low velocities. This indicates that the microcapillary flow behavior of older RBCs is indeed governed by both an increase in the membrane rigidity and an increase in the cytosol viscosity.

4.5 Conclusion

To conclude, our results demonstrate the sensitivity of the RBC shape on their age-induced intrinsic properties, highlighting the importance of considering the heterogeneity of cell populations in microfluidic deformability assessments or diagnostic applications. Moreover, regarding the investigations on *in vivo* aged cells, we show that the artificial rigidification of the membrane with a low diamide concentration (0.5mM) resembles the microcapillary flow behavior of the oldest RBC fraction the most. *In vivo*, the entire situation is more complex, because, in addition to the RBC properties, the conditions in the microcapillaries are less well-defined. This starts with the geometry of the vessels, which are different from the microfluidic channels, and

even diameters may be subject to temporal alterations due to vasodilation and vasoconstriction. This continues with a varying flow speed due to a changing pulse rate and blood pressure. Finally, the physiological and pathological variations of the blood plasma composition alter the biophysical effects (λ) as well as the biochemical effects on RBC flow properties^[79]. Therefore, our study presents an initial methodological in vitro framework for future experimental and numerical investigations of how alterations in RBC properties influence their shape in capillary flow at the single-cell level. This research is highly relevant for the accurate simulations of RBCs and the in silico modeling of blood flow.

CHAPTER III: DEFORMABILITY OF RED BLOOD CELL THROUGH A COMPRESSION-EXPANSION PROCESS

Contents:

5.1	Introduction	70
5.2	Materials and Methods	74
5.2.1	Blood Collection and Samples Preparation	74
5.2.2	Microfluidic Setup	74
5.2.3	Deformation Coefficient	76
5.2.4	Fit Model	76
5.3	Results	77
5.3.1	Deformation Illustration	77
5.3.2	Deformation Distributions	78
5.3.3	Effect of Age and Rigidity on Deformability	79
5.3.4	Deformation Rate and Deformation Time	82
5.3.5	Relaxation Effect	83
5.4	Discussion	85
5.5	Conclusion	87

Abstract

The deformability of red blood cells (RBCs) is a crucial physical property that profoundly influences their flow behavior within the circulatory system. Numerous methodologies have been employed in prior studies to characterize this property, considering various concepts such as stiffness, deformation, and elongation under differing flow conditions experienced by RBCs. Our investigation focuses on a specific flow process involving compression, where RBCs traverse a highly confined channel width, followed by expansion through a wider channel width. To quantitatively assess the deformation experienced by RBCs in both channel widths and the magnitude of deformation acquired during this process, we characterize this using the deformation index (DI). This chapter discusses how various parameters, including density and membrane rigidity, influence the evolution of the DI in our setup. Our study aims to elucidate how alterations in RBC deformability impact both blood flow dynamics and broader physiological phenomena.

Keywords: Red blood cell deformability, compression-expansion flow, deformation index, density, membrane rigidity, blood flow dynamics

5.1 Introduction

The shape of red blood cells (RBCs) is crucial to their function within the bloodstream. Deformability, a fundamental rheological property of RBCs, depends on several parameters (see Table III.1), each of which may or may not be examined individually depending on the chosen measurement methodology. The physical deformation of RBCs is a reversible process within certain limits (remaining in the Young's modulus range: ($\sim 2 - 8$ kPa)^[228,229], and once the applied force is removed, the cell returns to its relaxed state. However, excessive mechanical stress can damage RBCs^[230-232]. When RBCs encounter confinement within microcapillaries or narrow blood vessels, specific mechanical forces such as shear stress and local tubular hematocrit come into play, affecting their shape and behavior. Confinement can cause RBCs to compress, deform, or stretch, temporarily changing their morphology. Compression occurs when RBCs pass through narrow spaces, causing them to elongate and deform to fit the diameter of the vessel^[179,233-235]. Deformation refers to changes in the shape of RBCs due to external pressure, which can lead to temporary changes in morphology^[236,237]. Stretching involves the expansion of RBCs upon exposure to wider areas after passing through narrow passages^[238-241]. In vivo observations have demonstrated these effects on RBCs as they traverse microcapillaries.

Studies using in vivo microscopic imaging techniques have provided insights into how RBCs deform and adapt their shape to navigate through complex vascular networks^[81,242,243]. These observations highlight the flexibility and adaptability of RBCs in response to changing environmental conditions such as confinement, shear stress, and local tubular hematocrit within the bloodstream, explaining their effects on RBC morphology and behavior. In addition, the altered shape of RBCs enhances the surface-to-volume ratio^[229,244–246], which improves the exchange of oxygen and nutrients with surrounding tissues. This dynamic interplay between RBC deformation, blood flow, and nutrient exchange is essential for maintaining tissue viability and overall physiological function.

Table 5.4: Rheological properties of normal adult RBC. There is an $\approx 40\%$ excess surface area over that required to enclose the cell volume in a sphere. The relation for a whole circulating RBC population fits to the regression $S = aV + S_0$, where $a = 1.1 \mu\text{m}^2/\text{fL}$ and $S_0 = 26.8 \mu\text{m}^2$; the mean $S/V = 1.37 \mu\text{m}^2/\text{fL}$. The lower column describes the measurement methods. *Originally published in Gifford et.al^[245] reproduced here with permission.*

Cell volume V (fL)	Surface area (μm^2)	Membrane viscosity ($\mu\text{N}\cdot\text{m}^{-1}\cdot\text{s}$)	Time shape recovery
$\approx 80 - 100$	$\approx 110 - 140$	0.6–2.7	0.12
Automated cell counter	Parallel microchannel	Micropipette aspiration	Micropipette aspiration

As RBCs age within the microvascular system, they undergo various changes that affect their density and volume. One notable phenomenon is a gradual decrease in cell volume and an increase in density as RBCs age^[247,248], but also. This development can be attributed to several factors, including loss of water content, changes in membrane composition, and accumulation of metabolites.

Over time, due to the absence of protein synthesis, the activity of enzymes—particularly those involved in the neutralization of oxidants—gradually declines. As a result, oxidative damage affects various components within RBCs, including hemoglobin, cytoskeletal proteins, and membrane lipids, leading to increased cell membrane rigidity. Dysfunction of ion pumps results in loss of potassium and water, resulting in increased hemoglobin concentration and subsequent increased cytoplasmic viscosity^[249–252]. The complexity of the erythrocyte aging process appears to lie in both the transformation of the cell itself and its progressively decreasing ability to undergo reversible deformation, which results from these cellular transformations^[200,253–255]. Various environmental factors can affect the mechanical properties of the erythrocyte membrane, leading to stiffness and rigidity. Exposure to oxidative stress, inflammation, or pathological conditions can lead to the formation of oxidation products and membrane damage, making the membrane stiffer and less elastic^[256–258]. Furthermore, changes in membrane lipid composition, such as increased cholesterol levels or decreased phospholipid content, can contribute to membrane stiffness^[259,260]. Red blood cell membrane stiffness can impede the cell’s ability to deform and move through narrow capillaries^[131], resulting in altered blood flow and decreased oxygen delivery to tissues. In addition, stiff RBCs are more susceptible to lysis and

clearance by the reticuloendothelial system, further compromising their functional integrity in the bloodstream^[261,262]. Diseases called membraneopathies and hemoglobinopathies complexly reshape the rheological properties of RBCs, disrupting fluid dynamics within macrovascular and microvascular systems. These changes in RBC properties can lead to diverse clinical manifestations, including anemia, organ ischemia, and hypertension^[16,54,239,263–267]. In complex diseases such as diabetes or obesity, changes in RBC deformability often appear as important consequences of the underlying pathological mechanisms^[268–270].

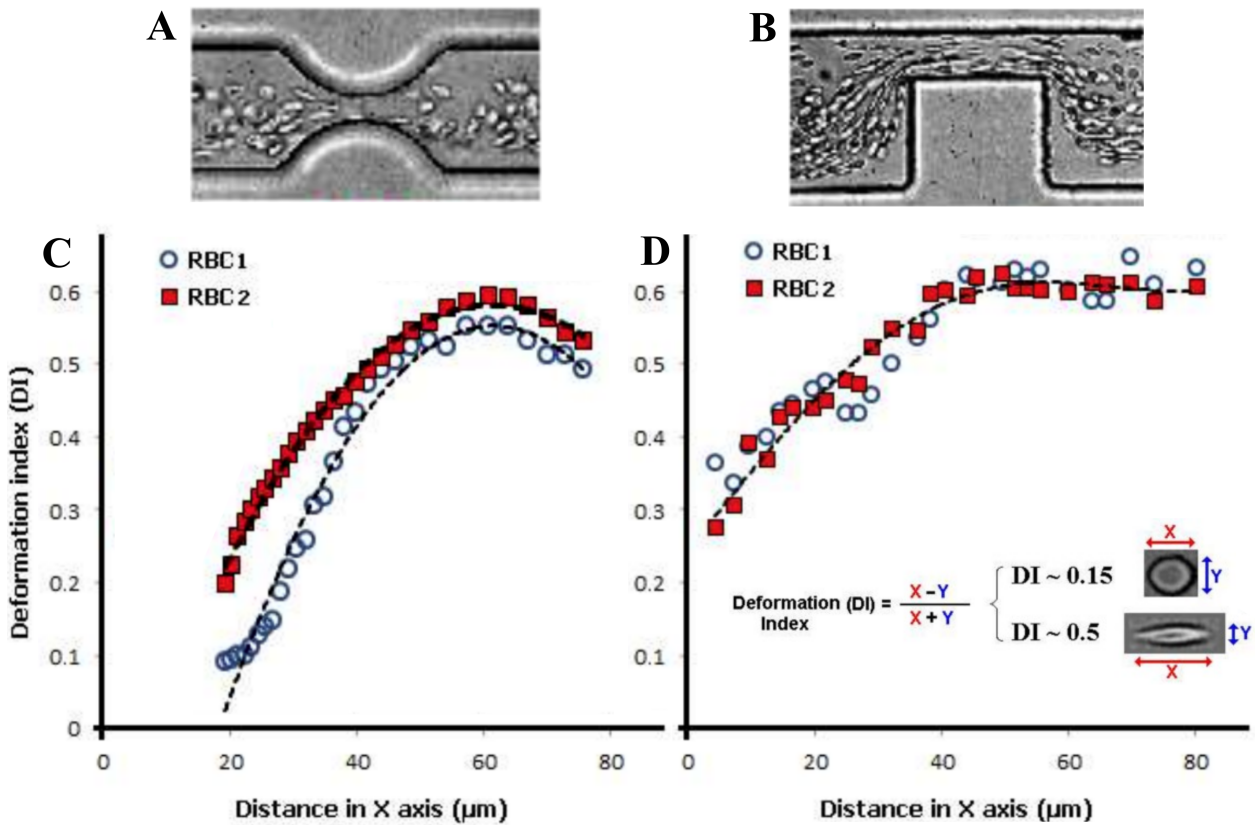


Figure 5.1: Red blood cells flowing through a microchannel with (A) a smooth and (B) a sudden (or abrupt) contraction^[271]: Individual RBC deformation index (DI) flowing through (C) smooth and (D) sudden contraction microchannel for the same flow rate. Adapted from Lanotte *et.al*^[73].

In the opening chapter of our investigation, we explored the flow behavior of RBCs at the microscopic level through experimental characterization. This research work aims to clarify the consistent patterns observed in RBC shapes and to identify the complex array of RBC morphologies encountered within different confined microchannels. By carefully evaluating the morphologies of RBCs in microcapillary flow settings, our results emphasize the paramount importance of tightly confined channels, especially those with a height of less than 10 μm and a dimensionless confinement coefficient (χ) of approximately 0.9, along with a rectangular cross-section^[131,132]. Within such confined environments, observations revealed distinct morphological features, notably the appearance of distinct croissant-shaped peaks at low velocities

and slipper-shaped plateaus at high velocities^[74,75,131,132].

In this chapter, our focus will be on exploring the unique ability of RBCs to undergo deformation within a confined double-width channel. We will quantify the compression and dilation processes that occur when RBCs move through such channels, elucidating the mechanisms underlying this phenomenon. In addition, we will examine the dynamic response of RBCs to sudden changes in confining conditions caused by fluctuations in the geometry of the vessel within the channel environment. The focus of our investigation is the deformation index (DI), a quantitative measure that enables us to assess the extent of compression or dilation to which RBCs are subjected by confinement. Through careful analysis, we aim to unravel the complex interplay between channel geometry, applied pressure, and RBC deformability, shedding light on the fundamental mechanism governing the cells' response to mechanical forces. Furthermore, our inquiry extends to explore the influence of RBC age and membrane stiffness on the magnitude, rate, and duration of observed deformation. By dissecting these factors, we seek to elucidate how changes in cell properties influence RBC deformability within confining environments. Through comprehensive experiments and analyses, we strive to deepen our understanding of the dynamic interplay between cell aging, membrane properties, and deformation dynamics, providing valuable insights into the physiological adaptations of RBCs to microenvironmental cues. Investigating deformability is a fundamental means of understanding the complex interplay between the biological aspects of RBCs, their mechanical properties, and the physical forces they encounter. The main goal is to establish an experimental relationship between the applied stress (force) and the resulting cell stress (compression or stretch), measured in terms of deformation. To achieve this goal, a deformability measurement technique must meet two fundamental criteria:

- It must represent a quantifiable and well-defined factor capable of inducing a change in cell shape (which is DI in our case).
- The extent of deformation must be measurable either directly or indirectly (treating the data images of the cell flowing through the channel), with a high degree of sensitivity and reproducibility.

In conclusion, this chapter serves as a comprehensive exploration of the multifaceted nature of RBC deformation within confined channels, including the underlying mechanisms driving deformation and the modulatory effects of cell aging and membrane stiffness.

5.2 Materials and Methods

5.2.1 Blood Collection and Samples Preparation

Blood samples were meticulously collected from three healthy male volunteers, aged between 28 and 31 years, with full informed consent, into EDTA-containing tubes. Following collection, the samples underwent a centrifugation process at $3000 \times g$ for a duration of 5 minutes to effectively separate RBCs from plasma and other biological components. The sedimented RBCs were then subjected to a rigorous washing procedure involving three cycles with the PBS solution (see 2.1.1) to ensure the purity and integrity of the cellular samples for subsequent analyses (see Figure 2.1). All experimental procedures, encompassing blood withdrawal, sample preparation, and microfluidic experiments, strictly adhered to the ethical guidelines outlined in the Declaration of Helsinki and received approval from the ethics committee of the “Arztekammer des Saarlandes” (*permission number 51/18*). To delve into the age-based fractionation of RBCs, a meticulous Percoll density gradient centrifugation method, as detailed by Ermolinskiy et al.^[150], was employed (see Figure 2.2 for full protocol). The process involved layering two milliliters of washed RBCs with a hematocrit concentration of 50% in PBS ($\rho = 1.025 \text{ g/mL}$) atop five distinct layers of Percoll gradients with varying densities. Post-centrifugation, the extraction of four distinct layers (L1–L4) was executed with precision to prevent any cross-contamination, followed by a thorough washing of the fractionated RBCs with PBS. Concerning the artificial membrane rigidification, freshly washed RBCs underwent a treatment regimen with diamide (Sigma-Aldrich, Taufkirchen, Germany) at concentrations ranging from 0 mM to 2 mM (described in Figure 2.3), with diamide serving as a catalyst for cross-linking between spectrin proteins. Subsequently, samples representing RBCs sourced from whole blood (WB), age-separated (AS), and rigid categories were meticulously prepared with a hematocrit concentration of 1% in a PBS solution supplemented with 1 g/L bovine serum albumin (*BSA, Sigma-Aldrich, Taufkirchen, Germany*). The viscosity of resulting PBS/BSA solutions at 20°C mirrored that of human blood plasma, approximating 1.2 mPa.s. The meticulous averaging of data across the three donors, coupled with the absence of significant inter-individual variations, ensured the reliability and robustness of the results obtained.

5.2.2 Microfluidic Setup

In the investigation of RBC shape dynamics within flow conditions, rectangular microfluidic channels with precise double widths of $W_c = 7.8 \pm 0.2 \mu\text{m}$ and $W_e = 15.8 \pm 0.2 \mu\text{m}$ were meticulously employed (refer to Figure 2.6.B and Figure 5.2.A). The channel height was consistently maintained at $H = 5.2 \pm 0.2 \mu\text{m}$, with a total length of $l = 27 \text{ mm}$, strategically divided into $2 \times 9 \text{ mm}$ segments for W_e on the right and left sides, along with a central 9 mm segment for W_c . The fabrication process of the microfluidic device involved the utilization of polydimethylsilox-

ane (PDMS, RTV 615A/B, Momentive Performance Materials, Waterford, NY, USA) through standard soft lithography techniques, followed by precise bonding to a glass slide using a plasma cleaner (PDC32G, Harrick Plasma, Ithaca, NY, USA).

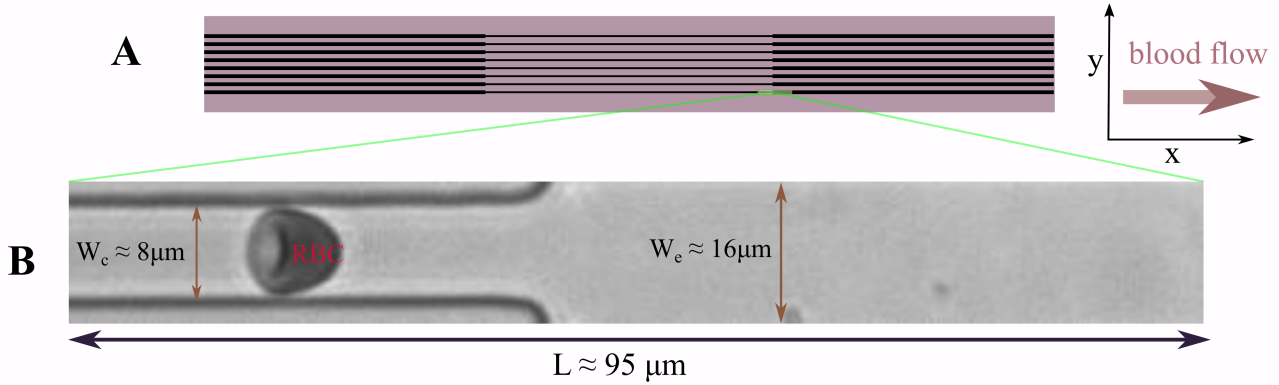


Figure 5.2: Illustration of the double width channel $W_c = 8 \mu\text{m}$ and $W_e = 16 \mu\text{m}$ used to process the compression-expansion of a single RBC: A- Set of double width channels with same height $H = 5 \mu\text{m}$ and length $l = 27 \text{ mm}$, divided into $2 \times 9 \text{ mm}$ segments for W_e on the right and left sides, along with a central 9 mm segment for W_c . B- Field of view ($\approx 95 \times 12 \mu\text{m}^2$) where the process of compression-expansion occurs.

The seamless connection of the inlet and outlet of the microfluidic chips with rigid medical-grade polyethylene tubing (featuring an inner diameter of 0.86 mm , *Scientific Commodities, Lake Havasu City, AZ, USA*) ensured optimal fluid flow to and from the sample and waste containers, respectively. The microfluidic chip was meticulously mounted on an inverted microscope (Eclipse TE2000-S, Nikon, Melville, NY, USA) equipped with advanced LED illumination (*SOLIS-415C, Thorlabs Inc., Newton, NJ, USA*). Utilizing a USB camera and a $20\times$ air objective, the RBC flow was precisely imaged at the strategic position of $2L/3$, precisely capturing the transition from the channel width W_c to W_e (as depicted in Figure 2.6.B.ii and Figure 5.2.B). The utilization of a high-precision pressure device (OB1-MK3, Elveflow, Paris, France) enabled the application of consistent pressure drops ranging from $p = 70$ to 200 mbar , ensuring controlled experimental conditions. Image sequences capturing the passage of each RBC through the field of view were recorded at a high frame rate of up to 400 frames per second, with a sophisticated tracking program managing the recording process. All microfluidic experiments were meticulously conducted at a controlled temperature of $22 \text{ }^\circ\text{C}$, ensuring the reliability and reproducibility of the experimental outcomes. The determination of essential parameters such as the center of mass and other key characteristics of each cell in the projection plane was facilitated by a custom MATLAB algorithm (*version 9.14.0.2206163 (R2023a), The MathWorks, Natick, MA, USA*). Individual cell velocities were precisely tracked across the image sequence within the field of view, providing valuable insights into the dynamic behavior of RBCs in the microfluidic environment.

5.2.3 Deformation Coefficient

In micro-confined settings, the shape of RBCs is intricately intertwined with the flow rate within the channel, showcasing a critical dependency on the environmental conditions. The calculation of the deformability index (DI) of RBCs during the compression-expansion flow process serves as a fundamental metric for evaluating alterations in cell deformability, providing crucial insights into the dynamic behavior of cells under varying flow conditions. The DI, as defined by Equation (5.2), with parameters a and b representing the major and minor axes of the RBC shape during flow, offers a quantitative measure within the range of -1 to 1, enabling a comprehensive assessment of the cell's response to compression and expansion forces exerted by the microfluidic environment.

$$\text{DI} = \frac{a - b}{a + b} \quad (5.2)$$

As RBCs navigate through highly confined channels, the DI assumes positive values, indicative of the cell's elongation in response to the compression imposed by the channel boundaries. This elongation phenomenon, characterized by a decrease in the minor axis (b) and an increase in the major axis (a), underscores the adaptive nature of RBCs in aligning with the direction of flow. Conversely, negative DI values signify expansion resulting from reduced confined areas, accompanied by sudden changes in cell acceleration and alterations in the cross-sectional profile.

5.2.4 Fit Model

The sigmoid function, a fundamental mathematical tool, serves to map its input to a value within the range of 0 to 1, showcasing its versatility and widespread application in fields such as machine learning, statistics, and neural networks. Its adaptability and unique properties make it a valuable asset in diverse applications, offering a robust framework for modeling complex systems. The customized sigmoid function $f(t)$ tailored for our specific context is delineated in Equation (5.3), where A represents the asymptotic value of $f(t)$ as t approaches negative infinity, B denotes the gap-value integrated across the entire time domain, and τ signifies the characteristic time governing the transition between the function's asymptotes (from A to $A - B$), thereby influencing the temporal dynamics of the system described by $f(t)$.

$$f(t) = A - B \frac{1}{1 + e^{-\frac{t}{\tau}}} \quad (5.3)$$

The derivation of the formula ($\frac{\partial f(t)}{\partial t}$), representing the partial time derivative of $f(t)$ as illustrated in Equation (5.4), sheds light on the intricate transitions from a concave downward to a concave upward trajectory within the function. This analytical approach enables a deeper understanding of the function's behavior and dynamics, elucidating critical inflection points and

rate changes. Notably, the determination of the maximum value at the inflection point (i.e., the slope of $f(t)$) occurring at $t = 0$ yields a resultant value of $-\frac{B}{4\tau}$, signifying the sharpest rate of change within the function. This value is intricately linked to the time constant τ , dictating the steepness and curvature of the curve, thereby influencing the overall shape and behavior of the sigmoid function.

$$\frac{\partial f(t)}{\partial t} = -\frac{Be^{-\frac{t}{\tau}}}{\tau(1 + e^{-\frac{t}{\tau}})^2} \quad (5.4)$$

5.3 Results

5.3.1 Deformation Illustration

In our investigation conducted through a double-width channel with $W_c = 8 \mu\text{m}$ and $W_e = 16 \mu\text{m}$, the behavior of a single RBC extracted from whole untreated blood (WB) under a pressure of $p=70\text{mbar}$ was observed (see Figure 5.3.A). It was noted that the cell retained its original shape both prior to and subsequent to passing through the exit situated between W_c and W_e , where deformation was observed.

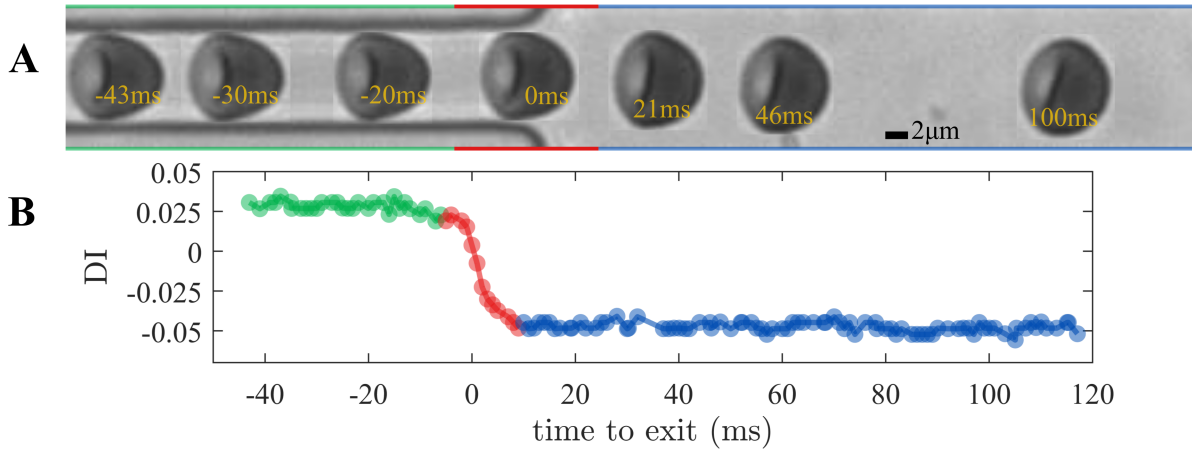


Figure 5.3: Single RBC extracted from whole blood flowing through the compression-expansion channel under the pressure drop of 70 mbar: A- Snapshots of the single RBC at different time steps to show the evolution of its shape during the compression-expansion process. B- Time evolution of DI shows the change from compressed ($a > b$) to negative values ($a < b$). The stage areas where the cell maintains its shape (greenish area for compression at the channel width $\approx 8 \mu\text{m}$ and blueish area for expansion at $\approx 16 \mu\text{m}$), while the transition area is represented in the reddish stage.

Illustrated in Figure 5.3.B, the entire temporal progression of the deformation index $DI(t)$ unfolds across three distinct stages: Initially, at the channel width W_c (referred to as the green stage), the cell experiences compression owing to the constraints imposed by the channel. Here, the horizontal dimension (a , described as the length of the RBC along x -axis) surpasses the vertical length (b , described as the length of the RBC along y -axis), resulting in a high deformation index (DI) during this phase. As the cell approaches the exit region (termed the

red stage), signs of deformation become evident, characterized by an expansion denoted by a reduction in 'a' and an increase in 'b'. Over time, this deformation progresses to attain a lower value, which persists within the width W_e (termed the blue stage). The overarching findings of the experiment underscore that RBCs sourced from WB maintain their structural integrity before and after traversing the exit between W_c and W_e . This substantiates the notion that deformation solely arises from the compression-expansion dynamics, with no intrinsic alteration in cell morphology occurring.

5.3.2 Deformation Distributions

The key focus of our investigation was the deformation index, referred to as $DI(t)$, which played a crucial role in characterizing how RBCs behave within the double width channel. We found a consistent pattern in the morphological characteristics displayed by RBCs across different channel widths, sparking our interest in analysing the deformation index as a step function with distinct values, DI_8 and DI_{16} , corresponding to specific channel widths, W_c and W_e . To enhance our understanding of RBC deformability, we introduced a new metric, ΔDI , to quantify the difference between DI_8 and DI_{16} . This innovative approach allowed us to quantitatively evaluate the extent of RBC deformation as they moved through channels of varying widths, providing valuable insights into the mechanisms influencing RBC behavior in microchannels.

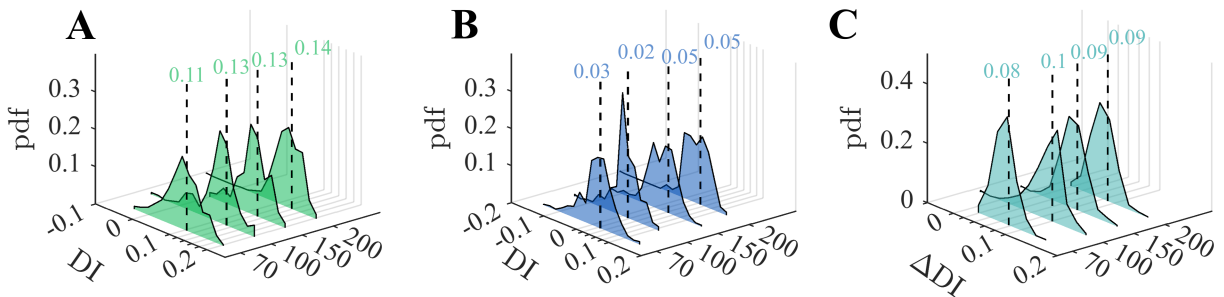


Figure 5.4: Distributions of the deformation index (DI) values following the pressure at both compression-expansion stages within the channel widths presented in Figure 5.3: Probability density functions (PDFs) of the median values of $DI(t)$ of RBCs that compress (A) while flowing through the channel width $\approx 8 \mu\text{m}$ then expand (B) through the channel width $\approx 16 \mu\text{m}$ at each pressure drop. ΔDI presents the individual difference between median DI values at both stages (see Figure 5.3.B). PDFs (C) shows no effect of pressure drop on the amount of RBC deformation. All median (dash-lines) distribution values are presented at the top of each PDF.

Our analysis, involving a significant sample size of 1363 individual RBCs, provided valuable insights into the probabilistic distribution of DI_8 , DI_{16} , and ΔDI . Visualized in Figure 5.5, these distributions revealed intriguing patterns, shedding light on the complex relationship between RBC behavior and channel geometry. When subjecting RBCs to different pressure conditions within the channel, interesting observations emerged. In the narrower channel section W_c , RBCs experienced significant compression, as indicated by DI_8 values ranging from 0 to 0.22 (see Figure 5.5.A). Conversely, as RBCs moved into the wider channel region W_e , the median values

of DI_{16} showed a noticeable decrease, highlighting the impact of confinement-induced expansion forces. This shift was evident in DI_{16} values ranging from -0.12 to 0.16 (see Figure 5.5.B), emphasizing the interplay between channel width and RBC deformability. Additionally, our investigation examined the distribution of deformation differentials, ΔDI , revealing a diverse range of values from 0.02 to 0.18 (see Figure 5.5.C). These variations underscored the complex response of RBCs to changes in pressure gradients within the channel environment, providing further insights into the behavior of these vital blood components.

5.3.3 Effect of Age and Rigidity on Deformability

The variation in the age of RBCs from whole untreated blood (WB) spans a wide range, significantly impacting the overall results observed in the preceding section. To delve deeper into this phenomenon, our next investigation focuses on segregating RBCs into layers of varying densities to explore the influence of aging on their properties. Additionally, we delve into examining how different degrees of membrane rigidity in RBCs from WB affect their deformation within the double-width channel.

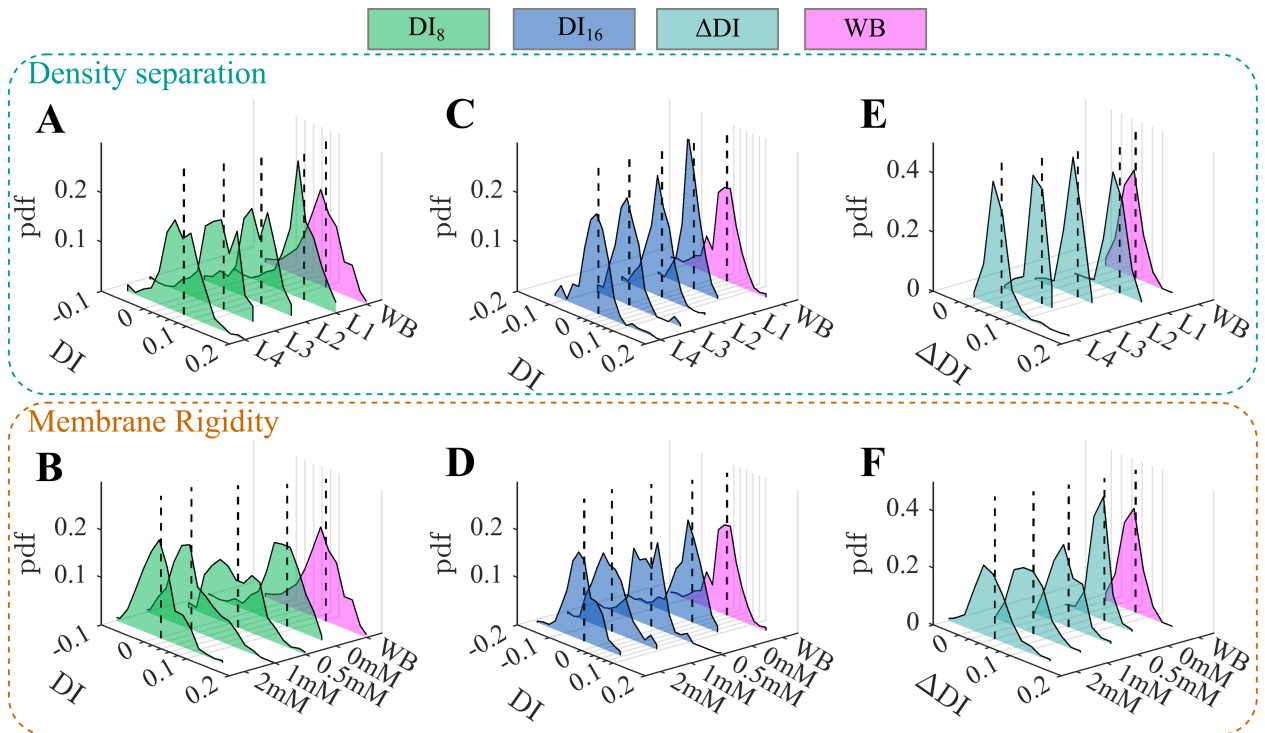


Figure 5.5: Effect of age (top) and membrane rigidity (bottom) on DI distributions of RBCs extracted from each density separation layers (see Figure 4.3) and from the diamide solutions (see Figure 2.3) at $p = 70$ mbar: Distributions as probability density functions (PDF) of the deformation index (DI) within channel widths $\approx 8 \mu\text{m}$ (A-B), $\approx 16 \mu\text{m}$ (C-D) and the individual amount of deformation (E-F) between the compression-expansion process through the exit $(\Delta DI)_i = (DI_8)_i - (DI_{16})_i$. The pink PDFs present the DI values of RBC collected from whole blood (see Figure 5.4). The dashed lines presents the median values of each PDF.

Upon analyzing the RBCs from WB, it was noted that the application of pressure drop

had minimal effects on the probability density functions (pdfs) and mean values of DI_8 , DI_{16} , or ΔDI . To gain further insights, we decided to analyze the data based on age and rigidity, particularly focusing on comparing the pdfs at a pressure of $p = 70$ mbar. This pressure setting allowed for the collection of a substantial amount of data as the RBCs flowed slowly, providing a more detailed analysis. The results from the density-separated RBCs revealed an interesting trend, with a more rapid decrease in DI_8 compared to DI_{16} as the age of the RBCs increased (e.g., L1-L4 layers). This differential rate of decrease directly impacted ΔDI , indicating that the deformability of RBCs is intricately linked to their age. On the other hand, as the rigidity of RBCs increased, they exhibited a tendency to become stiffer, leading to compression (e.g., DI_8 and DI_{16} shifting closer to zero and negative values, respectively, compared to WB).

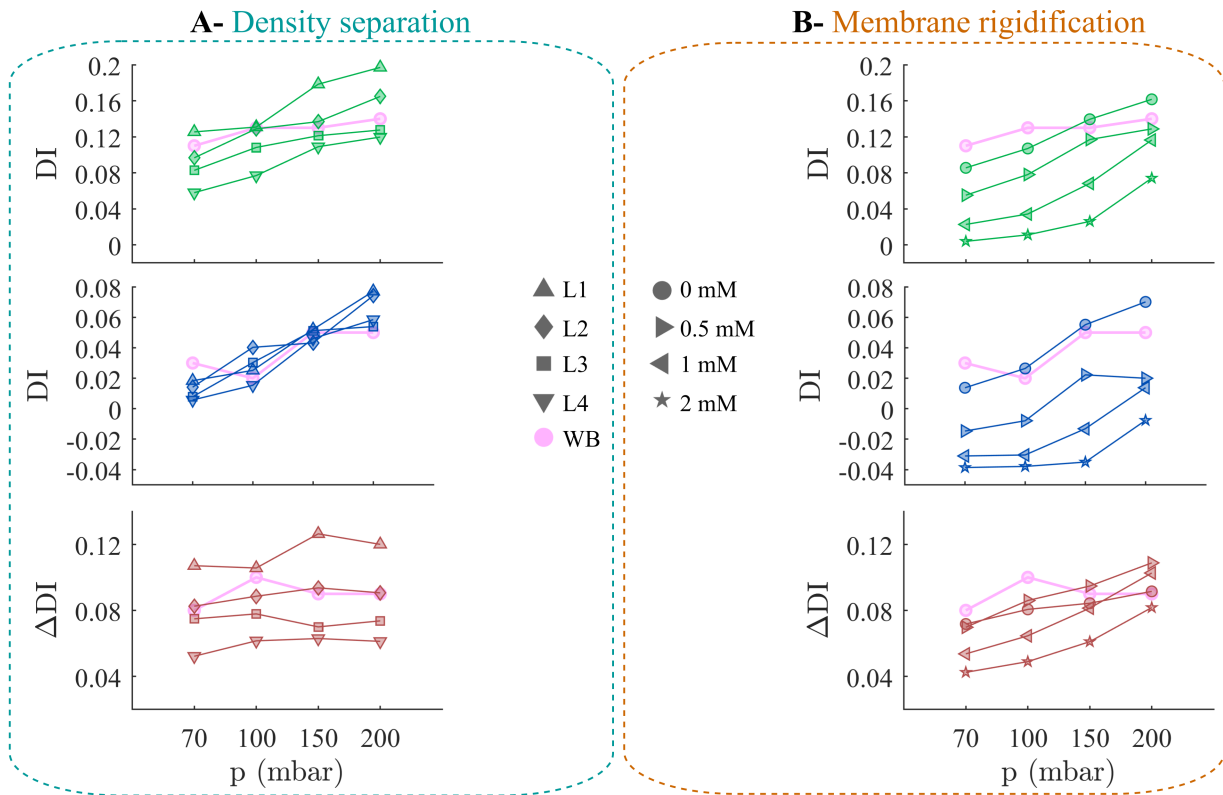


Figure 5.6: Comparison between deformation of RBCs extracted from whole blood (WB), density separation (A) and membrane rigidification (B). Based on the median values of DI distributions in Figure 5.5) but for the complete range of pressure drop, their evolution at (top) channel width of $\approx 8 \mu\text{m}$ and at (middle) channel width of $\approx 16 \mu\text{m}$ as a function of the pressure. In addition, (bottom) the individual change on the deformation ΔDI . The total number of RBCs treated is about: 1363 for WB. 880, 1078, 1045 and 1011 for L1–L4 respectively. 1130, 1120, 787 and 1344 for 0 – 2 mM respectively.

The pdfs of both DI_8 and DI_{16} decreased at a faster rate with increasing rigidity, while the range of values for ΔDI decreased, signifying a shift towards more constrained deformations (e.g., maximum pdf values decreasing with rigidity). Notably, the results from the L2 and 0mM layers aligned with the findings from WB. The rigidity of young, fresh RBCs (L1) is relatively low, allowing for easy compression within confined channels. However, as RBCs age, they pro-

gressively lose flexibility, resulting in reduced deformation capabilities. The membrane stiffness or rigidity of RBCs plays a crucial role in altering the overall deformation characteristics of the cell, highlighting the intricate relationship between cell properties and deformability. With the intention of to facilitate a comprehensive and insightful comparison of the deformation characteristics exhibited by WB, age-separated, and RBCs with varying levels of membrane rigidity, Figure 5.6 meticulously presents the median values of DI_8 , DI_{16} , and ΔDI across a diverse range of pressures spanning from 70 to 200 mbar. These results, also elegantly depicted as dashed lines in Figure 5.5 specifically for a pressure of $p = 70$ mbar, offer a profound glimpse into the intricate behavior of RBCs under varying pressure conditions. The detailed analysis unravels a compelling trend wherein the compression level of DI_8 showcases a notable increase in response to the applied pressure (see top Figure 5.6.A) for density-separated RBCs. Notably, RBCs originating from the L1 layer emerge as the most highly compressed cells within the W_c region, exhibiting a range of compression values from 0.13 to 0.2. This compression gradient gradually diminishes with the aging of the cells, culminating in the L4 layer displaying the narrowest range of DI_8 values, oscillating between 0.05 and 0.12. It is worth highlighting the remarkable alignment observed between the results from the L2 layer and those derived from WB, underscoring the significance of these findings. As these density-separated RBCs progress through the channel, a discernible decrease in compressibility is observed at the W_e region (see middle Figure 5.6.A), mirroring the trends observed within the WB samples. In stark contrast, the deformation characteristics of age-separated RBCs, as encapsulated by ΔDI , appear to exhibit a remarkable independence from the pressure variations exerted on the channel (see bottom Figure 5.6.A). The median values of ΔDI exhibit a consistent decrease across the L1-L4 layers, underscoring the nuanced relationship between RBC age and deformability. Conversely, the results pertaining to rigid RBCs shed light on a distinct pattern, showcasing a consistent increase in compression levels with the applied pressure for density-separated cells. Notably, RBCs subjected to rigidification at 0mM of diamide demonstrate the highest levels of compression within the W_c region (see top Figure 5.6.B), ranging from 0.09 to 0.16, aligning seamlessly with the trends observed in the WB samples. As the membrane rigidity intensifies, the compression levels gradually decrease, culminating in a minimal range of DI_8 values for RBCs rigidified at 2 mM of diamide. Furthermore, as the rigid RBCs traverse through the channel, a notable reduction in compressibility is observed at the W_e region (see middle Figure 5.6.B), with compression values reaching negative ranges at higher levels of rigidification. This distinctive behavior of rigid RBCs, characterized by maintaining compression in the direction of confinement before undergoing deformation at the exit, underscores the intricate interplay between membrane rigidity and deformability. The deformation levels of rigid RBCs, as encapsulated by ΔDI , exhibit a clear relationship with pressure (see bottom Figure 5.6.B), showcasing a linear increase for lower diamide densities and an exponential increase for higher

densities. The results presented encapsulate the profound impact of membrane rigidity in conjunction with cell density on the deformability of RBCs during a compression-expansion process. Young RBCs exhibit a remarkable flexibility that enables them to deform effortlessly through narrow channels. However, as these cells age, they gradually lose this inherent flexibility and transition towards a stiffer state. Moreover, the rigidity of the RBC membrane from WB plays a pivotal role in facilitating the smooth flow of cells through narrow channels. Nevertheless, this fluidity is compromised with an increase in rigidity, leading to a scenario where the cell undergoes compression in a direction opposite to that of the confinement.

5.3.4 Deformation Rate and Deformation Time

A comprehensive and detailed investigation was meticulously conducted near the exit within the double-width channel, focusing on the intricate compression-expansion process to precisely measure the deformation rate (DR) of RBCs as they traverse through.

The primary aim of this study was to unveil the nuanced alterations in both age (L1-L4) and membrane rigidity (0mM-2mM diamide concentrations), not only in terms of the deformation amount (ΔDI) as discussed in the preceding section but also in the characteristic rate DR and the duration of deformation (τ_R). This temporal aspect, defined as the time the cell spends undergoing deformation in close proximity to the exit, provides crucial insights into the dynamic behavior of RBCs under varying conditions.

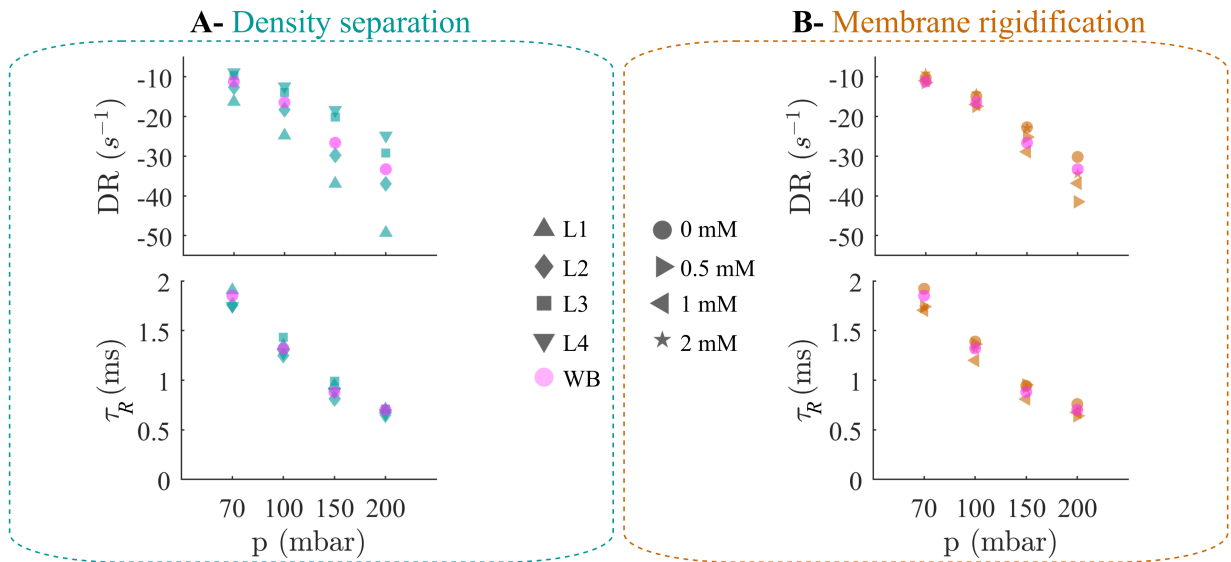


Figure 5.7: Analysis and results of the deformation speed (DR) defined as the slope of the deformation index $DI(t)$ in time at the exit, noted $\partial DI / \partial t|_{t=0}$ and the deformation time (τ_R) of RBCs under diverse conditions: The top row showcases the evolution of DR at the exit of the double-width channel. The bottom row depicted the deformation time characteristic τ_R at each pressure drop across WB (pink data points), density-separated (A) and rigid (B) RBCs.

To achieve a comprehensive understanding of the deformation dynamics, a specialized function was employed (see Equation (5.3)) to fit the curve data $DI(t)$ collected near the exit,

capturing the critical moments before and after $t=0$, which signifies the instant when the cell reaches the exit. The utilization of the sigmoid function $f(t)$ emerged as the most suitable model, where $f(t \rightarrow -\infty) = DI_8$, $f(t \rightarrow +\infty) = DI_{16}$ and $B = \Delta DI$, showcasing a remarkable fit with R^2 values approaching unity post-analysis. This sophisticated model enabled the extraction of essential parameters such as $DR = -\Delta DI/4\tau$ deformation time τ_R , and various deformation values including DI_8 , DI_{16} , and ΔDI . The subsequent analysis and treatment of the data yielded a wealth of valuable results, meticulously illustrated in Figure 5.7 for each category of RBCs, encompassing WB, age separation, and rigid classifications. Noteworthy observations from the analysis revealed a compelling trend where DI_8 consistently exceeded DI_{16} for the majority of RBCs, leading to a negative evolution of the deformation rate at the exit, ranging from -10 to -50, as depicted in the top row of Figure 5.7. In contrast, the deformation time τ_R exhibited fluctuations within a range of 0-2 milliseconds, as elegantly portrayed in the bottom row of Figure 5.7. Delving deeper into the results from age-separated RBCs (Figure 5.7.A), a distinct pattern emerged where the absolute value of DR showcased a discernible decrease with increasing pressure, with this rate of decrease further diminishing as the cell aged. For instance, younger RBCs in the L1 category displayed a decrease from -9 to -23, while older L4 cells exhibited a more pronounced decrease from -16 to -48, maintaining a consistent trend akin to the WB-extracted cells as observed in L2. Similarly, the results obtained from rigidified RBCs (Figure 5.7.B) unveiled a parallel decrease in the absolute value of DR with increasing pressure, albeit with varying rates of decrease ranging from 0 at 70mbar to 15 at 200mbar, exemplified by the decrease from -10 to -40 for 0.5mM rigidification. Furthermore, the deformation time τ_R for all categories of RBCs remained relatively stable at each pressure drop, with a consistent duration of 2ms at 70mbar gradually decreasing to 0.7 ms. The exponential decrement of τ_R following pressure variations remained unaffected by either age or membrane rigidity, underscoring the robustness and reliability of the results obtained. These insightful findings collectively highlight the intricate relationship between pressure, age, and membrane rigidity in shaping the deformability and behavior of RBCs within the complex microchannel environment. The dynamic nature of cellular deformation, as evidenced by the varying rates of DR and τ_R , underscores the importance of considering multiple factors in understanding the mechanical responses of RBCs under different conditions.

5.3.5 Relaxation Effect

Following the exit from a confined space, such as a microcapillary, RBCs undergo a deformation process triggered by the sudden change in confinement. This compression phase persists until the cell reaches a specific minimum value of the deformation index (DI), at which point the cell's shape rebounds, displaying elastic behavior, and the DI value begins to ascend until it stabilizes at a fixed plateau value. The Figure 5.8 illustrates the temporal evolution of the

deformation index (DI) for a single RBC from L1, showcasing the relaxation phenomenon through red data points conforming to an exponential function, visually represented by the green line. Simultaneously, the cell maintains its flow while gradually returning to its stable shape, characterized by a consistent DI value, as indicated by the blue data points.

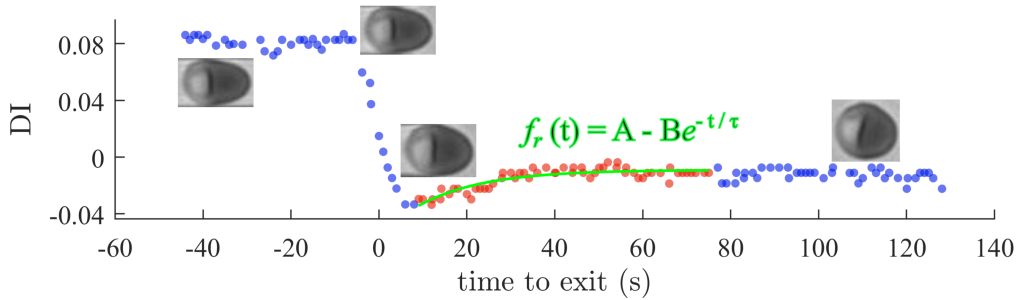


Figure 5.8: Relaxation phenomena observed as a reaction to the expansion process after RBC exiting the confined area. The red data points present the DI values along the time of relaxation, which are fitted with the exponential function f_r , where A is the deformation of the cell at infinite time (approximately reaching the blue data points with higher positive time), B is relaxation characteristic coefficient of RBC (e.i. the amount of DI retrieved during the relaxation), and τ is the relaxation characteristic time. The frames of a RBC extracted from L2 at $p = 70$ mbar is showing the shape at each interval of the compression-expansion process.

Our research is dedicated to unraveling the intricate evolution of this deformation process concerning established RBC properties. Despite the exponential nature of shape relaxation over time, crucial parameters such as the amplitude and duration of relaxation can be discerned and meticulously analyzed. The relaxation behavior exhibited by RBCs serves as a valuable tool for both quantitatively and qualitatively assessing the physiological status of the cell. By extracting characteristic parameters from the fitted data, a comprehensive insight into the RBC's condition can be obtained, providing a deeper understanding of its overall state and functionality.

The observation of the relaxation phenomenon during the compression and expansion process varies among cells, with not all cells exhibiting this behavior. The Figure 5.9 provides insights into the fractions of cells manifesting relaxation phenomena across different ages and membrane rigidities of RBCs. It is evident from the data that the relaxation phenomenon is more pronounced in younger cells, with an occurrence rate of approximately 50-55% for L1 and L2 cells, gradually diminishing to less than 20% as cells age (see the top line in Figure 5.9). In contrast, rigid cells exhibit minimal relaxation, with occurrences ranging between 2-7%.

The amplitude of relaxation (B) reaches its peak value of 0.031 for RBCs from L1, attributed to their high deformation rate as illustrated in Figure 5.7. As cell deformability decreases with age, the amplitude of relaxation (B) also decreases to 0.02 for L2, 0.015 for L3, and 0.016 for L4. Conversely, for rigid cells, the amplitude of relaxation (B) fluctuates within the range of 0.02-0.025 across different diamide concentrations. The higher error bars observed in the membrane rigidity results are due to the limited statistical efficiency resulting from a low number of cells.

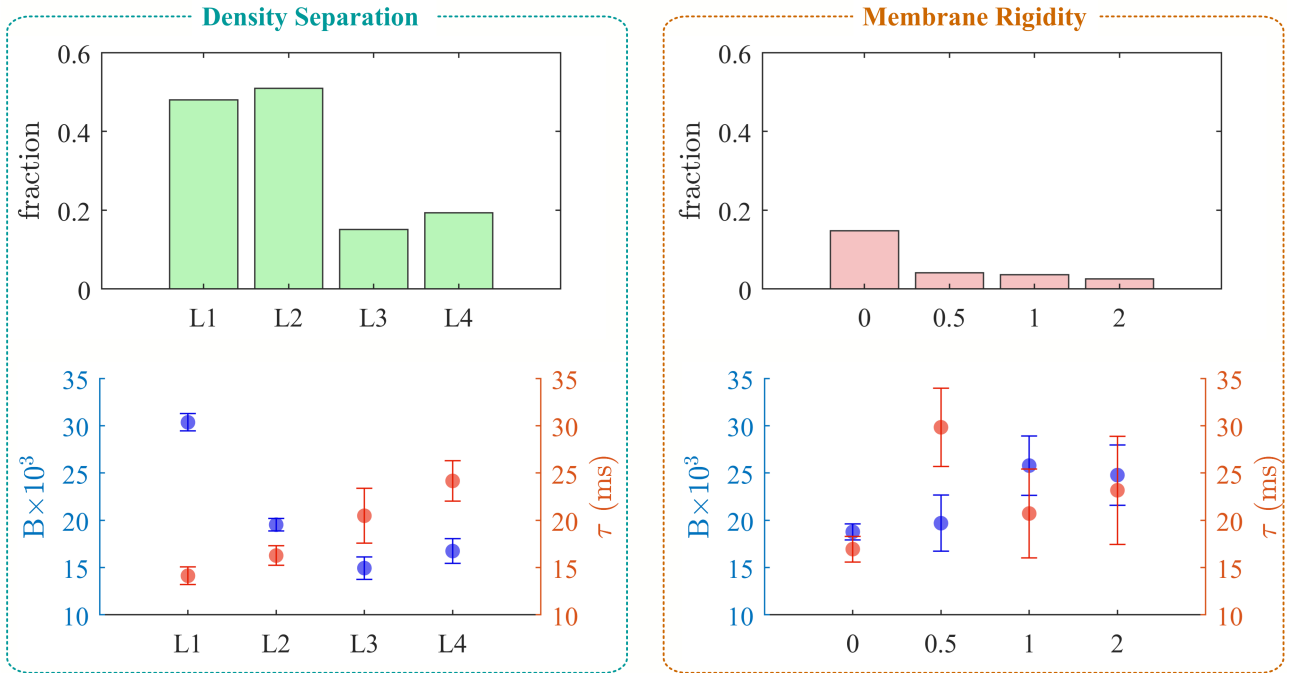


Figure 5.9: The occupancy and variation of the relaxation phenomena at low pressure $p = 70$ mbar for both effects, age and membrane rigidity of the cell. Top line: The fractions of cells that show the relaxation phenomena for both effects. Bottom line: The evolutions of the median of B and τ , together with their error bars, for the amount of cells at each layer (left) and each diamide concentration on mM (right).

Another critical aspect of the relaxation phenomenon is the relaxation time (τ), where density separation results indicate that young RBCs from L1 exhibit the shortest relaxation time of 14 ms, which gradually increases with cell age to approximately $\tau = 25$ ms for older RBCs from L4. In contrast, rigid cells do not demonstrate a clear dependency of relaxation time on membrane rigidity, with τ fluctuating between 30 ms for 0.5 mM diamide concentration and 21 ms for 1 mM.

The alignment of results from L2 and 0 mM is noteworthy, as RBCs from both categories exhibit similar physiological characteristics. L2 represents a denser layer containing the majority of RBCs in blood, while 0 mM denotes RBCs that have been incubated in PBS solution for 30 minutes.

5.4 Discussion

In this study, we investigate the deformability characteristics exhibited by individual RBCs as they traverse a channel with two different confinement coefficient values. Our analysis focuses on quantifying the extent of deformation induced by the abrupt alterations in channel dimensions, leading to a compression-expansion phenomenon in the cellular morphology. The degree of compression experienced by the RBCs correlates positively with the pressure exerted across the widened channel, mirroring previous observations^[161], under analogous flow conditions for

RBCs extracted from whole blood (WB). Notably, the rate of compression relative to velocity diminishes by half as the cell transitions into the broader channel. Deformability, herein defined as the alteration in deformation throughout this process, is delineated as the disparity in compression levels between the two channel widths. Subsequent to these distinct phases, as the cell nears the channel exit, we ascertain two key deformability attributes: firstly, RBCs sourced from WB exhibit a linear augmentation in deformation rate (DR) commensurate with escalating shear rates. Secondly, the time required for cell deformation follows a decaying trend in response to shear rate variations. Moreover, we elucidate the influence of RBC age, discerned through density-based separation, on deformability dynamics. Under constant pressure conditions, both compression magnitude and rate diminish with increasing cell age, indicative of heightened intracellular viscosity^[200] attributable to elevated cell density. Concurrently, DR demonstrates a linear progression akin to that observed in WB-derived cells, albeit with a declining slope correlating with cell age. Furthermore, we employ varying concentrations of diamide to simulate membrane disorders affecting RBC deformability, encompassing conditions such as diabetes^[272], hereditary membrane anomalies (including spherocytosis, elliptocytosis, ovalocytosis, and stomatocytosis)^[24,273], hypercholesterolemia^[273], paroxysmal nocturnal hemoglobinuria^[274], malaria^[275], and sickle cell anemia^[276]. Our findings unveil a broader spectrum of compression, expansion, and deformability metrics, showcasing an exponential augmentation in deformability with shear rate, reminiscent of behaviors observed in ektacytometry assessments. Notably, DR remains relatively unchanged irrespective of membrane rigidity as shear rate escalates.

The results obtained from the study of the relaxation phenomenon add more valuable findings to understand what happened during the process of RBC deformation following their exit from confined spaces, such as microcapillaries. The deformation process is characterized by a compression phase triggered by the sudden change in confinement, leading to a decrease in DI until a specific minimum value is reached. Subsequently, the RBC undergoes a rebound, displaying elastic behavior as the DI value ascends and stabilizes at a plateau. The temporal evolution of the DI for a single RBC from layer L1 illustrates the relaxation phenomenon, with the cell gradually returning to its stable shape while maintaining flow. This phenomenon, although exponential in nature, provides valuable insights into the physiological status of the cell, allowing for quantitative and qualitative assessments of its condition. The observation that not all cells exhibit the relaxation phenomenon highlights the heterogeneity in RBC behavior. Younger cells, particularly those from layers L1 and L2, demonstrate a higher occurrence of relaxation, which diminishes as cells age. In contrast, rigid cells exhibit minimal relaxation, indicating a correlation between cell deformability and the relaxation process. The amplitude of relaxation (B) peaks for RBCs from L1, reflecting their high deformation rate, and decreases with age. Additionally, the relaxation time (τ) varies across different cell ages, with younger cells exhibit-

ing shorter relaxation times compared to older cells. The alignment of results between layer L2 and 0 mM underscores the similarity in physiological characteristics between these groups, despite their distinct compositions.

These findings resonate with previous studies that have explored RBC deformability and relaxation phenomena^[19], delves into the mechanical properties of RBCs, emphasizing the importance of understanding cell deformability in physiological contexts. Furthermore, the work of Tomaiuolo et al.^[11] investigates the dynamics of RBC deformation in microcapillaries, highlighting the role of cell age and membrane rigidity in shaping cell behavior. The observations regarding relaxation time align with studies which emphasize the impact of cell age on the viscoelastic properties of RBCs^[191]. Overall, the results presented in the study provide valuable insights into the complex interplay between RBC age, membrane rigidity, and the relaxation phenomenon following cell deformation. By elucidating the characteristics of RBC behavior in response to varying conditions, these findings contribute to a deeper understanding of the physiological dynamics of RBCs in microfluidic environments.

5.5 Conclusion

In conclusion, the comprehensive analysis of the compression-expansion process for RBCs extracted from various blood media, including whole blood, density-separated samples, and those subjected to membrane rigidification, as they traverse channels with differing confinement values, has yielded valuable insights into the behavior of RBCs in dynamic flow environments. The findings indicate a positive correlation between the degree of compression experienced by RBCs and the pressure exerted across widened channels. Moreover, the rate of compression relative to velocity demonstrates a notable decrease by half as the cells transition into broader channels, underscoring the influence of channel geometry on RBC deformation dynamics. Cells sourced from whole blood exhibit a linear increase in deformation rate (DR) corresponding to escalating shear rates, while both compression magnitude and deformation rate decrease with advancing cell age. Interestingly, the deformation rate remains relatively consistent regardless of membrane rigidity as shear rate increases, emphasizing the complex interplay between cell age, shear rates, and deformability. The subsequent rebound of RBCs, displaying elastic behavior as the deformation index (DI) stabilizes at a plateau, signifies the resilience of RBCs in response to compression and expansion processes. The observation that not all RBCs exhibit the relaxation phenomenon underscores the inherent heterogeneity in RBC behavior. Younger cells, particularly those from layers L1 and L2, display a higher propensity for relaxation, which diminishes with cell age. In contrast, rigid cells exhibit minimal relaxation, highlighting the impact of cell deformability on the relaxation process.

These findings provide valuable insights into the nuanced dynamics of RBC behavior in microfluidic environments, offering a deeper understanding of the physiological responses of

RBCs to varying conditions. By elucidating the complexities of RBC deformation, compression, and relaxation processes, this study contributes to advancing our knowledge of RBC behavior in dynamic flow settings and underscores the importance of considering factors such as cell age, membrane rigidity, and shear rates in understanding RBC dynamics in microfluidic systems.

This thesis presents a comprehensive investigation into the morphodynamic behavior of red blood cells (RBCs) under various microfluidic conditions, offering crucial insights into their deformability and flow characteristics. The research is structured into three interconnected phases, each contributing to our understanding of RBC behavior in confined environments.

6.1 Summary of Key Findings

6.1.1 Influence of Geometrical Structure on RBC Morphology

Our investigation into the impact of channel geometry on RBC shape adaptation revealed several critical insights that expand our understanding of RBC behavior in confined microfluidic environments. We systematically explored the effects of channel dimensions, confinement ratios, and flow velocities on RBC morphology and positioning. In strongly confined rectangular channels with a height below $10\ \mu\text{m}$ and a confinement ratio ($\chi = D_{\text{RBC}}/D_h$) exceeding 0.9, we observed the emergence of distinct RBC shapes, characterized by croissant-peaks at low velocities and slipper-plateaus at high velocities. Specifically, in the most confined channel ($W \approx 10\ \mu\text{m} \times H \approx 8\ \mu\text{m}$), the croissant fraction reached a peak value of approximately 50% at a velocity of $1\ \text{mm}, \text{s}^{-1}$, while the slipper fraction increased above $3\ \text{mm}, \text{s}^{-1}$, eventually plateauing at 70-75% above $5\ \text{mm}, \text{s}^{-1}$. These findings are consistent with previous studies of RBC flow in similarly confined channels^[159,163]. Interestingly, increasing the channel height to $10\ \mu\text{m}$ resulted in a higher fraction of croissants while suppressing slipper-shaped RBCs. However, further increasing the height to $15\ \mu\text{m}$ led to a decrease in the croissant fraction, with most RBCs displaying other shape types. This observation highlights the complex interplay between channel dimensions and RBC morphology, which aligns with numerical simulations predicting shape transitions based on channel size^[188,189]. Our findings emphasize that an oval rectangular cross-section coupled with a shallow channel ($H \leq 10\ \mu\text{m}$) is a prerequisite for the emergence of slippers. Even a modest increase in channel height by $2\ \mu\text{m}$ to $H = 10\ \mu\text{m}$ resulted in a significant reduction of the slipper fraction. Consequently, stable slipper-like shapes are pri-

marily found in strongly confined, rectangular channels with a height smaller than $10\ \mu\text{m}$ and a confinement ratio exceeding $\chi = 0.9$. This is in contrast to observations in round capillaries, where slippers are essentially absent at $\chi > 0.7$ due to the cylindrical channel geometry^[19,70]. The RBC shape is intrinsically linked to its equilibrium position in the microchannel. Our analysis of the cell's y -position distribution aligned with the observed phase diagrams. When a significant number of slipper-shaped RBCs was observed, a pronounced off-centered peak at $|y/W| \approx 0.22$ appeared in the probability density distributions. This observation is in good agreement with previous work^[160,193]. We also studied how the shape of stable croissant and slipper-like RBCs is affected by the flow conditions in different microchannels. We found that the elongation index (DI) of both shapes increased with the channel shear rate. Croissants transitioned from negative to positive DI values as shear rates increased, while slippers maintained positive DI values throughout. At low shear rates, croissant-shaped RBCs exhibited a broad shape with a shorter length in flow direction than across the channel width ($DI < 0$). As the shear rate increased up to $5 \times 10^3\ \text{s}^{-1}$, there was a substantial rise in the elongation index, independent of the channel cross-section. Beyond $8 \times 10^3\ \text{s}^{-1}$, cell elongation seemed to saturate, eventually reaching a plateau at $DI = 0.1$. This dynamic deformation behavior is consistent with previous investigations on single RBCs^[137,277]. Our study also revealed the presence of unstable RBC shapes, particularly in less confined channels with $\chi \leq 0.65$. These unstable shapes exhibited rich temporal dynamics and strong fluctuations in their center of mass position during flow. The fraction of unstable other shapes was larger in microfluidic channels with a large cross-section (10×15 , 15×10 , and $15 \times 15\ \mu\text{m}^2$). This observation aligns with numerical simulations predicting a transition from steady to dynamic shapes upon increasing channel dimensions^[73,81].

6.1.2 Impact of Density and Membrane Rigidity on RBC Behavior

Through the investigation into the effects of cell density and membrane rigidity on RBC behavior in microfluidic channels revealed significant insights into the complex interplay between cellular properties and flow dynamics. By fractionating cells based on age and chemically modifying membrane properties, we uncovered several key findings that expand our understanding of RBC morphodynamics in confined environments. We observed a progressive decrease in the formation of stable, asymmetric slipper-like cells at high velocities as RBCs age or undergo membrane stiffening. For density-fractionated cells, the number of croissant-shaped RBCs increased with increasing age. The peak value of the croissant fraction rose from approximately 25% for the youngest fraction (L1) to 75% for the oldest fraction (L4), while the corresponding velocity of the croissant peak remained consistent at about $1\ \text{mm}\cdot\text{s}^{-1}$. This finding aligns with previous studies on RBC shape transitions in microchannels^[74,75]. Interestingly, croissant-like shapes also appeared at velocities exceeding $5\ \text{mm}\cdot\text{s}^{-1}$ for L3 and L4, whereas no significant

numbers of such shapes were found at the same velocities for L1 and L2.

Concurrently, the proportion of slipper-like shapes decreased with increasing age between the layers. While a plateau value for the slipper fraction of roughly 80% was observed for velocities above 6 mm.s^{-1} in L1 and L2, this value decreased sharply below 20% for L4. This trend is consistent with previous observations of age-dependent changes in RBC deformability [54,134,136,255].

The artificial rigidification of the membrane with diamide treatment significantly affected the formation of stable croissant and slipper-like shapes. While the control (0 mM diamide) exhibited the characteristic croissant peak at approximately 1 mm.s^{-1} , increasing the diamide concentration led to a reduction in the peak fraction and a shift of the peak position toward higher velocities of about 3 mm.s^{-1} for a concentration of 2 mM. This shift in shape transition velocities due to increased membrane rigidity is in agreement with theoretical predictions. We examined the projection area and deformability index (DI) of RBCs during capillary flow. With increasing age (L1–L4), the median projection area decreased at both low and high velocities, while it increased with increasing diamide concentration. The deformability index (DI) showed interesting trends: for both age-fractionated RBCs and cells treated with diamide, the median DI at high velocities was larger than at low velocities, attributed to the emergence of slipper-like shapes at elevated velocities leading to cell elongation. This observation is consistent with previous studies on RBC elongation in microchannels. The RBC shape was inherently linked to its equilibrium position in the microchannel. For all density-separated layers L1–L4, we observed a pronounced peak in the probability density distributions at the channel centers at low velocities ($< 5 \text{ mm.s}^{-1}$). As the velocity increased, the central position became less favorable, and an off-centered peak emerged. This transition in equilibrium position with increasing velocity has been reported in previous studies and is associated with the transition from symmetric to asymmetric shapes. Increasing the diamide concentration dramatically affected the equilibrium RBC position across the channel width. At a concentration of 0.5 mM, we found a large number of cells flowing closer to the channel center at high velocities, while the off-centered slipper peak was still visible. This effect qualitatively persisted as the diamide concentration further increased, with more cells flowing between the channel's centerline and the off-centered position of the slipper peak at concentrations above 0.5 mM. These observations provide new insights into the relationship between membrane rigidity and cell positioning in confined flow. The fraction of stable shapes decreased with increasing RBC age for the density-fractionated cells and with increasing diamide concentration for chemically modified cells. While nearly all cells had the same shape in the field of view for L1, only 63% of the RBCs in L4 exhibited a stable shape. Similarly, the fraction of stable shapes decreased from roughly 90% for fresh RBCs to 30% for cells treated with 2 mM diamide. This decrease in shape stability with age and increased membrane rigidity is consistent with previous studies on RBC mechanical

properties^[255,278].

6.1.3 Quantitative Assessment of RBC Deformability

Finalizing the whole study with our investigation into the deformability of RBCs utilizing a novel compression-expansion process through microchannels of varying widths has yielded significant insights into the complex interplay between cell age, shear rates, and deformability. The study was conducted using a double-width channel with $W_c = 8 \mu\text{m}$ and $W_e = 16 \mu\text{m}$, allowing for the observation of RBC behavior under various pressure conditions. A key finding of our research was the positive correlation between RBC compression and the pressure exerted across widened channels. Notably, we observed that the rate of compression relative to velocity decreased as cells transitioned into broader channels, highlighting the significant influence of channel geometry on RBC deformation dynamics^[11,279]. This observation aligns with previous studies on RBC behavior in microfluidic environments, while extending our understanding of the specific effects of channel width variations. The deformation rate (DR) exhibited a linear increase corresponding to escalating shear rates for cells sourced from whole blood, consistent with earlier investigations^[134,137]. However, our research goes beyond these previous observations by examining the effects of cell age and membrane rigidity on deformation characteristics. We found that compression magnitude and deformation rate decreased with advancing cell age, a phenomenon not previously reported in the context of microfluidic deformability assessments. This age-dependent variation in deformability could have significant implications for understanding RBC behavior in microcirculation and potential diagnostic applications^[19,280]. Interestingly, we observed relatively consistent deformation rates regardless of membrane rigidity as shear rate increased. This finding contrasts with some earlier studies that suggested a more pronounced effect of membrane rigidity on deformation^[81,281]. Our results indicate a more nuanced relationship between membrane properties and deformability under dynamic flow conditions, emphasizing the complexity of RBC mechanics in microfluidic environments. A particularly novel aspect of our study was the observation of a rebound effect in RBCs, displaying elastic behavior as the deformation index (DI) stabilized at a plateau. This phenomenon was more pronounced in younger cells, particularly those from layers L1 and L2, and diminished with cell age and increased rigidity. The relaxation time (τ) for young RBCs was found to be approximately 14 ms, gradually increasing to about 25 ms for older cells. These findings provide new insights into the viscoelastic properties of RBCs and their age-dependent variations^[57,238]. To quantify the extent of RBC deformation as they moved through channels of varying widths, we introduced a new metric, ΔDI , representing the difference between DI_8 and DI_{16} . This innovative approach allowed us to evaluate the deformation process more precisely, providing valuable insights into the mechanisms influencing RBC behavior in microchannels. Our analysis, involving a significant sample size of 1363 individual RBCs, revealed intriguing

patterns in the probabilistic distribution of DI_8 , DI_{16} , and ΔDI , shedding light on the complex relationship between RBC behavior and channel geometry. When subjecting RBCs to different pressure conditions within the channel, we observed that in the narrower channel section W_c , RBCs experienced significant compression, as indicated by DI_8 values ranging from 0 to 0.22. Conversely, as RBCs moved into the wider channel region W_e , the median values of DI_{16} showed a noticeable decrease, highlighting the impact of confinement-induced expansion forces. This shift was evident in DI_{16} values ranging from -0.12 to 0.16, emphasizing the interplay between channel width and RBC deformability.

Our comprehensive analysis of RBC deformability across different age groups and rigidity levels offers a more refined understanding of cellular mechanics in microfluidic environments. These results have potential implications for improving diagnostic techniques and our understanding of microcirculatory dynamics in health and disease. The observed variations in deformation characteristics with cell age and membrane rigidity underscore the importance of considering these factors in future studies and applications involving RBC mechanics in confined spaces^[73,277].

6.2 Implications and Future Directions

Our comprehensive investigation into RBC morphodynamics has yielded significant insights with far-reaching implications for both fundamental cellular biology and practical applications in biomedical engineering. The understanding of RBC behavior under various microfluidic conditions opens up new avenues for research and development across multiple disciplines.

6.2.1 Microfluidic Device Design

The detailed characterization of RBC shape classifications and behavior in confined channels provides a robust foundation for the development of tailored microfluidic devices. These findings can be leveraged to enhance diagnostic and analytical capabilities, particularly in the realm of point-of-care testing^[282]. By optimizing channel geometries based on our observations, future devices could achieve improved sensitivity and specificity in detecting subtle changes in RBC properties, potentially revolutionizing early disease detection and monitoring^[139].

6.2.2 Blood Flow Modeling

Our results offer crucial empirical data for refining the accuracy of RBC simulations and *in silico* modeling of blood flow, especially in complex microcirculatory systems. The observed variations in RBC deformability across different age groups and rigidity levels can be incorporated into multi-scale computational models, leading to more realistic representations of blood rheology in health and disease^[163]. These improved models could significantly enhance our

understanding of microvascular dynamics and inform the development of novel therapeutic strategies for circulatory disorders^[283].

6.2.3 Hematological Diagnostics

The distinct behavioral patterns of RBCs based on age and rigidity present exciting opportunities for developing new diagnostic tools for hematological disorders and vascular health assessment. By exploiting these differences, microfluidic-based assays could be designed to rapidly evaluate RBC population heterogeneity, providing valuable insights into various pathological conditions such as sickle cell disease, malaria, and diabetes-related microvascular complications^[238]. Furthermore, these findings could pave the way for non-invasive methods to assess overall cardiovascular health by analyzing RBC deformability profiles^[134].

6.2.4 Therapeutic Strategies

Understanding the factors influencing RBC deformability may inform the development of novel therapeutic approaches for conditions affecting blood flow and oxygen delivery. For instance, targeted interventions to modulate membrane rigidity or cellular aging processes could potentially improve microcirculatory function in various pathological states^[248]. Additionally, this knowledge could be applied to optimize blood storage techniques, enhancing the efficacy of transfusion therapies^[284].

6.2.5 Future Research Directions

Building upon our findings, several promising avenues for future research emerge:

- **Pathological Conditions:** Investigating the effects of specific diseases on RBC deformability and flow behavior in microchannels could provide valuable insights into disease mechanisms and progression. This could include studies on rare hematological disorders, infectious diseases affecting RBCs, and systemic conditions impacting blood rheology.
- **High-Throughput Assessment:** Exploring the potential of microfluidic devices for rapid, high-throughput evaluation of RBC properties in clinical settings could revolutionize diagnostic procedures. Development of automated, AI-assisted analysis systems could enable real-time assessment of large RBC populations, enhancing diagnostic accuracy and efficiency^[285].
- **Advanced Computational Modeling:** Developing more sophisticated computational models that incorporate the heterogeneity of RBC populations and complex microvascular geometries is crucial. These models should account for the dynamic interactions between RBCs, plasma components, and endothelial cells, providing a more comprehensive understanding of microcirculatory function^[286].

- **Long-term Physiological Implications:** Examining the long-term physiological consequences of altered RBC deformability on tissue oxygenation and overall cardiovascular health is essential. Longitudinal studies correlating RBC mechanical properties with clinical outcomes could provide valuable prognostic indicators for various cardiovascular and hematological disorders^[136].
- **Biomimetic Microfluidics:** Developing more physiologically relevant microfluidic systems that mimic the complex architecture and flow conditions of the microcirculation could enhance the translational potential of *in vitro* studies. These advanced platforms could incorporate endothelial cell layers, oxygen gradients, and pulsatile flow to better recapitulate the *in vivo* microenvironment^[287].

In conclusion, this comprehensive study of RBC morphodynamics provides a solid foundation for understanding the intricate interplay between cellular properties, environmental factors, and blood flow dynamics. By elucidating the nuanced effects of channel geometry, cell age, and membrane rigidity on RBC behavior, this work contributes significantly to our understanding of microcirculatory function and related pathologies. The insights gained from this research have the potential to drive innovations in hematology, vascular biology, and microfluidic technologies, ultimately leading to improved diagnostic and therapeutic strategies for a wide range of blood-related disorders.

Acknowledgments

I would like to take this opportunity to express my heartfelt gratitude to all those who have supported me throughout the journey of my thesis. This project would not have been possible without their invaluable contributions and encouragement.

First and foremost, I would like to extend my deepest appreciation to **Prof. Christian Wagner**, my professor, for his unwavering guidance and insightful feedback. Your expertise and encouragement have been instrumental in shaping my academic journey. I am profoundly grateful to **Dr. Steffen M. Recktenwald**, my supervisor, whose support in developing the concept of my studies has been invaluable. Your mentorship has provided me with the clarity and direction necessary to navigate the complexities of this research. My sincere thanks also go to **Dr. Alexis Darras** for his insightful suggestions and ideas that greatly enriched the conceptual framework of my thesis. Your ability to illuminate complex topics has been a source of inspiration. I would like to acknowledge **Dr. Thomas John** for his assistance in overcoming numerous technical challenges. Your expertise and patience made a significant difference in the progress of my work. A special thank you to **Frau Apfelbaum and Frau Zimmermann** for their help with administrative procedures. Your support ensured that I could focus on my research without unnecessary distractions. I am also grateful to my colleague and friend, **Mohamed Bendaoud**, for his camaraderie and support throughout this process. Your friendship has made this journey more enjoyable. My heartfelt appreciation goes to **Felix Maurer** and his family for their generous support, both as a colleague and as a friend. Your kindness has been a source of motivation for me. I would like to thank **Karin Kretsch** for her assistance in the laboratory, which was crucial in carrying out my experiments effectively. Additionally, I would like to acknowledge **Dr. Yazdan Rashidi** and **Khadija Larhrissi**, my colleagues, for their collaboration and support during this project. Lastly, I am immensely grateful to my friends—**Rachid, Rabie, Zakariya, Amine, Mohcin, Babaye, and Mehdi**—whose unwavering support and encouragement have kept me motivated during challenging times. Thank you for being there every step of the way.

This thesis is a reflection of our collective efforts, and I am truly thankful for each contribution that has brought me closer to this achievement.

- [1] Arthur C. Guyton and John E. Hall. *Guyton and Hall Textbook of Medical Physiology*. Elsevier, Oxford, England, UK, 2011. ISBN 978-1-41604574-8. URL <http://111.93.204.14:8080/xmlui/handle/123456789/791>.
- [2] Ganong Wf. Review of medical physiology. *Dynamics of blood and lymph flow*, 30:525–541, 1995. URL https://cir.nii.ac.jp/crid/1570009749769022336#citations_container.
- [3] A. V. Hoffbrand and P. A. H. Moss. *Fundamentos em Hematologia de Hoffbrand*. Artmed Editora, Brazil, November 2017. ISBN 978-85-8271451-5. URL https://books.google.de/books?id=EyU_DwAAQBAJ&dq=A.+Victor+Hoffbrand+and+Paul+A.+H.+Moss.+&lr=&source=gbs_navlinks_s.
- [4] Narla Mohandas and Patrick G. Gallagher. Red cell membrane: past, present, and future. *Blood*, 112(10):3939–3948, November 2008. ISSN 0006-4971. doi: [10.1182/blood-2008-07-161166](https://doi.org/10.1182/blood-2008-07-161166).
- [5] Maureane Hoffman and Dougald M. Monroe Iii. A Cell-based Model of Hemostasis. *Thromb. Haemost.*, 85(06):958–965, 2001. ISSN 0340-6245. doi: [10.1055/s-0037-1615947](https://doi.org/10.1055/s-0037-1615947).
- [6] Shaun P. Jackson. The growing complexity of platelet aggregation. *Blood*, 109(12):5087–5095, June 2007. ISSN 0006-4971. doi: [10.1182/blood-2006-12-027698](https://doi.org/10.1182/blood-2006-12-027698).
- [7] Blood Separation With Centrifuge - Glanlab Instrument. <https://www.glanlab.com/blood-separation-with-centrifuge.html>, August 2024.
- [8] Graham R. Serjeant. Sickle-cell disease. *Lancet*, 350(9079):725–730, September 1997. ISSN 0140-6736. doi: [10.1016/S0140-6736\(97\)07330-3](https://doi.org/10.1016/S0140-6736(97)07330-3).
- [9] Pasquale Memmolo, Lisa Miccio, Francesco Merola, Oriella Gennari, Paolo Antonio Netti, and Pietro Ferraro. 3d morphometry of red blood cells by digital holography. *Cytometry Part A*, 85:1030–1036, 12 2014. ISSN 1552-4930. doi: [10.1002/CYTO.A.22570](https://doi.org/10.1002/CYTO.A.22570). URL <https://onlinelibrary.wiley.com/doi/full/10.1002/cyto.a.22570>.
- [10] Nima Khatibzadeh, Sharad Gupta, et al. Effects of cholesterol on nano-mechanical properties of the living cell plasma membrane. *Soft Matter*, 8(32):8350–8360, July 2012. ISSN 1744-683X. doi: [10.1039/C2SM25263E](https://doi.org/10.1039/C2SM25263E).
- [11] Giovanna Tomaiuolo. Biomechanical properties of red blood cells in health and disease towards microfluidics. *Biomicrofluidics*, 8(5), September 2014. doi: [10.1063/1.4895755](https://doi.org/10.1063/1.4895755).
- [12] Claudia Trejo-Soto, Guillermo R. Lázaro, et al. Microfluidics Approach to the Mechanical Properties of Red Blood Cell Membrane and Their Effect on Blood Rheology. *Membranes*, 12(2):217, February 2022. ISSN 2077-0375. doi: [10.3390/membranes12020217](https://doi.org/10.3390/membranes12020217).
- [13] Joel Anne Chasis and Stephen B. Shoet. Red Cell Biochemical Anatomy and Membrane Properties. *Annu. Rev. Physiol.*, (Volume 49, 1987):237–248, March 1987. doi: [10.1146/annurev.ph.49.030187.001321](https://doi.org/10.1146/annurev.ph.49.030187.001321).
- [14] Yoshihito Yawata. *Cell Membrane: The Red Blood Cell as a Model*. Wiley, Weinheim, Germany, January 2006. ISBN 978-3-52760532-3. URL https://books.google.de/books?id=_FN6NID_CKIC&lr=&hl=de&source=gbs_navlinks_s.
- [15] I. Bernhardt and J. C. Ellory. *Red Cell Membrane Transport in Health and Disease*. Springer, Berlin, Germany, April 2013. ISBN 978-3-66205181-8. URL <https://books.google.ne/books?id=0v7uCAAAQBAJ>.

REFERENCES

- [16] J. Stuart and G. B. Nash. Red cell deformability and haematological disorders. *Blood Rev.*, 4(3):141–147, September 1990. ISSN 0268-960X. doi: [10.1016/0268-960X\(90\)90041-P](https://doi.org/10.1016/0268-960X(90)90041-P).
- [17] Manouk Abkarian and Annie Viallat. On the Importance of the Deformability of Red Blood Cells in Blood Flow. *Royal Society of Chemistry*, November 2015. doi: [10.1039/9781782628491-00347](https://doi.org/10.1039/9781782628491-00347).
- [18] Mary Risinger and Theodosia A. Kalfa. Red cell membrane disorders: structure meets function. *Blood*, 136(11):1250–1261, September 2020. ISSN 0006-4971. doi: [10.1182/blood.2019000946](https://doi.org/10.1182/blood.2019000946).
- [19] Timothy W. Secomb. Blood Flow in the Microcirculation. *Annu. Rev. Fluid Mech.*, (Volume 49, 2017):443–461, January 2017. doi: [10.1146/annurev-fluid-010816-060302](https://doi.org/10.1146/annurev-fluid-010816-060302).
- [20] Herbert H. Lipowsky. Microvascular Rheology and Hemodynamics. *Microcirculation*, January 2005. URL <https://www.tandfonline.com/doi/abs/10.1080/10739680590894966>.
- [21] Bruce Alberts, Dennis Bray, et al. *Essential Cell Biology*. Garland Science, Abingdon, England, UK, January 2015. ISBN 978-1-31780627-1. URL https://books.google.de/books?id=Cg4WAgAAQBAJ&dq=Bruce+Alberts,+Alexander+Johnson,+Julian+Lewis,+Martin+Raff,+Keith+Roberts,+and+Peter+Walter.+Molecular+Biology+of+the+Cell.+Garland+Science,+2015.&lr=&source=gbs_navlinks_s.
- [22] Lesley J. Bruce, Sandip Ghosh, et al. Absence of CD47 in protein 4.2-deficient hereditary spherocytosis in man: an interaction between the Rh complex and the band 3 complex Presented at the 43rd Annual Meeting of the American Society of Hematology, Orlando, FL, December 7-11, 2001, and abstract published in *Blood*. 2001;98:(suppl1):10a. *Blood*, 100(5):1878–1885, September 2002. ISSN 0006-4971. doi: [10.1182/blood-2002-03-0706](https://doi.org/10.1182/blood-2002-03-0706).
- [23] Xiuli An and Narla Mohandas. Disorders of red cell membrane. *Br. J. Haematol.*, 141(3):367–375, May 2008. ISSN 0007-1048. doi: [10.1111/j.1365-2141.2008.07091.x](https://doi.org/10.1111/j.1365-2141.2008.07091.x).
- [24] Lydie Da Costa, Julie Galimand, Odile Fenneteau, and Narla Mohandas. Hereditary spherocytosis, elliptocytosis, and other red cell membrane disorders. *Blood Rev.*, 27(4):167–178, July 2013. ISSN 0268-960X. doi: [10.1016/j.blre.2013.04.003](https://doi.org/10.1016/j.blre.2013.04.003).
- [25] Youngchan Kim, Kyoohyun Kim, et al. Measurement Techniques for Red Blood Cell Deformability: Recent Advances. In *Blood Cell - An Overview of Studies in Hematology*. IntechOpen, Croatia, September 2012. ISBN 978-953-51-0753-8. doi: [10.5772/50698](https://doi.org/10.5772/50698).
- [26] Prabhani U. Atukorale, Yu-Sang Yang, et al. Influence of the glycocalyx and plasma membrane composition on amphiphilic gold nanoparticle association with erythrocytes. *Nanoscale*, 7(26):11420–11432, June 2015. ISSN 2040-3364. doi: [10.1039/C5NR01355K](https://doi.org/10.1039/C5NR01355K).
- [27] A. Riggs and M. Wells. The oxygen equilibrium of sickle-cell hemoglobin. *Biochim. Biophys. Acta*, 50(2):243–248, June 1961. ISSN 0006-3002. doi: [10.1016/0006-3002\(61\)90322-5](https://doi.org/10.1016/0006-3002(61)90322-5).
- [28] Ruth E. Benesch and Reinhold Benesch. The Influence of Oxygenation on the Reactivity of the —SH Groups of Hemoglobin*. *Biochemistry*, 1(5):735–738, September 1962. ISSN 0006-2960. doi: [10.1021/bi00911a002](https://doi.org/10.1021/bi00911a002).
- [29] Max F. Perutz, Jane E. Ladner, et al. Influence of globin structure on the state of the heme. I. Human deoxyhemoglobin. *Biochemistry*, 13(10):2163–2173, May 1974. ISSN 0006-2960. doi: [10.1021/bi00707a026](https://doi.org/10.1021/bi00707a026).
- [30] Stock Images, Photos, Vectors, Video, and Music | Shutterstock, August 2024.
- [31] Linus Pauling, Harvey A. Itano, et al. Sickle Cell Anemia, a Molecular Disease. *Science*, 110(2865):543–548, November 1949. ISSN 0036-8075. doi: [10.1126/science.110.2865.543](https://doi.org/10.1126/science.110.2865.543).
- [32] Ivan Birukou, Rachel L. Schweers, and John S. Olson. Distal Histidine Stabilizes Bound O₂ and Acts as a Gate for Ligand Entry in Both Subunits of Adult Human Hemoglobin*. *J. Biol. Chem.*, 285(12):8840–8854, March 2010. ISSN 0021-9258. doi: [10.1074/jbc.M109.053934](https://doi.org/10.1074/jbc.M109.053934).
- [33] Maurizio Brunori, Robert W. Noble, Eraldo Antonini, and Jeffries Wyman. The Reactions of the Isolated α and β Chains of Human Hemoglobin with Oxygen and Carbon Monoxide. *J. Biol. Chem.*, 241(22):5238–5243, November 1966. ISSN 0021-9258. doi: [10.1016/S0021-9258\(18\)96423-9](https://doi.org/10.1016/S0021-9258(18)96423-9).
- [34] M. Brunori and T. M. Schuster. Kinetic Studies of Ligand Binding to Hemoglobin and Its Isolated Subunits by the Temperature Jump Relaxation Method. *J. Biol. Chem.*, 244(15):4046–4053, August 1969. ISSN 0021-9258. doi: [10.1016/S0021-9258\(17\)36383-4](https://doi.org/10.1016/S0021-9258(17)36383-4).

REFERENCES

- [35] R. W. Noble, Q. H. Gibson, M. Brunori, E. Antonini, and J. Wyman. The Rates of Combination of the Isolated Chains of Human Hemoglobin with Oxygen. *J. Biol. Chem.*, 244(14):3905–3908, July 1969. ISSN 0021-9258. doi: [10.1016/S0021-9258\(17\)36435-9](https://doi.org/10.1016/S0021-9258(17)36435-9).
- [36] E. Antonini and M. Brunori. Hemoglobin. *Annu. Rev. Biochem.*, (Volume 39, 1970):977–1042, July 1970. doi: [10.1146/annurev.bi.39.070170.004553](https://doi.org/10.1146/annurev.bi.39.070170.004553).
- [37] Virgilio L. Lew and Teresa Tiffert. On the Mechanism of Human Red Blood Cell Longevity: Roles of Calcium, the Sodium Pump, PIEZO1, and Gardos Channels. *Front. Physiol.*, 8:311944, December 2017. ISSN 1664-042X. doi: [10.3389/fphys.2017.00977](https://doi.org/10.3389/fphys.2017.00977).
- [38] Perumal Thiagarajan, Charles J. Parker, and Josef T. Prchal. How Do Red Blood Cells Die? *Front. Physiol.*, 12:655393, March 2021. ISSN 1664-042X. doi: [10.3389/fphys.2021.655393](https://doi.org/10.3389/fphys.2021.655393).
- [39] Joel Anne Chasis and Narla Mohandas. Erythroblastic islands: niches for erythropoiesis. *Blood*, 112(3):470–478, August 2008. ISSN 0006-4971. doi: [10.1182/blood-2008-03-077883](https://doi.org/10.1182/blood-2008-03-077883).
- [40] G. J. C. G. M. Bosman, J. M. Werre, F. L. A. Willekens, and V. M. J. Novotný. Erythrocyte ageing in vivo and in vitro: structural aspects and implications for transfusion. *Transfus. Med.*, 18(6):335–347, December 2008. ISSN 0958-7578. doi: [10.1111/j.1365-3148.2008.00892.x](https://doi.org/10.1111/j.1365-3148.2008.00892.x).
- [41] Anitra C. Carr, Mark R. McCall, and Balz Frei. Oxidation of LDL by Myeloperoxidase and Reactive Nitrogen Species. *Arterioscler., Thromb., Vasc. Biol.*, July 2000. doi: [10.1161/01.ATV.20.7.1716](https://doi.org/10.1161/01.ATV.20.7.1716).
- [42] Joy Mohanty, Enika Nagababu, and Joseph M. Rifkind. Red blood cell oxidative stress impairs oxygen delivery and induces red blood cell aging. *Front. Physiol.*, 5:75882, February 2014. ISSN 1664-042X. doi: [10.3389/fphys.2014.00084](https://doi.org/10.3389/fphys.2014.00084).
- [43] Samuel E. Lux. Anatomy of the red cell membrane skeleton: unanswered questions. *Blood*, 127(2):187–199, January 2016. ISSN 0006-4971. doi: [10.1182/blood-2014-12-512772](https://doi.org/10.1182/blood-2014-12-512772).
- [44] Joseph M. Rifkind and Enika Nagababu. Hemoglobin Redox Reactions and Red Blood Cell Aging. *Antioxid. Redox Signaling*, 18(17):2274–2283, April 2013. ISSN 1523-0864. doi: [10.1089/ars.2012.4867](https://doi.org/10.1089/ars.2012.4867).
- [45] Tigist Kassa, Sirsendu Jana, Michael Brad Strader, Fantao Meng, Yiping Jia, Michael T. Wilson, and Abdu I. Alayash. Sick Cell Hemoglobin in the Ferryl State Promotes β Cys-93 Oxidation and Mitochondrial Dysfunction in Epithelial Lung Cells (E10) *. *J. Biol. Chem.*, 290(46):27939–27958, November 2015. ISSN 0021-9258. doi: [10.1074/jbc.M115.651257](https://doi.org/10.1074/jbc.M115.651257).
- [46] Tae-Hoon Lee, Sun-Uk Kim, Seong-Lan Yu, Sue Hee Kim, Do Sim Park, Hyung-Bae Moon, So Hee Dho, Ki-Sun Kwon, Hyun Jeong Kwon, Ying-Hao Han, Sangkyun Jeong, Sang Won Kang, Hee-Sup Shin, Kyung-Kwang Lee, Sue Goo Rhee, and Dae-Yeul Yu. Peroxiredoxin II is essential for sustaining life span of erythrocytes in mice. *Blood*, 101(12):5033–5038, June 2003. ISSN 0006-4971. doi: [10.1182/blood-2002-08-2548](https://doi.org/10.1182/blood-2002-08-2548).
- [47] Frans L. A. Willekens, Jan M. Werre, J. Kar Kruijt, Bregt Roerdinkholder-Stoelwinder, Yvonne A. M. Groenen-Doepp, Annegeet G. van den Bos, Giel J. C. G. M. Bosman, and Theo J. C. van Berkel. Liver Kupffer cells rapidly remove red blood cell-derived vesicles from the circulation by scavenger receptors. *Blood*, 105(5):2141–2145, March 2005. ISSN 0006-4971. doi: [10.1182/blood-2004-04-1578](https://doi.org/10.1182/blood-2004-04-1578).
- [48] Giel J. C. G. M. Bosman, Edwin Lasonder, Marleen Lutten, Bregt Roerdinkholder-Stoelwinder, Věra M. J. Novotný, Harry Bos, and Willem J. De Grip. The proteome of red cell membranes and vesicles during storage in blood bank conditions. *Transfusion*, 48(5):827–835, May 2008. ISSN 0041-1132. doi: [10.1111/j.1537-2995.2007.01630.x-i2](https://doi.org/10.1111/j.1537-2995.2007.01630.x-i2).
- [49] Guillaume Deplaine, Innocent Safeukui, et al. The sensing of poorly deformable red blood cells by the human spleen can be mimicked in vitro. *Blood*, 117(8):e88–e95, February 2011. ISSN 0006-4971. doi: [10.1182/blood-2010-10-312801](https://doi.org/10.1182/blood-2010-10-312801).
- [50] Reina E. Mebius and Georg Kraal. Structure and function of the spleen. *Nat. Rev. Immunol.*, 5:606–616, August 2005. ISSN 1474-1741. doi: [10.1038/nri1669](https://doi.org/10.1038/nri1669).
- [51] Djuna Z. de Back, Elena B. Kostova, et al. Of macrophages and red blood cells; a complex love story. *Front. Physiol.*, 5:74689, January 2014. ISSN 1664-042X. doi: [10.3389/fphys.2014.00009](https://doi.org/10.3389/fphys.2014.00009).
- [52] James Palis. Primitive and definitive erythropoiesis in mammals. *Front. Physiol.*, 5:74694, January 2014. ISSN 1664-042X. doi: [10.3389/fphys.2014.00003](https://doi.org/10.3389/fphys.2014.00003).

REFERENCES

- [53] Kenneth Kaushansky. Thrombopoiesis. *Semin. Hematol.*, 52(1):4–11, January 2015. ISSN 0037-1963. doi: [10.1053/j.seminhematol.2014.10.003](https://doi.org/10.1053/j.seminhematol.2014.10.003).
- [54] S. Chien. Red Cell Deformability and its Relevance to Blood Flow. *Annu. Rev. Physiol.*, (Volume 49, 1987): 177–192, March 1987. doi: [10.1146/annurev.ph.49.030187.001141](https://doi.org/10.1146/annurev.ph.49.030187.001141).
- [55] Jules Dupire, Marius Socol, et al. Full dynamics of a red blood cell in shear flow. *Proc. Natl. Acad. Sci. U.S.A.*, 109(51):20808–20813, December 2012. doi: [10.1073/pnas.1210236109](https://doi.org/10.1073/pnas.1210236109).
- [56] P. B. Canham and Alan C. Burton. Distribution of Size and Shape in Populations of Normal Human Red Cells. *Circ. Res.*, March 1968. doi: [10.1161/01.RES.22.3.405](https://doi.org/10.1161/01.RES.22.3.405).
- [57] Jonathan B. Freund. Numerical Simulation of Flowing Blood Cells. *Annu. Rev. Fluid Mech.*, (Volume 46, 2014): 67–95, January 2014. doi: [10.1146/annurev-fluid-010313-141349](https://doi.org/10.1146/annurev-fluid-010313-141349).
- [58] R. Skalak and P. I. Brånemark. Deformation of Red Blood Cells in Capillaries. *Science*, 164(3880):717–719, May 1969. ISSN 0036-8075. doi: [10.1126/science.164.3880.717](https://doi.org/10.1126/science.164.3880.717).
- [59] C. Pozrikidis. Effect of membrane bending stiffness on the deformation of capsules in simple shear flow. *J. Fluid Mech.*, 440:269–291, August 2001. ISSN 1469-7645. doi: [10.1017/S0022112001004657](https://doi.org/10.1017/S0022112001004657).
- [60] Manouk Abkarian, Magalie Faivre, et al. Swinging of Red Blood Cells under Shear Flow. *Phys. Rev. Lett.*, 98(18): 188302, April 2007. ISSN 1079-7114. doi: [10.1103/PhysRevLett.98.188302](https://doi.org/10.1103/PhysRevLett.98.188302).
- [61] Secomb T. W. Mechanics of blood flow in the microcirculation. *Symp. Soc. Exp. Biol.*, 49:305–321, January 1995. ISSN 0081-1386. URL <https://europepmc.org/article/med/8571232>.
- [62] R. M. Hochmuth and R. E. Waugh. Erythrocyte Membrane Elasticity and Viscosity. *Annu. Rev. Physiol.*, (Volume 49, 1987):209–219, March 1987. doi: [10.1146/annurev.ph.49.030187.001233](https://doi.org/10.1146/annurev.ph.49.030187.001233).
- [63] Dmitry A. Fedosov, Bruce Caswell, et al. A Multiscale Red Blood Cell Model with Accurate Mechanics, Rheology, and Dynamics. *Biophys. J.*, 98(10):2215–2225, May 2010. ISSN 0006-3495. doi: [10.1016/j.bpj.2010.02.002](https://doi.org/10.1016/j.bpj.2010.02.002).
- [64] J. Liam McWhirter, Hiroshi Noguchi, et al. Flow-induced clustering and alignment of vesicles and red blood cells in microcapillaries. *Proc. Natl. Acad. Sci. U.S.A.*, 106(15):6039–6043, April 2009. doi: [10.1073/pnas.0811484106](https://doi.org/10.1073/pnas.0811484106).
- [65] Jonathan B. Freund. The flow of red blood cells through a narrow spleen-like slit. *Phys. Fluids*, 25(11):110807, August 2013. ISSN 1070-6631. doi: [10.1063/1.4819341](https://doi.org/10.1063/1.4819341).
- [66] N. Mohandas and Chasis J. A. Red blood cell deformability, membrane material properties and shape: regulation by transmembrane, skeletal and cytosolic proteins and lipids. *Semin. Hematol.*, 30(3):171–192, July 1993. ISSN 0037-1963. URL https://europepmc.org/article/med/8211222?utm_medium=email&utm_source=transaction.
- [67] Sara Salehyar and Qiang Zhu. Deformation and internal stress in a red blood cell as it is driven through a slit by an incoming flow. *Soft Matter*, 12(13):3156–3164, March 2016. ISSN 1744-683X. doi: [10.1039/C5SM02933C](https://doi.org/10.1039/C5SM02933C).
- [68] T. M. Fischer, C. W. M. Haest, et al. Selective alteration of erythrocyte deformability by SH-reagents. Evidence for an involvement of spectrin in membrane shear elasticity. *Biochimica et Biophysica Acta (BBA) - Biomembranes*, 510(2):270–282, July 1978. ISSN 0005-2736. doi: [10.1016/0005-2736\(78\)90027-5](https://doi.org/10.1016/0005-2736(78)90027-5).
- [69] Dmitry A. Fedosov, Bruce Caswell, et al. Systematic coarse-graining of spectrin-level red blood cell models. *Comput. Methods Appl. Mech. Eng.*, 199(29-32):10.1016/j.cma.2010.02.001., June 2010. ISSN 0045-7825. doi: [10.1016/j.cma.2010.02.001](https://doi.org/10.1016/j.cma.2010.02.001).
- [70] Manouk Abkarian and Annie Viallat. Vesicles and red blood cells in shear flow. *Soft Matter*, 4(4):653–657, March 2008. ISSN 1744-683X. doi: [10.1039/B716612E](https://doi.org/10.1039/B716612E).
- [71] Scott Atwell, Catherine Badens, et al. Dynamics of Individual Red Blood Cells Under Shear Flow: A Way to Discriminate Deformability Alterations. *Front. Physiol.*, 12:775584, January 2022. ISSN 1664-042X. doi: [10.3389/fphys.2021.775584](https://doi.org/10.3389/fphys.2021.775584).
- [72] A. Viallat and M. Abkarian. Red blood cell: from its mechanics to its motion in shear flow. *Int. J. Labor. Hematol.*, 36(3):237–243, June 2014. ISSN 1751-5521. doi: [10.1111/ijlh.12233](https://doi.org/10.1111/ijlh.12233).
- [73] Luca Lanotte, Johannes Mauer, Simon Mendez, Dmitry A. Fedosov, Jean-Marc Fromental, Viviana Claveria, Franck Nicoud, Gerhard Gompper, and Manouk Abkarian. Red cells’ dynamic morphologies govern blood shear thinning under microcirculatory flow conditions. *Proc. Natl. Acad. Sci. U.S.A.*, 113(47):13289–13294, November 2016. doi: [10.1073/pnas.1608074113](https://doi.org/10.1073/pnas.1608074113).

- [74] Alexander Kihm, Lars Kaestner, et al. Classification of red blood cell shapes in flow using outlier tolerant machine learning. *PLoS Comput. Biol.*, 14(6):e1006278, June 2018. ISSN 1553-7358. doi: [10.1371/journal.pcbi.1006278](https://doi.org/10.1371/journal.pcbi.1006278).
- [75] Achim Guckenberger, Alexander Kihm, et al. Numerical–experimental observation of shape bistability of red blood cells flowing in a microchannel. *Soft Matter*, 14(11):2032–2043, March 2018. ISSN 1744-683X. doi: [10.1039/C7SM02272G](https://doi.org/10.1039/C7SM02272G).
- [76] Steffen M. Recktenwald, Katharina Graessel, et al. Red blood cell shape transitions and dynamics in time-dependent capillary flows. *Biophys. J.*, 121(1):23–36, January 2022. ISSN 0006-3495. doi: [10.1016/j.bpj.2021.12.009](https://doi.org/10.1016/j.bpj.2021.12.009).
- [77] Antonia Rabe, Alexander Kihm, et al. The Erythrocyte Sedimentation Rate and Its Relation to Cell Shape and Rigidity of Red Blood Cells from Chorea-Acanthocytosis Patients in an Off-Label Treatment with Dasatinib. *Biomolecules*, 11(5):727, May 2021. ISSN 2218-273X. doi: [10.3390/biom11050727](https://doi.org/10.3390/biom11050727).
- [78] Steffen M. Recktenwald, Marcelle G. M. Lopes, et al. ErySense, a Lab-on-a-Chip-Based Point-of-Care Device to Evaluate Red Blood Cell Flow Properties With Multiple Clinical Applications. *Front. Physiol.*, 13:884690, April 2022. ISSN 1664-042X. doi: [10.3389/fphys.2022.884690](https://doi.org/10.3389/fphys.2022.884690).
- [79] Steffen M. Recktenwald, Greta Simionato, et al. Cross-talk between red blood cells and plasma influences blood flow and omics phenotypes in severe COVID-19. *eLife*, December 2022. doi: [10.7554/eLife.81316](https://doi.org/10.7554/eLife.81316).
- [80] Felix Reichel, Martin Kräter, et al. Changes in Blood Cell Deformability in Chorea-Acanthocytosis and Effects of Treatment With Dasatinib or Lithium. *Front. Physiol.*, 13:852946, April 2022. ISSN 1664-042X. doi: [10.3389/fphys.2022.852946](https://doi.org/10.3389/fphys.2022.852946).
- [81] Dmitry A. Fedosov, Matti Peltomäki, et al. Deformation and dynamics of red blood cells in flow through cylindrical microchannels. *Soft Matter*, 10(24):4258–4267, May 2014. ISSN 1744-683X. doi: [10.1039/C4SM00248B](https://doi.org/10.1039/C4SM00248B).
- [82] Anil K. Dasanna, Johannes Mauer, et al. Importance of Viscosity Contrast for the Motion of Erythrocytes in Microcapillaries. *Front. Phys.*, 9:666913, May 2021. ISSN 2296-424X. doi: [10.3389/fphys.2021.666913](https://doi.org/10.3389/fphys.2021.666913).
- [83] Giorgio Gianini Morbioli, Nicholas Colby Speller, et al. A practical guide to rapid-prototyping of PDMS-based microfluidic devices: A tutorial. *Anal. Chim. Acta*, 1135:150–174, October 2020. ISSN 0003-2670. doi: [10.1016/j.aca.2020.09.013](https://doi.org/10.1016/j.aca.2020.09.013).
- [84] Kangning Ren, Jianhua Zhou, et al. Materials for Microfluidic Chip Fabrication. *Acc. Chem. Res.*, 46(11):2396–2406, November 2013. ISSN 0001-4842. doi: [10.1021/ar300314s](https://doi.org/10.1021/ar300314s).
- [85] Fabio Guglietta, Marek Behr, et al. On the effects of membrane viscosity on transient red blood cell dynamics. *Soft Matter*, 16(26):6191–6205, July 2020. ISSN 1744-683X. doi: [10.1039/D0SM00587H](https://doi.org/10.1039/D0SM00587H).
- [86] Ali Gürbüz, On Shun Pak, et al. Effects of membrane viscoelasticity on the red blood cell dynamics in a microcapillary. *Biophys. J.*, 122(11):2230–2241, June 2023. ISSN 0006-3495. doi: [10.1016/j.bpj.2023.01.010](https://doi.org/10.1016/j.bpj.2023.01.010).
- [87] Robert S. Franco. The measurement and importance of red cell survival. *Am. J. Hematol.*, 84(2):109–114, February 2009. ISSN 0361-8609. doi: [10.1002/ajh.21298](https://doi.org/10.1002/ajh.21298).
- [88] Anna Bogdanova and Hans U. Lutz. Mechanisms tagging senescent red blood cells for clearance in healthy humans. *Front. Physiol.*, 4:73608, December 2013. ISSN 1664-042X. doi: [10.3389/fphys.2013.00387](https://doi.org/10.3389/fphys.2013.00387).
- [89] Lars Kaestner and Giampaolo Minetti. The potential of erythrocytes as cellular aging models - Cell Death & Differentiation. *Nature*, 24:1475–1477, June 2017. ISSN 1476-5403. doi: [10.1038/cdd.2017.100](https://doi.org/10.1038/cdd.2017.100).
- [90] Angelo D’Alessandro, Pier Giorgio Righetti, et al. The Red Blood Cell Proteome and Interactome: An Update. *J. Proteome Res.*, 9(1):144–163, January 2010. ISSN 1535-3893. doi: [10.1021/pr900831f](https://doi.org/10.1021/pr900831f).
- [91] Patrizia Caprari, Angelo Scuteri, et al. Aging and red blood cell membrane: a study of centenarians. *Exp. Gerontol.*, 34(1):47–57, January 1999. ISSN 0531-5565. doi: [10.1016/S0531-5565\(98\)00055-2](https://doi.org/10.1016/S0531-5565(98)00055-2).
- [92] Umakant J. Dumaswala, Limei Zhuo, et al. Protein and lipid oxidation of banked human erythrocytes: Role of glutathione. *Free Radical Biol. Med.*, 27(9):1041–1049, November 1999. ISSN 0891-5849. doi: [10.1016/S0891-5849\(99\)00149-5](https://doi.org/10.1016/S0891-5849(99)00149-5).
- [93] Inna Freikman and Eitan Fibach. Distribution and shedding of the membrane phosphatidylserine during maturation and aging of erythroid cells. *Biochimica et Biophysica Acta (BBA) - Biomembranes*, 1808(12):2773–2780, December 2011. ISSN 0005-2736. doi: [10.1016/j.bbamem.2011.08.014](https://doi.org/10.1016/j.bbamem.2011.08.014).

REFERENCES

- [94] M. R. Clark. Senescence of red blood cells: progress and problems. *Physiol. Rev.*, April 1988. doi: [10.1152/physrev.1988.68.2.503](https://doi.org/10.1152/physrev.1988.68.2.503).
- [95] J. A. Chasis and N. Mohandas. Erythrocyte membrane deformability and stability: two distinct membrane properties that are independently regulated by skeletal protein associations. *J. Cell Biol.*, 103(2):343–350, August 1986. ISSN 0021-9525. doi: [10.1083/jcb.103.2.343](https://doi.org/10.1083/jcb.103.2.343).
- [96] M. Musielak. Red blood cell-deformability measurement: Review of techniques. *Clin. Hemorheol. Microcirc.*, 42(1):47–64, January 2009. ISSN 1386-0291. doi: [10.3233/CH-2009-1187](https://doi.org/10.3233/CH-2009-1187).
- [97] D. Platt and P. Norwig. Biochemical studies of membrane glycoproteins during red cell aging. *Mech. Ageing Dev.*, 14(1):119–126, September 1980. ISSN 0047-6374. doi: [10.1016/0047-6374\(80\)90110-4](https://doi.org/10.1016/0047-6374(80)90110-4).
- [98] Heather N. Colvin, Elmira Alipour, et al. An Ex Vivo Model of Oxidatively Stressed Red Blood Cells Demonstrates a Role for Exogenous Amino Acids in Enhancing Red Blood Cell Function and Morphology. *Blood*, 138:922, November 2021. ISSN 0006-4971. doi: [10.1182/blood-2021-153836](https://doi.org/10.1182/blood-2021-153836).
- [99] Niels Lion, David Crettaz, et al. Stored red blood cells: A changing universe waiting for its map(s). *J. Proteomics*, 73(3):374–385, January 2010. ISSN 1874-3919. doi: [10.1016/j.jprot.2009.11.001](https://doi.org/10.1016/j.jprot.2009.11.001).
- [100] Angelo D’Alessandro, Giancarlo Liumbruno, et al. Red blood cell storage: the story so far. *Blood Transfusion*, 8(2):82, April 2010. doi: [10.2450/2009.0122-09](https://doi.org/10.2450/2009.0122-09).
- [101] Tatsuro Yoshida, Michel Prudent, et al. Red blood cell storage lesion: causes and potential clinical consequences. *Blood Transfusion*, 17(1):27, January 2019. doi: [10.2450/2019.0217-18](https://doi.org/10.2450/2019.0217-18).
- [102] Angelo D’Alessandro, Julie A. Reisz, et al. Effects of aged stored autologous red blood cells on human plasma metabolome. *Blood Adv.*, 3(6):884–896, March 2019. ISSN 2473-9529. doi: [10.1182/bloodadvances.2018029629](https://doi.org/10.1182/bloodadvances.2018029629).
- [103] Anastasios G. Kriebardis, Marianna H. Antonelou, et al. RBC-derived vesicles during storage: ultrastructure, protein composition, oxidation, and signaling components. *Transfusion*, 48(9):1943–1953, September 2008. ISSN 0041-1132. doi: [10.1111/j.1537-2995.2008.01794.x](https://doi.org/10.1111/j.1537-2995.2008.01794.x).
- [104] John R. Hess. Red cell changes during storage. *Transfusion and Apheresis Science*, 43(1):51–59, August 2010. ISSN 1473-0502. doi: [10.1016/j.transci.2010.05.009](https://doi.org/10.1016/j.transci.2010.05.009).
- [105] Michaël Chassé, Lauralyn McIntyre, et al. Clinical effects of blood donor characteristics in transfusion recipients: protocol of a framework to study the blood donor–recipient continuum. *BMJ Open*, 5(1):e007412, January 2015. ISSN 2044-6055. doi: [10.1136/bmjopen-2014-007412](https://doi.org/10.1136/bmjopen-2014-007412).
- [106] Michaël Chassé, Lauralyn McIntyre, et al. Effect of Blood Donor Characteristics on Transfusion Outcomes: A Systematic Review and Meta-Analysis. *Transfus. Med. Rev.*, 30(2):69–80, April 2016. ISSN 0887-7963. doi: [10.1016/j.tmr.2016.01.002](https://doi.org/10.1016/j.tmr.2016.01.002).
- [107] Olga Mykhaïlova, Carly Olafson, et al. Donor-dependent aging of young and old red blood cell subpopulations: Metabolic and functional heterogeneity. *Transfusion*, 60(11):2633–2646, November 2020. ISSN 0041-1132. doi: [10.1111/trf.16017](https://doi.org/10.1111/trf.16017).
- [108] Gregory Barshtein, Ivana Pajic-Lijakovic, et al. Deformability of Stored Red Blood Cells. *Front. Physiol.*, 12:722896, September 2021. ISSN 1664-042X. doi: [10.3389/fphys.2021.722896](https://doi.org/10.3389/fphys.2021.722896).
- [109] Eldad A. Hod and Steven L. Spitalnik. Harmful effects of transfusion of older stored red blood cells: iron and inflammation. *Transfusion*, 51(4):881–885, April 2011. ISSN 0041-1132. doi: [10.1111/j.1537-2995.2011.03096.x](https://doi.org/10.1111/j.1537-2995.2011.03096.x).
- [110] B. Blasi, A. D’Alessandro, et al. Red blood cell storage and cell morphology. *Transfus. Med.*, 22(2):90–96, April 2012. ISSN 0958-7578. doi: [10.1111/j.1365-3148.2012.01139.x](https://doi.org/10.1111/j.1365-3148.2012.01139.x).
- [111] María García-Roa, María del Carmen Vicente-Ayuso, et al. Red blood cell storage time and transfusion: current practice, concerns and future perspectives. *Blood Transfusion*, 15(3):222, May 2017. doi: [10.2450/2017.0345-16](https://doi.org/10.2450/2017.0345-16).
- [112] Nareg H. Roubinian, Sarah E. Reese, et al. Donor genetic and nongenetic factors affecting red blood cell transfusion effectiveness. *JCI Insight*, 7(1), January 2022. doi: [10.1172/jci.insight.152598](https://doi.org/10.1172/jci.insight.152598).
- [113] N. Mohandas and E. Evans. Mechanical Properties of the Red Cell Membrane in. *Annu. Rev. Biophys.*, (Volume 23, 1994):787–818, June 1994. doi: [10.1146/annurev.bb.23.060194.004035](https://doi.org/10.1146/annurev.bb.23.060194.004035).

REFERENCES

- [114] S. Suresh, J. Spatz, et al. Connections between single-cell biomechanics and human disease states: gastrointestinal cancer and malaria. *Acta Biomater.*, 1(1):15–30, January 2005. ISSN 1742-7061. doi: [10.1016/j.actbio.2004.09.001](https://doi.org/10.1016/j.actbio.2004.09.001).
- [115] Dondorp A. M., Angus B. J., et al. Red blood cell deformability as a predictor of anemia in severe falciparum malaria. *Am. J. Trop. Med. Hyg.*, 60(5):733–737, May 1999. ISSN 0002-9637. doi: [10.4269/ajtmh.1999.60.733](https://doi.org/10.4269/ajtmh.1999.60.733).
- [116] M. R. Clark, N. Mohandas, et al. Deformability of oxygenated irreversibly sickled cells. *J. Clin. Invest.*, 65(1):189–196, January 1980. ISSN 0021-9738. doi: [10.1172/JCI109650](https://doi.org/10.1172/JCI109650).
- [117] Patrick G. Gallagher. Red Cell Membrane Disorders. *Hematology*, 2005(1):13–18, December 2005. ISSN 1520-4391. doi: [10.1182/asheducation-2005.1.13](https://doi.org/10.1182/asheducation-2005.1.13).
- [118] Robert M. Hochmuth. Micropipette aspiration of living cells. *J. Biomech.*, 33(1):15–22, January 2000. ISSN 0021-9290. doi: [10.1016/S0021-9290\(99\)00175-X](https://doi.org/10.1016/S0021-9290(99)00175-X).
- [119] Ameya Sinha, Trang T. T. Chu, et al. Single-cell evaluation of red blood cell bio-mechanical and nano-structural alterations upon chemically induced oxidative stress. *Sci. Rep.*, 5(9768):1–8, May 2015. ISSN 2045-2322. doi: [10.1038/srep09768](https://doi.org/10.1038/srep09768).
- [120] Subra Suresh. Biomechanics and biophysics of cancer cells. *Acta Biomater.*, 3(4):413–438, July 2007. ISSN 1742-7061. doi: [10.1016/j.actbio.2007.04.002](https://doi.org/10.1016/j.actbio.2007.04.002).
- [121] Muhammad S. Yousafzai, Giovanna Coceano, et al. Effect of neighboring cells on cell stiffness measured by optical tweezers indentation. In *Journal of Biomedical Optics, Vol. 21, Issue 5*, volume 21, page 057004. SPIE, May 2016. doi: [10.1117/1.JBO.21.5.057004](https://doi.org/10.1117/1.JBO.21.5.057004).
- [122] J. P. Mills, M. Diez-Silva, et al. Effect of plasmodial RESA protein on deformability of human red blood cells harboring Plasmodium falciparum. *Proc. Natl. Acad. Sci. U.S.A.*, 104(22):9213–9217, May 2007. doi: [10.1073/pnas.0703433104](https://doi.org/10.1073/pnas.0703433104).
- [123] Lei Gu, William A. Smith, et al. Mechanical Fragility Calibration of Red Blood Cells. *ASAIO J.*, 51(3):194, May 2005. ISSN 1058-2916. doi: [10.1097/01.MAT.0000161940.30190.6D](https://doi.org/10.1097/01.MAT.0000161940.30190.6D).
- [124] Innocent Safeukui, Pierre A. Buffet, et al. Quantitative assessment of sensing and sequestration of spherocytic erythrocytes by the human spleen. *Blood*, 120(2):424–430, July 2012. ISSN 0006-4971. doi: [10.1182/blood-2012-01-404103](https://doi.org/10.1182/blood-2012-01-404103).
- [125] Luke A. Ziegler, Salim E. Olia, et al. Red Blood Cell Mechanical Fragility Test for Clinical Research Applications. *Artif. Organs*, 41(7):678–682, July 2017. ISSN 0160-564X. doi: [10.1111/aor.12826](https://doi.org/10.1111/aor.12826).
- [126] R. Waugh and E. A. Evans. Thermoelasticity of red blood cell membrane. *Biophys. J.*, 1(26):115–131, 1979. ISSN 0006-3495. doi: [10.1016/S0006-3495\(79\)85239-X](https://doi.org/10.1016/S0006-3495(79)85239-X).
- [127] Bernhard Deuticke. Transformation and restoration of biconcave shape of human erythrocytes induced by amphiphilic agents and changes of ionic environment. *Biochimica et Biophysica Acta (BBA) - Biomembranes*, 163(4):494–500, December 1968. ISSN 0005-2736. doi: [10.1016/0005-2736\(68\)90078-3](https://doi.org/10.1016/0005-2736(68)90078-3).
- [128] Nobuji Maeda, Kazunori Kon, et al. Alteration of rheological properties of human erythrocytes by crosslinking of membrane proteins. *Biochimica et Biophysica Acta (BBA) - Biomembranes*, 735(1):104–112, October 1983. ISSN 0005-2736. doi: [10.1016/0005-2736\(83\)90265-1](https://doi.org/10.1016/0005-2736(83)90265-1).
- [129] Guillermo R. Lázaro, Aurora Hernández-Machado, et al. Rheology of red blood cells under flow in highly confined microchannels. II. Effect of focusing and confinement. *Soft Matter*, 10(37):7207–7217, August 2014. ISSN 1744-683X. doi: [10.1039/C4SM01382D](https://doi.org/10.1039/C4SM01382D).
- [130] Xiaolong Wang, Satoshi Ii, et al. Effect of mechanical properties of red blood cells on their equilibrium states in microchannels. *Phys. Fluids*, 35(3), March 2023. ISSN 1070-6631. doi: [10.1063/5.0141811](https://doi.org/10.1063/5.0141811).
- [131] Mohammed Nouaman, Alexis Darras, et al. Effect of Cell Age and Membrane Rigidity on Red Blood Cell Shape in Capillary Flow. *Cells*, 12(11):1529, June 2023. ISSN 2073-4409. doi: [10.3390/cells12111529](https://doi.org/10.3390/cells12111529).
- [132] Mohammed Nouaman, Alexis Darras, Christian Wagner, and Steffen M. Recktenwald. Confinement effect on the microcapillary flow and shape of red blood cells. *Biomicrofluidics*, 18(2), March 2024. doi: [10.1063/5.0197208](https://doi.org/10.1063/5.0197208).
- [133] Vera Faustino, Susana O. Catarino, et al. Biomedical microfluidic devices by using low-cost fabrication techniques: A review. *J. Biomech.*, 49(11):2280–2292, July 2016. ISSN 0021-9290. doi: [10.1016/j.jbiomech.2015.11.031](https://doi.org/10.1016/j.jbiomech.2015.11.031).

REFERENCES

- [134] Michael J. Simmonds, Herbert J. Meiselman, et al. Blood rheology and aging. *Journal of Geriatric Cardiology : JGC*, 10(3):291, September 2013. doi: [10.3969/j.issn.1671-5411.2013.03.010](https://doi.org/10.3969/j.issn.1671-5411.2013.03.010).
- [135] Monica Diez-Silva, Ming Dao, et al. Shape and Biomechanical Characteristics of Human Red Blood Cells in Health and Disease. *MRS Bull.*, 35(5):382–388, May 2010. ISSN 1938-1425. doi: [10.1557/mrs2010.571](https://doi.org/10.1557/mrs2010.571).
- [136] Oguz K. Baskurt and Herbert J. Meiselman. Blood Rheology and Hemodynamics. *Semin. Thromb. Hemost.*, 29(05):435–450, 2003. ISSN 0094-6176. doi: [10.1055/s-2003-44551](https://doi.org/10.1055/s-2003-44551).
- [137] Alison M. Forsyth, Jiandi Wan, et al. The dynamic behavior of chemically “stiffened” red blood cells in microchannel flows. *Microvasc. Res.*, 80(1):37–43, July 2010. ISSN 0026-2862. doi: [10.1016/j.mvr.2010.03.008](https://doi.org/10.1016/j.mvr.2010.03.008).
- [138] Giovanna Tomaiuolo and Stefano Guido. Start-up shape dynamics of red blood cells in microcapillary flow. *Microvasc. Res.*, 82(1):35–41, July 2011. ISSN 0026-2862. doi: [10.1016/j.mvr.2011.03.004](https://doi.org/10.1016/j.mvr.2011.03.004).
- [139] Yi Zheng, John Nguyen, et al. Recent advances in microfluidic techniques for single-cell biophysical characterization. *Lab Chip*, 13(13):2464–2483, June 2013. ISSN 1473-0197. doi: [10.1039/C3LC50355K](https://doi.org/10.1039/C3LC50355K).
- [140] David Bento, Raquel O. Rodrigues, Vera Faustino, Diana Pinho, Carla S. Fernandes, Ana I. Pereira, Valdemar Garcia, João M. Miranda, and Rui Lima. Deformation of Red Blood Cells, Air Bubbles, and Droplets in Microfluidic Devices: Flow Visualizations and Measurements. *Micromachines*, 9(4):151, March 2018. ISSN 2072-666X. doi: [10.3390/mi9040151](https://doi.org/10.3390/mi9040151).
- [141] Gaël Prado, Alexander Farutin, et al. Viscoelastic Transient of Confined Red Blood Cells. *Biophys. J.*, 108(9):2126–2136, May 2015. ISSN 0006-3495. doi: [10.1016/j.bpj.2015.03.046](https://doi.org/10.1016/j.bpj.2015.03.046).
- [142] Nina T. Holland, Martyn T. Smith, et al. Biological sample collection and processing for molecular epidemiological studies. *Mutat. Res.*, 543(3):217–234, June 2003. ISSN 0027-5107. doi: [10.1016/s1383-5742\(02\)00090-x](https://doi.org/10.1016/s1383-5742(02)00090-x).
- [143] Mehmet Toner and Daniel Irimia. Blood-on-a-chip. *Annu. Rev. Biomed. Eng.*, 7:77-103.(;):Annu, 2005. ISSN 1523-9829. doi: [10.1146/annurev.bioeng.7.011205.135108](https://doi.org/10.1146/annurev.bioeng.7.011205.135108).
- [144] Albert J. Mach and Dino Di Carlo. Continuous scalable blood filtration device using inertial microfluidics. *Biotechnol. Bioeng.*, 107(2):302–311, October 2010. ISSN 1097-0290. doi: [10.1002/bit.22833](https://doi.org/10.1002/bit.22833).
- [145] Lindsay A. Alaishuski, Rodney D. Grim, et al. The informed consent process in whole blood donation. *Arch. Pathol. Lab. Med.*, 132(6):947–951, June 2008. ISSN 0003-9985. URL <https://pure.psu.edu/en/publications/the-informed-consent-process-in-whole-blood-donation>.
- [146] Brian Grainger and Peter Flanagan. Informed consent for whole blood donation. *Vox Sang.*, 115(1):3–10, January 2020. ISSN 0042-9007. doi: [10.1111/vox.12866](https://doi.org/10.1111/vox.12866).
- [147] Oguz K. Baskurt, Michel Boynard, Giles C. Cokelet, Philippe Connes, Brian M. Cooke, Sandro Forconi, Fulong Liao, Max R. Hardeman, Friedrich Jung, Herbert J. Meiselman, Gerard Nash, Norbert Nemeth, Björn Neu, Bo Sandhagen, Sehyun Shin, George Thurston, and Jean Luc Wautier. New guidelines for hemorheological laboratory techniques. *Clinical Hemorheology and Microcirculation*, 42:75–97, 2009. ISSN 13860291. doi: [10.3233/CH-2009-1202](https://doi.org/10.3233/CH-2009-1202).
- [148] A.J. Keidan, M.C. Sowter, S.S. Marwah, C.S. Johnson, and J. Stuart. Evaluation of hepes and phosphate buffers for rheological studies of sickle cells. *Clinical Hemorheology and Microcirculation*, 7:599–610, 12 2016. ISSN 18758622. doi: [10.3233/CH-1987-7405](https://doi.org/10.3233/CH-1987-7405).
- [149] L.E.Göran Eriksson. On the shape of human red blood cells interacting with flat artificial surfaces — the ‘glass effect’. *Biochimica et Biophysica Acta (BBA) - General Subjects*, 1036:193–201, 12 1990. ISSN 03044165. doi: [10.1016/0304-4165\(90\)90034-T](https://doi.org/10.1016/0304-4165(90)90034-T).
- [150] Petr Ermolinskiy, Andrei Lugovtsov, et al. Effect of Red Blood Cell Aging In Vivo on Their Aggregation Properties In Vitro: Measurements with Laser Tweezers. *Appl. Sci.*, 10(21):7581, October 2020. ISSN 2076-3417. doi: [10.3390/app10217581](https://doi.org/10.3390/app10217581).
- [151] Anupam Sengupta, Stephan Herminghaus, et al. Liquid crystal microfluidics: surface, elastic and viscous interactions at microscales. *Liq. Cryst. Rev.*, July 2014. URL <https://www.tandfonline.com/doi/abs/10.1080/21680396.2014.963716>.
- [152] Douglas B. Weibel, Willow R. DiLuzio, et al. Microfabrication meets microbiology. *Nat. Rev. Microbiol.*, 5:209–218, March 2007. ISSN 1740-1534. doi: [10.1038/nrmicro1616](https://doi.org/10.1038/nrmicro1616).

REFERENCES

- [153] Alexander Kihm. *Deformability-Induced Effects of Red Blood Cells in Flow*. PhD thesis, Universität Des Saarlandes, 2021.
- [154] Yoji Suzuki, Norihiko Tateishi, et al. Deformation of Erythrocytes in Microvessels and Glass Capillaries: Effects of Erythrocyte Deformability. *Microcirculation*, 3(1):49–57, March 1996. ISSN 1073-9688. doi: [10.3109/10739689609146782](https://doi.org/10.3109/10739689609146782).
- [155] Axel R. Pries and Timothy W. Secomb. Blood Flow in Microvascular Networks. In *Microcirculation (Second Edition)*, pages 3–36. Academic Press, Cambridge, MA, USA, January 2008. ISBN 978-0-12-374530-9. doi: [10.1016/B978-0-12-374530-9.00001-2](https://doi.org/10.1016/B978-0-12-374530-9.00001-2).
- [156] U. Bagge, Brånemark P. I., et al. Three-dimensional observations of red blood cell deformation in capillaries. *Blood Cells*, 6(2):231–239, January 1980. ISSN 0340-4684. URL <https://europepmc.org/article/med/7378593>.
- [157] P. Gaehtgens, C. Dührssen, et al. Motion, deformation, and interaction of blood cells and plasma during flow through narrow capillary tubes. *Blood Cells*, 6(4):799–817, January 1980. ISSN 0340-4684. URL <https://europepmc.org/article/med/7470632>.
- [158] Stefano Guido and Giovanna Tomaiuolo. Microconfined flow behavior of red blood cells in vitro. *C. R. Phys.*, 10(8):751–763, November 2009. ISSN 1631-0705. doi: [10.1016/j.crhy.2009.10.002](https://doi.org/10.1016/j.crhy.2009.10.002).
- [159] Giovanna Tomaiuolo, Marino Simeone, et al. Red blood cell deformation in microconfined flow. *Soft Matter*, 5(19):3736–3740, September 2009. ISSN 1744-683X. doi: [10.1039/B904584H](https://doi.org/10.1039/B904584H).
- [160] Judith C. A. Cluitmans, Venkatachalam Chokkalingam, et al. Alterations in Red Blood Cell Deformability during Storage: A Microfluidic Approach. *Biomed Res. Int.*, 2014(1):764268, January 2014. ISSN 2314-6133. doi: [10.1155/2014/764268](https://doi.org/10.1155/2014/764268).
- [161] Giovanna Tomaiuolo, Luca Lanotte, Rosa D’Apolito, Antonio Cassinese, and Stefano Guido. Microconfined flow behavior of red blood cells. *Med. Eng. Phys.*, 38(1):11–16, January 2016. ISSN 1350-4533. doi: [10.1016/j.medengphy.2015.05.007](https://doi.org/10.1016/j.medengphy.2015.05.007).
- [162] Amir Saadat, Diego A. Huyke, et al. A system for the high-throughput measurement of the shear modulus distribution of human red blood cells. *Lab Chip*, 20(16):2927–2936, August 2020. ISSN 1473-0197. doi: [10.1039/D0LC00283F](https://doi.org/10.1039/D0LC00283F).
- [163] Dmitry A. Fedosov, Hiroshi Noguchi, et al. Multiscale modeling of blood flow: from single cells to blood rheology. *Biomech. Model. Mechanobiol.*, 13(2):239–258, April 2014. ISSN 1617-7940. doi: [10.1007/s10237-013-0497-9](https://doi.org/10.1007/s10237-013-0497-9).
- [164] Felix Reichel, Johannes Mauer, et al. High-Throughput Microfluidic Characterization of Erythrocyte Shapes and Mechanical Variability. *Biophys. J.*, 117(1):14–24, July 2019. ISSN 0006-3495. doi: [10.1016/j.bpj.2019.05.022](https://doi.org/10.1016/j.bpj.2019.05.022).
- [165] Yuncheng Man, Erdem Kucukal, et al. Microfluidic assessment of red blood cell mediated microvascular occlusion. *Lab Chip*, 20(12):2086–2099, June 2020. ISSN 1473-0197. doi: [10.1039/D0LC00112K](https://doi.org/10.1039/D0LC00112K).
- [166] Kerryn Matthews, Erik S. Lamoureux, et al. Technologies for measuring red blood cell deformability. *Lab Chip*, 22(7):1254–1274, March 2022. ISSN 1473-0197. doi: [10.1039/D1LC01058A](https://doi.org/10.1039/D1LC01058A).
- [167] Adrian Bejan. Convection heat transfer: Fourth edition. *Convection Heat Transfer: Fourth Edition*, 3 2013. doi: [10.1002/9781118671627](https://doi.org/10.1002/9781118671627). URL <https://onlinelibrary.wiley.com/doi/10.1002/9781118671627.fmatter>.
- [168] James Friend and Leslie Yeo. Fabrication of microfluidic devices using polydimethylsiloxane. *Biomicrofluidics*, 4(2):026502, March 2010. doi: [10.1063/1.3259624](https://doi.org/10.1063/1.3259624).
- [169] Thomas Gervais, Jamil El-Ali, et al. Flow-induced deformation of shallow microfluidic channels. *Lab Chip*, 6(4):500–507, March 2006. ISSN 1473-0197. doi: [10.1039/B513524A](https://doi.org/10.1039/B513524A).
- [170] Brian S. Hardy, Kawika Uechi, et al. The deformation of flexible PDMS microchannels under a pressure driven flow. *Lab Chip*, 9(7):935–938, April 2009. ISSN 1473-0197. doi: [10.1039/B813061B](https://doi.org/10.1039/B813061B).
- [171] David W. Inglis. A method for reducing pressure-induced deformation in silicone microfluidics. *Biomicrofluidics*, 4(2):026504, June 2010. doi: [10.1063/1.3431715](https://doi.org/10.1063/1.3431715).
- [172] M. Kiran Raj and Suman Chakraborty. PDMS microfluidics: A mini review. *J. Appl. Polym. Sci.*, 137(27):48958, July 2020. ISSN 0021-8995. doi: [10.1002/app.48958](https://doi.org/10.1002/app.48958).

REFERENCES

- [173] Steffen M. Recktenwald, Katharina Graessel, et al. Cell-free layer of red blood cells in a constricted microfluidic channel under steady and time-dependent flow conditions. *Phys. Rev. Fluids*, 8(7):074202, July 2023. ISSN 2469-990X. doi: [10.1103/PhysRevFluids.8.074202](https://doi.org/10.1103/PhysRevFluids.8.074202).
- [174] W. Macosko C. Rheology Principles. *Measurements and Applications*, 1994. URL <https://cir.nii.ac.jp/crid/1573387449190639744>.
- [175] Naoki Takeishi, Hiroaki Ito, et al. Deformation of a Red Blood Cell in a Narrow Rectangular Microchannel. *Micromachines*, 10(3):199, March 2019. ISSN 2072-666X. doi: [10.3390/mi10030199](https://doi.org/10.3390/mi10030199).
- [176] Sylvie Hénon, Guillaume Lenormand, et al. A New Determination of the Shear Modulus of the Human Erythrocyte Membrane Using Optical Tweezers. *Biophys. J.*, 76(2):1145–1151, February 1999. ISSN 0006-3495. doi: [10.1016/S0006-3495\(99\)77279-6](https://doi.org/10.1016/S0006-3495(99)77279-6).
- [177] Kushal Sinha and Michael D. Graham. Dynamics of a single red blood cell in simple shear flow. *Phys. Rev. E*, 92(4):042710, October 2015. ISSN 2470-0053. doi: [10.1103/PhysRevE.92.042710](https://doi.org/10.1103/PhysRevE.92.042710).
- [178] T. W. Secomb. Flow-dependent rheological properties of blood in capillaries. *Microvasc. Res.*, 34(1):46–58, July 1987. ISSN 0026-2862. doi: [10.1016/0026-2862\(87\)90078-1](https://doi.org/10.1016/0026-2862(87)90078-1).
- [179] Kosuke Tsukada, Eiichi Sekizuka, et al. Direct Measurement of Erythrocyte Deformability in Diabetes Mellitus with a Transparent Microchannel Capillary Model and High-Speed Video Camera System. *Microvasc. Res.*, 61(3):231–239, May 2001. ISSN 0026-2862. doi: [10.1006/mvre.2001.2307](https://doi.org/10.1006/mvre.2001.2307).
- [180] Giovanna Tomaiuolo, Mario Barra, et al. Microfluidics analysis of red blood cell membrane viscoelasticity. *Lab Chip*, 11(3):449–454, February 2011. ISSN 1473-0197. doi: [10.1039/C0LC00348D](https://doi.org/10.1039/C0LC00348D).
- [181] Viviana Clavería, Othmane Aouane, et al. Clusters of red blood cells in microcapillary flow: hydrodynamic versus macromolecule induced interaction. *Soft Matter*, 12(39):8235–8245, October 2016. ISSN 1744-683X. doi: [10.1039/C6SM01165A](https://doi.org/10.1039/C6SM01165A).
- [182] Johannes Mauer, Simon Mendez, et al. Flow-Induced Transitions of Red Blood Cell Shapes under Shear. *Phys. Rev. Lett.*, 121(11):118103, September 2018. ISSN 1079-7114. doi: [10.1103/PhysRevLett.121.118103](https://doi.org/10.1103/PhysRevLett.121.118103).
- [183] A. Symeonidis, G. Athanassiou, et al. Impairment of erythrocyte viscoelasticity is correlated with levels of glycosylated haemoglobin in diabetic patients. *Clin. Lab. Haematol.*, 23(2):103–109, April 2001. ISSN 0141-9854. doi: [10.1046/j.1365-2257.2001.00366.x](https://doi.org/10.1046/j.1365-2257.2001.00366.x).
- [184] A. M. Dondorp, M. Nyanoti, et al. The role of reduced red cell deformability in the pathogenesis of severe falciparum malaria and its restoration by blood transfusion. *Trans. R. Soc. Trop. Med. Hyg.*, 96(3):282–286, May 2002. ISSN 0035-9203. doi: [10.1016/S0035-9203\(02\)90100-8](https://doi.org/10.1016/S0035-9203(02)90100-8).
- [185] Robert Mannino, David R. Myers, et al. Increased Erythrocyte Rigidity Is Sufficient to Cause Endothelial Dysfunction in Sickle Cell Disease. *Blood*, 120(21):818, November 2012. ISSN 0006-4971. doi: [10.1182/blood.V120.21.818.818](https://doi.org/10.1182/blood.V120.21.818.818).
- [186] Manouk Abkarian, Magalie Faivre, et al. High-speed microfluidic differential manometer for cellular-scale hydrodynamics. *Proc. Natl. Acad. Sci. U.S.A.*, 103(3):538–542, January 2006. doi: [10.1073/pnas.0507171102](https://doi.org/10.1073/pnas.0507171102).
- [187] Susanne Braunmüller, Lothar Schmid, et al. Hydrodynamic deformation reveals two coupled modes/time scales of red blood cell relaxation. *Soft Matter*, 8(44):11240–11248, October 2012. ISSN 1744-683X. doi: [10.1039/C2SM26513C](https://doi.org/10.1039/C2SM26513C).
- [188] Badr Kaoui, George Biros, et al. Why Do Red Blood Cells Have Asymmetric Shapes Even in a Symmetric Flow? *Phys. Rev. Lett.*, 103(18):188101, October 2009. ISSN 1079-7114. doi: [10.1103/PhysRevLett.103.188101](https://doi.org/10.1103/PhysRevLett.103.188101).
- [189] N. Tahiri, T. Biben, et al. On the problem of slipper shapes of red blood cells in the microvasculature. *Microvasc. Res.*, 85:40–45, January 2013. ISSN 0026-2862. doi: [10.1016/j.mvr.2012.10.001](https://doi.org/10.1016/j.mvr.2012.10.001).
- [190] Ting Ye, Huixin Shi, et al. Numerical studies of a red blood cell in rectangular microchannels. *J. Appl. Phys.*, 122(8):084701, August 2017. ISSN 0021-8979. doi: [10.1063/1.5000357](https://doi.org/10.1063/1.5000357).
- [191] Dania Fischer, Julian Büsow, Patrick Meybohm, Christian Friedrich Weber, Kai Zacharowski, Anja Urbschat, Markus Matthias Müller, and Carla Jennewein. Microparticles from stored red blood cells enhance procoagulant and proinflammatory activity. *Transfusion*, 57(11):2701–2711, November 2017. ISSN 0041-1132. doi: [10.1111/trf.14268](https://doi.org/10.1111/trf.14268).

REFERENCES

- [192] Thomas M. Fischer. Shape Memory of Human Red Blood Cells. *Biophys. J.*, 86(5):3304–3313, May 2004. ISSN 0006-3495. doi: [10.1016/S0006-3495\(04\)74378-7](https://doi.org/10.1016/S0006-3495(04)74378-7).
- [193] S. Quint, A. F. Christ, et al. 3D tomography of cells in micro-channels. *Appl. Phys. Lett.*, 111(10):103701, September 2017. ISSN 0003-6951. doi: [10.1063/1.4986392](https://doi.org/10.1063/1.4986392).
- [194] Julie Martin-Wortham, Steffen M. Recktenwald, et al. A deep learning-based concept for high throughput image flow cytometry. *Appl. Phys. Lett.*, 118(12):123701, March 2021. ISSN 0003-6951. doi: [10.1063/5.0037336](https://doi.org/10.1063/5.0037336).
- [195] Marcelle G. M. Lopes, Steffen M. Recktenwald, et al. Big Data in Transfusion Medicine and Artificial Intelligence Analysis for Red Blood Cell Quality Control. *Transfus. Med. Hemother.*, 50(3):163–173, June 2023. ISSN 1660-3796. doi: [10.1159/000530458](https://doi.org/10.1159/000530458).
- [196] J. Duez, J. P. Holleran, et al. Mechanical clearance of red blood cells by the human spleen: Potential therapeutic applications of a biomimetic RBC filtration method. *Transfus. Clin. Biol.*, 22(3):151–157, August 2015. ISSN 1246-7820. doi: [10.1016/j.tracli.2015.05.004](https://doi.org/10.1016/j.tracli.2015.05.004).
- [197] He Li, Zixiang Leonardo Liu, et al. How the spleen reshapes and retains young and old red blood cells: A computational investigation. *PLoS Comput. Biol.*, 17(11):e1009516, November 2021. ISSN 1553-7358. doi: [10.1371/journal.pcbi.1009516](https://doi.org/10.1371/journal.pcbi.1009516).
- [198] O. Linderkamp and H. J. Meiselman. Geometric, osmotic, and membrane mechanical properties of density-separated human red cells. *Blood*, 59(6):1121–1127, June 1982. ISSN 0006-4971. doi: [10.1182/blood.V59.6.1121.1121](https://doi.org/10.1182/blood.V59.6.1121.1121).
- [199] R. E. Waugh, M. Narla, et al. Rheologic properties of senescent erythrocytes: loss of surface area and volume with red blood cell age. *Blood*, 79(5):1351–1358, March 1992. ISSN 0006-4971. doi: [10.1182/blood.V79.5.1351.1351](https://doi.org/10.1182/blood.V79.5.1351.1351).
- [200] F. H. Bosch, J. M. Werre, et al. Determinants of red blood cell deformability in relation to cell age. *Eur. J. Haematol.*, 52(1):35–41, January 1994. ISSN 0902-4441. doi: [10.1111/j.1600-0609.1994.tb01282.x](https://doi.org/10.1111/j.1600-0609.1994.tb01282.x).
- [201] Sean C. Gifford, Jure Derganc, et al. A detailed study of time-dependent changes in human red blood cells: from reticulocyte maturation to erythrocyte senescence. *Br. J. Haematol.*, 135(3):395–404, November 2006. ISSN 0007-1048. doi: [10.1111/j.1365-2141.2006.06279.x](https://doi.org/10.1111/j.1365-2141.2006.06279.x).
- [202] Marianna H. Antonelou, Anastasios G. Kriebardis, et al. Aging and death signalling in mature red cells: from basic science to transfusion practice. *Blood Transfusion*, 8(Suppl 3):s39, June 2010. doi: [10.2450/2010.007S](https://doi.org/10.2450/2010.007S).
- [203] G. J. C. G. M. Bosman, E. Lasonder, et al. Comparative proteomics of erythrocyte aging in vivo and in vitro. *J. Proteomics*, 73(3):396–402, January 2010. ISSN 1876-7737. doi: [10.1016/j.jprot.2009.07.010](https://doi.org/10.1016/j.jprot.2009.07.010).
- [204] Yao-Xiong Huang, Zheng-Jie Wu, et al. Human red blood cell aging: correlative changes in surface charge and cell properties. *J. Cell. Mol. Med.*, 15(12):2634–2642, December 2011. ISSN 1582-1838. doi: [10.1111/j.1582-4934.2011.01310.x](https://doi.org/10.1111/j.1582-4934.2011.01310.x).
- [205] Daniel Alexander Bizjak, Christian Brinkmann, et al. Increase in Red Blood Cell-Nitric Oxide Synthase Dependent Nitric Oxide Production during Red Blood Cell Aging in Health and Disease: A Study on Age Dependent Changes of Rheologic and Enzymatic Properties in Red Blood Cells. *PLoS One*, 10(4):e0125206, April 2015. ISSN 1932-6203. doi: [10.1371/journal.pone.0125206](https://doi.org/10.1371/journal.pone.0125206).
- [206] F. H. Bosch, J. M. Werre, et al. Characteristics of red blood cell populations fractionated with a combination of counterflow centrifugation and Percoll separation. *Blood*, 79(1):254–260, January 1992. ISSN 0006-4971. doi: [10.1182/blood.V79.1.254.254](https://doi.org/10.1182/blood.V79.1.254.254).
- [207] Angelo D’Alessandro, Barbara Blasi, et al. Red blood cell subpopulations in freshly drawn blood: application of proteomics and metabolomics to a decades-long biological issue. *Blood Transfusion*, 11(1):75, January 2013. doi: [10.2450/2012.0164-11](https://doi.org/10.2450/2012.0164-11).
- [208] Felix Maurer, Thomas John, et al. Continuous Percoll Gradient Centrifugation of Erythrocytes—Explanation of Cellular Bands and Compromised Age Separation. *Cells*, 11(8):1296, April 2022. ISSN 2073-4409. doi: [10.3390/cells11081296](https://doi.org/10.3390/cells11081296).
- [209] Magalie Faivre, Céline Renoux, et al. Mechanical Signature of Red Blood Cells Flowing Out of a Microfluidic Constriction Is Impacted by Membrane Elasticity, Cell Surface-to-Volume Ratio and Diseases. *Front. Physiol.*, 11:534357, June 2020. ISSN 1664-042X. doi: [10.3389/fphys.2020.00576](https://doi.org/10.3389/fphys.2020.00576).
- [210] Anna Bogdanova, Lars Kaestner, et al. Heterogeneity of Red Blood Cells: Causes and Consequences. *Front. Physiol.*, 11:526790, May 2020. ISSN 1664-042X. doi: [10.3389/fphys.2020.00392](https://doi.org/10.3389/fphys.2020.00392).

-
- [211] C. Pfafferoth, G. B. Nash, et al. Red blood cell deformation in shear flow. Effects of internal and external phase viscosity and of in vivo aging. *Biophys. J.*, 47(5):695–704, May 1985. ISSN 0006-3495. doi: [10.1016/S0006-3495\(85\)83966-7](https://doi.org/10.1016/S0006-3495(85)83966-7).
- [212] Takeshi Shiga, Misuzu Sekiya, et al. Cell age-dependent changes in deformability and calcium accumulation of human erythrocytes. *Biochimica et Biophysica Acta (BBA) - Biomembranes*, 814(2):289–299, April 1985. ISSN 0005-2736. doi: [10.1016/0005-2736\(85\)90447-X](https://doi.org/10.1016/0005-2736(85)90447-X).
- [213] Gerrit Danker, Petia M. Vlahovska, et al. Vesicles in Poiseuille Flow. *Phys. Rev. Lett.*, 102(14):148102, April 2009. ISSN 1079-7114. doi: [10.1103/PhysRevLett.102.148102](https://doi.org/10.1103/PhysRevLett.102.148102).
- [214] Alireza Z. K. Yazdani and Prosenjit Bagchi. Phase diagram and breathing dynamics of a single red blood cell and a biconcave capsule in dilute shear flow. *Phys. Rev. E*, 84(2):026314, August 2011. ISSN 2470-0053. doi: [10.1103/PhysRevE.84.026314](https://doi.org/10.1103/PhysRevE.84.026314).
- [215] B. Kaoui, N. Tahiri, et al. Complexity of vesicle microcirculation. *Phys. Rev. E*, 84(4):041906, October 2011. ISSN 2470-0053. doi: [10.1103/PhysRevE.84.041906](https://doi.org/10.1103/PhysRevE.84.041906).
- [216] Badr Kaoui, Timm Krüger, et al. How does confinement affect the dynamics of viscous vesicles and red blood cells? *Soft Matter*, 8(35):9246–9252, August 2012. ISSN 1744-683X. doi: [10.1039/C2SM26289D](https://doi.org/10.1039/C2SM26289D).
- [217] Daniel Cordasco, Alireza Yazdani, and Prosenjit Bagchi. Comparison of erythrocyte dynamics in shear flow under different stress-free configurations. *Physics of Fluids*, 26, 4 2014. ISSN 10897666. doi: [10.1063/1.4871300/314557](https://doi.org/10.1063/1.4871300/314557). URL [/aip/pof/article/26/4/041902/314557/Comparison-of-erythrocyte-dynamics-in-shear-flow](http://aip/pof/article/26/4/041902/314557/Comparison-of-erythrocyte-dynamics-in-shear-flow).
- [218] Alexander Farutin and Chaouqi Misbah. Symmetry breaking and cross-streamline migration of three-dimensional vesicles in an axial poiseuille flow. *Physical Review E - Statistical, Nonlinear, and Soft Matter Physics*, 89: 042709, 4 2014. ISSN 15502376. doi: [10.1103/PHYSREVE.89.042709](https://doi.org/10.1103/PHYSREVE.89.042709). URL <https://journals.aps.org/pre/abstract/10.1103/PhysRevE.89.042709>.
- [219] Moritz, Sebastian Johannes Müller, et al. Efficient viscosity contrast calculation for blood flow simulations using the lattice Boltzmann method. *Int. J. Numer. Methods Fluids*, 92(11):1463–1477, November 2020. ISSN 0271-2091. doi: [10.1002/fld.4835](https://doi.org/10.1002/fld.4835).
- [220] R. Skalak, A. Tozeren, et al. Strain Energy Function of Red Blood Cell Membranes. *Biophys. J.*, 13(3):245–264, March 1973. ISSN 0006-3495. doi: [10.1016/S0006-3495\(73\)85983-1](https://doi.org/10.1016/S0006-3495(73)85983-1).
- [221] W. Helfrich. Elastic Properties of Lipid Bilayers: Theory and Possible Experiments. *Zeitschrift für Naturforschung C*, 28(11-12):693–703, December 1973. ISSN 1865-7125. doi: [10.1515/znc-1973-11-1209](https://doi.org/10.1515/znc-1973-11-1209).
- [222] Dominique Barthès-Biesel, Anna Diaz, et al. Effect of constitutive laws for two-dimensional membranes on flow-induced capsule deformation. *J. Fluid Mech.*, 460:211–222, June 2002. ISSN 1469-7645. doi: [10.1017/S0022112002008352](https://doi.org/10.1017/S0022112002008352).
- [223] J. M. Skotheim and T. W. Secomb. Red Blood Cells and Other Nonspherical Capsules in Shear Flow: Oscillatory Dynamics and the Tank-Treading-to-Tumbling Transition. *Phys. Rev. Lett.*, 98(7):078301, February 2007. ISSN 1079-7114. doi: [10.1103/PhysRevLett.98.078301](https://doi.org/10.1103/PhysRevLett.98.078301).
- [224] Othmane Aouane, Marine Thiébaud, et al. Vesicle dynamics in a confined Poiseuille flow: From steady state to chaos. *Phys. Rev. E*, 90(3):033011, September 2014. ISSN 2470-0053. doi: [10.1103/PhysRevE.90.033011](https://doi.org/10.1103/PhysRevE.90.033011).
- [225] Thierry Mignon and Simon Mendez. A theoretical investigation of the frisbee motion of red blood cells in shear flow. *Math. Model. Nat. Phenom.*, 16:23, 2021. ISSN 0973-5348. doi: [10.1051/mmnp/2021014](https://doi.org/10.1051/mmnp/2021014).
- [226] R. M. Hochmuth, P. R. Worthy, et al. Red cell extensional recovery and the determination of membrane viscosity. *Biophys. J.*, 26(1):101–114, April 1979. ISSN 0006-3495. doi: [10.1016/S0006-3495\(79\)85238-8](https://doi.org/10.1016/S0006-3495(79)85238-8).
- [227] P. Matteoli, F. Nicoud, et al. Impact of the membrane viscosity on the tank-treading behavior of red blood cells. *Phys. Rev. Fluids*, 6(4):043602, April 2021. ISSN 2469-990X. doi: [10.1103/PhysRevFluids.6.043602](https://doi.org/10.1103/PhysRevFluids.6.043602).
- [228] Meredith E. Fay, David R. Myers, et al. Cellular softening mediates leukocyte demargination and trafficking, thereby increasing clinical blood counts. *Proc. Natl. Acad. Sci. U.S.A.*, 113(8):1987–1992, February 2016. doi: [10.1073/pnas.1508920113](https://doi.org/10.1073/pnas.1508920113).
- [229] G. Ciasca, M. Papi, et al. Mapping viscoelastic properties of healthy and pathological red blood cells at the nanoscale level. *Nanoscale*, 7(40):17030–17037, October 2015. ISSN 2040-3364. doi: [10.1039/C5NR03145A](https://doi.org/10.1039/C5NR03145A).
-

REFERENCES

- [230] O. K. Baskurt and H. J. Meiselman. Determination of Red Blood Cell Shape Recovery Time Constant in a Couette System by the Analysis of Light Reflectance and Ektacytometry. *Biorheology*, 33(6):489–503, January 1996. ISSN 0006-355X. doi: [10.3233/BIR-1996-33607](https://doi.org/10.3233/BIR-1996-33607).
- [231] P. J. Bronkhorst, G. J. Streekstra, et al. A new method to study shape recovery of red blood cells using multiple optical trapping. *Biophys. J.*, 69(5):1666, November 1995. doi: [10.1016/S0006-3495\(95\)80084-6](https://doi.org/10.1016/S0006-3495(95)80084-6).
- [232] Johannes G. G. Dobbe, Geert J. Streekstra, et al. Sylllectometry: the effect of aggregometer geometry in the assessment of red blood cell shape recovery and aggregation. *IEEE Trans. Biomed. Eng.*, 50(1):97–106, January 2003. ISSN 0018-9294. doi: [10.1109/TBME.2002.807319](https://doi.org/10.1109/TBME.2002.807319).
- [233] Marina Puig-de Morales-Marinkovic, Kevin T. Turner, et al. Viscoelasticity of the human red blood cell. *American Journal of Physiology-Cell Physiology*, August 2007. URL <https://journals.physiology.org/doi/full/10.1152/ajpce11.00562.2006>.
- [234] Ting Ye, Nhan Phan-Thien, et al. Stretching and Relaxation of Malaria-Infected Red Blood Cells. *Biophys. J.*, 105(5):1103–1109, September 2013. ISSN 0006-3495. doi: [10.1016/j.bpj.2013.07.008](https://doi.org/10.1016/j.bpj.2013.07.008).
- [235] Guansheng Li, He Li, et al. Red blood cell passage through deformable interendothelial slits in the spleen: Insights into splenic filtration and hemodynamics. *bioRxiv*, page 2024.02.22.581664, February 2024. URL <https://doi.org/10.1101/2024.02.22.581664>.
- [236] Iwona Cicha, Yoji Suzuki, et al. Gamma-Ray-Irradiated Red Blood Cells Stored in Mannitol-Adenine-Phosphate Medium: Rheological Evaluation and Susceptibility to Oxidative Stress. *Vox Sang.*, 79(2):75–82, September 2000. ISSN 0042-9007. doi: [10.1046/j.1423-0410.2000.7920075.x](https://doi.org/10.1046/j.1423-0410.2000.7920075.x).
- [237] Max R. Hardeman, Geert A. J. Besselink, et al. Laser-assisted optical rotational cell analyzer measurements reveal early changes in human RBC deformability induced by photodynamic treatment. *Transfusion*, 43(11):1533–1537, November 2003. ISSN 0041-1132. doi: [10.1046/j.1537-2995.2003.00566.x](https://doi.org/10.1046/j.1537-2995.2003.00566.x).
- [238] Yang Jun Kang. RBC deformability measurement based on variations of pressure in multiple micropillar channels during blood delivery using a disposable air-compressed pump. *Anal. Methods*, 10(37):4549–4561, September 2018. ISSN 1759-9660. doi: [10.1039/C8AY01486H](https://doi.org/10.1039/C8AY01486H).
- [239] E. Pretorius. Erythrocyte deformability and eryptosis during inflammation, and impaired blood rheology. *Clin. Hemorheol. Microcirc.*, 69(4):545–550, January 2018. ISSN 1386-0291. doi: [10.3233/CH-189205](https://doi.org/10.3233/CH-189205).
- [240] Amit K. Saha, Brendan R. Schmidt, et al. Red blood cell deformability is diminished in patients with Chronic Fatigue Syndrome. *Clin. Hemorheol. Microcirc.*, 71(1):113–116, January 2019. ISSN 1386-0291. doi: [10.3233/CH-180469](https://doi.org/10.3233/CH-180469).
- [241] Alberto M. Gambaruto. Flow structures and red blood cell dynamics in arteriole of dilated or constricted cross section. *J. Biomech.*, 49(11):2229–2240, July 2016. ISSN 0021-9290. doi: [10.1016/j.jbiomech.2015.11.023](https://doi.org/10.1016/j.jbiomech.2015.11.023).
- [242] Kanti Bhooshan Pandey and Syed Ibrahim Rizvi. Biomarkers of oxidative stress in red blood cells. *Biomed. Pap. Med. Fac. Univ. Palacky Olomouc Czech. Repub.*, 155(2):131–136, June 2011. ISSN 1804-7521. doi: [10.5507/bp.2011.027](https://doi.org/10.5507/bp.2011.027).
- [243] Yi Zheng, Ehsan Shojaei-Baghini, et al. High-throughput biophysical measurement of human red blood cells. *Lab Chip*, 12(14):2560–2567, June 2012. ISSN 1473-0197. doi: [10.1039/C2LC21210B](https://doi.org/10.1039/C2LC21210B).
- [244] D. B. Dill and D. L. Costill. Calculation of percentage changes in volumes of blood, plasma, and red cells in dehydration. *J. Appl. Physiol.*, 37(2):247–248, August 1974. ISSN 0021-8987. doi: [10.1152/jappl.1974.37.2.247](https://doi.org/10.1152/jappl.1974.37.2.247).
- [245] Sean C. Gifford, Michael G. Frank, et al. Parallel Microchannel-Based Measurements of Individual Erythrocyte Areas and Volumes. *Biophys. J.*, 84(1):623–633, January 2003. ISSN 0006-3495. doi: [10.1016/S0006-3495\(03\)74882-6](https://doi.org/10.1016/S0006-3495(03)74882-6).
- [246] Zhensong Xu, Yi Zheng, et al. Stiffness increase of red blood cells during storage. *Microsyst. Nanoeng.*, 4(1):17103, February 2018. ISSN 2055-7434. doi: [10.1038/micronano.2017.103](https://doi.org/10.1038/micronano.2017.103).
- [247] Igor V. Pivkin, Zhangli Peng, et al. Biomechanics of red blood cells in human spleen and consequences for physiology and disease. *Proc. Natl. Acad. Sci. U.S.A.*, 113(28):7804–7809, July 2016. ISSN 1091-6490. doi: [10.1073/pnas.1606751113](https://doi.org/10.1073/pnas.1606751113).
- [248] Rick Huisjes, Anna Bogdanova, et al. Squeezing for Life - Properties of Red Blood Cell Deformability. *Front. Physiol.*, 9:656., June 2018. ISSN 1664-042X. doi: [10.3389/fphys.2018.00656](https://doi.org/10.3389/fphys.2018.00656).

REFERENCES

- [249] W. Schwarz and H. Passow. Ca^{2+} -Activated K^{+} Channels in Erythrocytes and Excitable. *Annu. Rev. Physiol.*, (Volume 45, 1983):359–374, March 1983. doi: [10.1146/annurev.ph.45.030183.002043](https://doi.org/10.1146/annurev.ph.45.030183.002043).
- [250] Ryszard Grygorczyk. Temperature dependence of Ca^{2+} -activated K^{+} currents in the membrane of human erythrocytes. *Biochimica et Biophysica Acta (BBA) - Biomembranes*, 902(2):159–168, August 1987. ISSN 0005-2736. doi: [-10.1016/0005-2736\(87\)90291-4](https://doi.org/10.1016/0005-2736(87)90291-4)".
- [251] R. M. Johnson and S. A. Gannon. Erythrocyte cation permeability induced by mechanical stress: a model for sickle cell cation loss. *American Journal of Physiology-Cell Physiology*, November 1990. doi: [-10.1152/ajp-cell.1990.259.5.C746](https://doi.org/10.1152/ajp-cell.1990.259.5.C746)".
- [252] Robert M. Johnson and Ke Tang. Induction of a Ca^{2+} -activated K^{+} channel in human erythrocytes by mechanical stress. *Biochimica et Biophysica Acta (BBA) - Biomembranes*, 1107(2):314–318, June 1992. ISSN 0005-2736. doi: [-10.1016/0005-2736\(92\)90418-L](https://doi.org/10.1016/0005-2736(92)90418-L)".
- [253] W. Tillmann, C. Levin, G. Prindull, and W. Schröter. Rheological properties of young and aged human erythrocytes. *Klin. Wochenschr.*, 58(11):569–574, June 1980. ISSN 1432-1440. doi: [10.1007/BF01477168](https://doi.org/10.1007/BF01477168).
- [254] O. Linderkamp, E. Friederichs, T. Boehler, and A. Ludwig. Age dependency of red blood cell deformability and density: studies in transient erythroblastopenia of childhood. *Br. J. Haematol.*, 83(1):125–129, January 1993. ISSN 0007-1048. doi: [10.1111/j.1365-2141.1993.tb04642.x](https://doi.org/10.1111/j.1365-2141.1993.tb04642.x).
- [255] S. P. Suter, R. A. Gardner, C. W. Boylan, G. L. Carroll, K. C. Chang, J. S. Marvel, C. Kilo, B. Gonen, and J. R. Williamson. Age-related changes in deformability of human erythrocytes. *Blood*, 65(2):275–282, February 1985. ISSN 0006-4971. doi: [10.1182/blood.V65.2.275.275](https://doi.org/10.1182/blood.V65.2.275.275).
- [256] Elie Nader, Marc Romana, and Philippe Connes. The Red Blood Cell—Inflammation Vicious Circle in Sickle Cell Disease. *Front. Immunol.*, 11:517556, March 2020. ISSN 1664-3224. doi: [10.3389/fimmu.2020.00454](https://doi.org/10.3389/fimmu.2020.00454).
- [257] Florencia Orrico, Sandrine Laurance, Ana C. Lopez, Sophie D. Lefevre, Leonor Thomson, Matias N. Möller, and Mariano A. Ostuni. Oxidative Stress in Healthy and Pathological Red Blood Cells. *Biomolecules*, 13(8):1262, August 2023. ISSN 2218-273X. doi: [10.3390/biom13081262](https://doi.org/10.3390/biom13081262).
- [258] Matias N. Möller, Florencia Orrico, Sebastián F. Villar, Ana C. López, Nicolás Silva, Marcel Donzé, Leonor Thomson, and Ana Denicola. Oxidants and Antioxidants in the Redox Biochemistry of Human Red Blood Cells. *ACS Omega*, 8(1):147–168, January 2023. doi: [10.1021/acsomega.2c06768](https://doi.org/10.1021/acsomega.2c06768).
- [259] Richard A. Cooper. Influence of increased membrane cholesterol on membrane fluidity and cell function in human red blood cells. *J. Supramol. Struct.*, 8(4):413–430, January 1978. ISSN 0091-7419. doi: [10.1002/jss.400080404](https://doi.org/10.1002/jss.400080404).
- [260] J. S. Owen, K. R. Bruckdorfer, R. C. Day, and N. McIntyre. Decreased erythrocyte membrane fluidity and altered lipid composition in human liver disease. *J. Lipid Res.*, 23(1):124–132, January 1982. ISSN 0022-2275. doi: [10.1016/S0022-2275\(20\)38181-5](https://doi.org/10.1016/S0022-2275(20)38181-5).
- [261] Daniel Pan, Omayra Vargas-Morales, Blaine Zern, Aaron C. Anselmo, Vivek Gupta, Michael Zakrewsky, Samir Mitragotri, and Vladimir Muzykantov. The Effect of Polymeric Nanoparticles on Biocompatibility of Carrier Red Blood Cells. *PLoS One*, 11(3):e0152074, March 2016. ISSN 1932-6203. doi: [10.1371/journal.pone.0152074](https://doi.org/10.1371/journal.pone.0152074).
- [262] Daniel C. Pan, Jacob W. Myerson, Jacob S. Brenner, Priyal N. Patel, Aaron C. Anselmo, Samir Mitragotri, and Vladimir Muzykantov. Nanoparticle Properties Modulate Their Attachment and Effect on Carrier Red Blood Cells. *Sci. Rep.*, 8(1615):1–12, January 2018. ISSN 2045-2322. doi: [10.1038/s41598-018-19897-8](https://doi.org/10.1038/s41598-018-19897-8).
- [263] A. Iolascon, S. Perrotta, and Stewart G. W. Red blood cell membrane defects. *Rev. Clin. Exp. Hematol.*, 7(1):22–56, March 2003. ISSN 1127-0020. URL <https://europepmc.org/article/med/14692233>.
- [264] Achille Iolascon, Immacolata Andolfo, and Roberta Russo. Advances in understanding the pathogenesis of red cell membrane disorders. *Br. J. Haematol.*, 187(1):13–24, October 2019. ISSN 0007-1048. doi: [10.1111/bjh.16126](https://doi.org/10.1111/bjh.16126).
- [265] Jean Delaunay. The molecular basis of hereditary red cell membrane disorders. *Blood Rev.*, 21(1):1–20, January 2007. ISSN 0268-960X. doi: [10.1016/j.blre.2006.03.005](https://doi.org/10.1016/j.blre.2006.03.005).
- [266] F. Ch. Mokken, M. Kedaria, Ch. P. Henny, M. R. Hardeman, and A. W. Gelb. The clinical importance of erythrocyte deformability, a hemorrheological parameter. *Ann. Hematol.*, 64(3):113–122, March 1992. ISSN 1432-0584. doi: [10.1007/BF01697397](https://doi.org/10.1007/BF01697397).
- [267] G. D. O. Lowe. 1 Blood rheology in vitro and in vivo. *Baillières Clin. Haematol.*, 1(3):597–636, September 1987. ISSN 0950-3536. doi: [10.1016/S0950-3536\(87\)80018-5](https://doi.org/10.1016/S0950-3536(87)80018-5).

REFERENCES

- [268] Giuseppe Cicco and Sebastiano Cicco. *Hemorheological Aspects in The Microvasculature of Several Pathologies*, volume 599. Kluwer, January 2007. ISBN 978-0-387-71763-0. doi: [10.1007/978-0-387-71764-7_2](https://doi.org/10.1007/978-0-387-71764-7_2).
- [269] Maria Fornal, Małgorzata Lekka, Grażyna Pyka-Fościk, Kateryna Lebed, Tomasz Grodzicki, Barbara Wizner, and Jan Styczeń. Erythrocyte stiffness in diabetes mellitus studied with atomic force microscope. *Clin. Hemorheol. Microcirc.*, 35(1-2):273–276, January 2006. ISSN 1386-0291. URL <https://content.iospress.com/articles/clinical-hemorheology-and-microcirculation/ch938>.
- [270] Ida Dulińska, Marta Targosz, Wojciech Strojny, Małgorzata Lekka, Paweł Czuba, Walentyna Balwierz, and Marek Szymoński. Stiffness of normal and pathological erythrocytes studied by means of atomic force microscopy. *J. Biochem. Bioph. Methods*, 66(1):1–11, March 2006. ISSN 0165-022X. doi: [10.1016/j.jbbm.2005.11.003](https://doi.org/10.1016/j.jbbm.2005.11.003).
- [271] Diana Pinho, Tomoko Yaginuma, and Rui Lima. A microfluidic device for partial cell separation and deformability assessment. *Biochip J.*, 7(4):367–374, December 2013. ISSN 2092-7843. doi: [10.1007/s13206-013-7408-0](https://doi.org/10.1007/s13206-013-7408-0).
- [272] Emanuela Cecchin, Sergio De Marchi, Giacomo Panarello, and Vincenzo De Angelis. Rheological Abnormalities of Erythrocyte Deformability and Increased Glycosylation of Hemoglobin in the Nephrotic Syndrome. *Am. J. Nephrol.*, 7(1):18–21, January 1987. ISSN 0250-8095. doi: [10.1159/000167423](https://doi.org/10.1159/000167423).
- [273] Masakazu Kohno, Koh-ichi Murakawa, Kenichi Yasunari, Koji Yokokawa, Takeshi Horio, Hiroaki Kano, Mieko Minami, and Junichi Yoshikawa. Improvement of erythrocyte deformability by cholesterol-lowering therapy with pravastatin in hypercholesterolemic patients. *Metabolism*, 46(3):287–291, March 1997. ISSN 0026-0495. doi: [10.1016/S0026-0495\(97\)90255-9](https://doi.org/10.1016/S0026-0495(97)90255-9).
- [274] Brian D. Smith. Abnormal erythrocyte fragmentation and membrane deformability in paroxysmal nocturnal hemoglobinuria. *Am. J. Hematol.*, 20(4):337–343, December 1985. ISSN 0361-8609. doi: [10.1002/ajh.2830200404](https://doi.org/10.1002/ajh.2830200404).
- [275] S. Majid Hosseini and James J. Feng. How Malaria Parasites Reduce the Deformability of Infected Red Blood Cells. *Biophys. J.*, 103(1):1–10, July 2012. ISSN 0006-3495. doi: [10.1016/j.bpj.2012.05.026](https://doi.org/10.1016/j.bpj.2012.05.026).
- [276] Gilda A. Barabino, Manu O. Platt, and Dhananjay K. Kaul. Sick Cell Biomechanics. *Annu. Rev. Biomed. Eng.*, (Volume 12, 2010):345–367, August 2010. doi: [10.1146/annurev-bioeng-070909-105339](https://doi.org/10.1146/annurev-bioeng-070909-105339).
- [277] M. Brust, O. Aouane, et al. The plasma protein fibrinogen stabilizes clusters of red blood cells in microcapillary flows. *Sci. Rep.*, 4(4348):1–6, March 2014. ISSN 2045-2322. doi: [10.1038/srep04348](https://doi.org/10.1038/srep04348).
- [278] Saša Svetina, Drago Kuzman, et al. The cooperative role of membrane skeleton and bilayer in the mechanical behaviour of red blood cells. *Bioelectrochemistry*, 62(2):107–113, May 2004. ISSN 1567-5394. doi: [10.1016/j.bioelechem.2003.08.002](https://doi.org/10.1016/j.bioelechem.2003.08.002).
- [279] Oguz K. Baskurt and Herbert J. Meiselman. Red blood cell mechanical stability test. *Clin. Hemorheol. Microcirc.*, 55(1):55–62, January 2013. ISSN 1386-0291. doi: [10.3233/CH-131689](https://doi.org/10.3233/CH-131689).
- [280] S. Braunmüller, L. Schmid, et al. Dynamics of red blood cells and vesicles in microchannels of oscillating width. *J. Phys.: Condens. Matter*, 23(18):184116, April 2011. ISSN 0953-8984. doi: [10.1088/0953-8984/23/18/184116](https://doi.org/10.1088/0953-8984/23/18/184116).
- [281] Xuejin Li, Zhangli Peng, et al. Probing red blood cell mechanics, rheology and dynamics with a two-component multi-scale model. *Philosophical transactions. Series A, Mathematical, physical, and engineering sciences*, 372(2021), August 2014. doi: [10.1098/rsta.2013.0389](https://doi.org/10.1098/rsta.2013.0389).
- [282] Quan Guo, Simon P. Duffy, et al. Microfluidic analysis of red blood cell deformability. *J. Biomech.*, 47(8):1767–1776, June 2014. ISSN 0021-9290. doi: [10.1016/j.jbiomech.2014.03.038](https://doi.org/10.1016/j.jbiomech.2014.03.038).
- [283] Gerhard Gompper and Dmitry A. Fedosov. Modeling microcirculatory blood flow: current state and future perspectives. *WIREs Syst. Biol. Med.*, 8(2):157–168, March 2016. ISSN 1939-5094. doi: [10.1002/wsbm.1326](https://doi.org/10.1002/wsbm.1326).
- [284] Pascal Preira, Thomas Leoni, et al. Microfluidic tools to investigate pathologies in the blood microcirculation. *Int. J. Nanotechnol.*, February 2012. URL <https://www.inderscienceonline.com/doi/abs/10.1504/IJNT.2012.045340>.
- [285] Zhu Chen, Changhu Xiao, et al. Recent Advances of Artificial Intelligence in Cardiovascular Disease. *J. Biomed. Nanotechnol.*, 16(7):1065–1081, July 2020. ISSN 1550-7033. doi: [10.1166/jbn.2020.2955](https://doi.org/10.1166/jbn.2020.2955).
- [286] Robert Kotan, Katalin Peto, et al. Hemorheological and Microcirculatory Relations of Acute Pancreatitis. *Metabolites*, 13(1):4, December 2022. ISSN 2218-1989. doi: [10.3390/metabo13010004](https://doi.org/10.3390/metabo13010004).
- [287] Jose M. Ayuso, María Virumbrales-Muñoz, et al. A role for microfluidic systems in precision medicine. *Nat. Commun.*, 13(3086):1–12, June 2022. ISSN 2041-1723. doi: [10.1038/s41467-022-30384-7](https://doi.org/10.1038/s41467-022-30384-7).

